Micromechanics of oxide inclusions in ferrous alloys

Alejandra Inés SLAGTER

Acknowledgments

I want to express my most sincere appreciation to Andreas Mortensen for his guidance, support, and advice he provided during these years. His kindness and consideration made these years particularly gratifying.

I would also like to thank the members of the thesis examination committee: Dr. Aïcha Hessler-Wyser, Prof. Jérôme Chevalier, Prof. Guillaume Kermouche, and Prof. Roland Logé for the time they dedicated to this thesis and the interesting discussions.

This work would not have been possible without the financial support of the Swiss National Science Foundation (Grant No. 20 0 021_182557), for which I am grateful.

In addition, I would like to acknowledge everyone that contributed to this project and extended aid during these years. In particular, I would like to express my gratitude to:

Joris Everaerts and David Hernández Escobar, who, at different times, were also part of the "inclusions" team and with whom we shared numerous experiments and discussions.

Léa Deillon, for the aid provided at the beginning of this work and for help in taking my first steps at EPFL.

The LMM team, in particular to Raphaël Charvet and Cyril Dénéréaz for all the help provided for the experimental work and for the design and installation of the cold-crucible apparatus.

The personnel of the Center for Electron Microscopy, particularly Grégoire Baroz and Lucie Navratilova, for the support in the use of the scanning electron microscope and focused ion beam.

Finally, to Luciano, who has always been a source of support and encouragement both in and outside the lab.

Abstract

Oxide inclusions are inevitably present in steel as a direct consequence of the steelmaking process; as a result, a cubic centimetre of modern steel will generally contain about a million of these hard and brittle micrometre-sized ceramic particles. Inclusions are important because they influence, generally in a negative way, the alloy mechanical performance. Current knowledge concerning compositions, formation and growth mechanisms of inclusions in steel is well-established; however, inclusion intrinsic mechanical properties are less well understood.

A number of techniques have been developed in the past years that allow the measurement of local properties on individual phases or small-scale materials. Methods have been proposed to assess the strength of micrometre-sized particles, which can be adapted to obtain the properties of oxide inclusions. Other methods, such as nanoindentation, can be used to probe the stiffness and hardness of a vast range of materials; however, special considerations are needed if those are to be used for micrometre-sized particles embedded in a dissimilar matrix.

In this work, oxide inclusions in iron alloys are produced by melting and deoxidizing high-purity iron under a controlled atmosphere. Inclusion characteristics, including chemical composition and observed morphologies, are studied using standard characterization techniques such as scanning electron microscopy and energy dispersive spectroscopy. The mechanical properties of selected inclusions are studied using micromechanical testing methods. The stiffness and hardness are probed by nanoindentation and analysed using a strategy that is developed in this work to obtain matrix-independent data when testing embedded particles. The correction is based on theoretical considerations complemented with results from finite element simulations and leads to an accurate determination if indentation data are collected and averaged from a large number of particles (~30 or more). Finally, the strength of oxide particles is measured by producing and testing micromechanical test samples out of individual inclusions.

Results of this work show that the local inclusion stiffness and hardness vary strongly within narrow compositional ranges in inclusions based on Si-Fe-Mn oxide, or alternatively remain relatively unchanged as a function of the oxide chemistry in inclusions based on Si-Al-Ca oxide. Stiffnesses remain lower than that of iron for all inclusions except Mn-rich Si-Fe-Mn oxides, in turn suggesting that such inclusions might be more benign with respect to high-cycle fatigue resistance. Hardness values for inclusions analysed in this work, remaining in the range of 4 to 11 GPa, are all relatively high when compared to typical values for metal alloys, while also showing an upward jump in Mn-rich Si-Fe-Mn-O inclusions. In-situ micromechanical tests performed on individual inclusions made of amorphous SiO_2 show that the strain and stress to failure of these individual particles can reach values in the range of 8 to 17 % and in the order of 10 GPa. These fall within the range of the highest values so far reported for dry silica and demonstrate that oxide inclusions within iron can, in fact, be very strong.

Keywords: inclusions, oxide, steel, silica, nanoindentation, hardness, stiffness.

Résumé

La présence d'inclusions d'oxyde dans la microstructure des aciers est une conséquence inévitable du processus de fabrication de cet alliage : chaque centimètre cube d'acier contient typiquement environ un million de ces particules en céramique micrométrique. La présence de ces inclusions d'oxyde dures et fragiles péjore généralement la performance mécanique des aciers. Les connaissances actuelles concernant les compositions, la formation et les mécanismes de croissance des inclusions dans l'acier sont relativement bien établies ; cependant, les propriétés mécaniques intrinsèques de ces inclusions sont moins bien connues.

Plusieurs techniques ont été développées au cours de ces dernières années permettant de mesurer les propriétés locales de phases individuelles ou d'échantillons de matériau de faible dimension. Il est notamment aujourd'hui possible de mesurer la résistance mécanique de particules de taille micrométrique par des méthodes qui peuvent être adaptées pour obtenir les propriétés d'inclusions d'oxyde. La nanoindentation peut être utilisée pour mesurer la rigidité et la dureté d'une vaste gamme de matériaux ; cependant, des considérations particulières sont nécessaires si cette technique est utilisée pour caractériser des particules de petit taille noyées dans une matrice ayant une autre rigidité.

Dans le cadre de ce travail, des inclusions d'oxyde dans du fer sont produites par fusion et désoxydation de fer de haute pureté de l'oxygène sous atmosphère contrôlée. Les caractéristiques des inclusions, notamment leur composition chimique et leur morphologie, sont étudiées à l'aide de techniques de caractérisation microstructurale telles que la microscopie électronique à balayage et la spectroscopie à dispersion d'énergie. Les propriétés mécaniques d'inclusions sélectionnées sont étudiées à l'aide de méthodes d'essais micromécaniques. La rigidité et la dureté sont sondées par nanoindentation de particules incorporées au sein d'une matrice de fer, à l'aide d'une stratégie développée au cours de ce travail pour rendre la mesure du module élastique et de la dureté des inclusions indépendante de la matrice, laquelle influence le signal par sa rigidité différente de celle de la particule. La correction est basée sur des considérations théoriques complétées par des simulations par éléments finis. Il est démontré qu'à condition que les données d'indentation soient collectées et moyennées à partir d'un nombre suffisant de particules (~30 ou plus), cette technique conduit à une détermination relativement précise de la dureté et la rigidité des particules. La résistance mécanique de particules d'oxyde individuelles est ensuite mesurée en sollicitant des échantillons d'essai micromécanique formés à partir d'inclusions individuelles.

Les résultats de ce travail montrent que la rigidité et la dureté locales d'inclusions d'oxyde formées par précipitation dans le fer varient fortement en fonction de la teneur en manganèse dans les inclusions à base d'oxyde de Si-Fe-Mn, ou alternativement restent relativement inchangées en fonction de la chimie de l'oxyde dans les inclusions à base d'oxyde de Si-Al-Ca. Les rigidités restent inférieures à celles du fer pour toutes les inclusions, à l'exception des oxydes Si-Fe-Mn riches en Mn, ce qui suggère que ces inclusions pourraient être moins nocives en ce qui concerne la résistance à la fatigue à cycle élevé. Les valeurs de dureté des inclusions analysées dans ce travail, qui se situent entre 4 et 11 GPa, sont toutes relativement élevées par rapport aux valeurs typiques des alliages métalliques, tout en montrant comme le module un saut vers le haut pour les inclusions Si-Fe-Mn-O riches en Mn. Des essais micromécaniques

in-situ réalisés sur des inclusions individuelles en SiO_2 amorphe montrent que la déformation et la contrainte à la rupture de ces particules peuvent atteindre des valeurs de 8 à 17 % pour la déformation et de l'ordre de 10 GPa pour la résistance mécanique. Ces valeurs se situent dans la fourchette des valeurs les plus élevées rapportées à ce jour pour la silice sous atmosphère sèche et démontrent que les inclusions d'oxyde dans le fer peuvent, en fait, être des phases de haute performance mécanique.

Table of contents

Chapter 1 – Introduction

In metal alloys, the term inclusion refers to micrometre-sized non-metallic second phases found in the microstructure, generally as an undesirable byproduct of the alloy fabrication process. In steels, typical inclusions are sulphides or oxide compounds. Although their amount and size have considerably decreased with the evolution of steel processing technology, their presence in steel alloys cannot be entirely avoided.

These second phases are known to affect alloy properties, generally degrading the mechanical performance of steel products. Examples of the detrimental effect of non-metallic inclusions include the degradation of fatigue properties, a decreased machinability, and lower strains to failure when the amount and/or the size of inclusions is increased. In addition, inclusions can influence alloy processability, for example, by clogging duct nozzles during casting operations, by causing the formation of defects during rolling, or by leading to wire fracture during steel wire drawing.

Some inclusion characteristics that render them particularly harmful are well known, namely a large size or a high volume fraction; however, the role of other inclusion properties is less well understood. Part of the reason why clear relationships between inclusion properties and steel performance have not yet been determined is linked to the wide variety of possible inclusion compositions and structures. Only considering oxide particles, the composition of inclusions can, in many cases, produce a mixed oxide containing several oxides such as Al_2O_3, SiO_2, CaO, MgO, MnO, and FeO, or a mixture of oxide and sulphide phases. A further complication is the fact that industrial casts usually contain, in one single alloy, many inclusions of different compositions, shapes, and sizes.

Inclusion properties that are deemed important but whose role is not fully understood include their hardness, stiffness, and coefficient of thermal expansion, in addition to the particle strength and that of its interface with steel, all of which are expected to vary upon the inclusion composition and structure, and likely also on the steel processing history. Some of these properties are available in the literature over a relatively wide range of inclusion compositions: the deformability and thermal expansion coefficient have received considerable attention, while hardness values have been reported for several inclusion phases. Other important properties, such as the inclusion stiffness, have mostly been reported for bulk materials and are generally limited to stoichiometric inclusion compositions. In addition, the strength of oxide particles is expected to depend on the volume of stressed material through the distribution of defects in its midst. As a consequence, the strength of micrometre-sized oxide particles is likely to differ from that extrapolated from bulk ceramic materials produced by other means.

This thesis explores the use of nanomechanical testing methods to measure local mechanical properties of oxide inclusions in iron. It was carried out in the framework of a project funded by the Swiss National Science Foundation (Grant No. 20 0 021_182557), which has as its primary objective the quantification of mechanical properties of micrometre-sized oxide inclusions produced by precipitation within iron melts. This project aims to fill a gap in the science of steel by linking the local structure of oxide inclusions with their properties, by

relating those with the conditions that lead to their appearance in steel products, and potentially also relating those with the influence exerted by inclusions on the properties of steel. Particular interest is placed on determining inclusion mechanical properties, including their stiffness, hardness, the strength of the oxide-metal interface and that of the oxide inclusions themselves.

Fulfilling this goal is nowadays made possible by progress in micromechanical testing methods. In particular, this project builds on expertise acquired by the laboratory within the framework of a previous five-year grant (ERC Advanced Grant project 291085), which led to the development of a testing method that can measure the strength of small second phases in a metallic matrix. The measurement of two other inclusion properties, namely their stiffness and hardness, is made possible by nanoindentation techniques. Those cannot be directly applied to inclusions because indented particles are embedded in an iron matrix, which influences their nanoindentation response; therefore, part of this work is focused on developing a strategy to account for this influence. In parallel with this work, techniques dedicated to extracting matrix-particle interfacial properties are currently under development (not presented here); this work is chiefly carried out by Dr. David Hernández Escobar, who has been working on the project since September 2021. Other contributions to the project include the two-year work by Dr. Joris Everaerts (September 2019 to August 2021), together with preliminary work by Dr. Léa Deillon and Dr. Marta Fornabaio, whose contributions are reflected in some of the work presented here.

After a brief survey of the literature related to this work (Chapter 2), the thesis is structured in three parts. The first part addresses substrate effects observed when stiffness and hardness properties are to be deduced from nanoindentation data obtained by probing embedded particles. The details of the problem and a strategy developed to extract indentation properties that are independent of the matrix contributions are presented in Chapter 3. The second part is concerned with the production of oxide inclusions of controlled compositions by precipitation within iron melts. The fabrication process and the characteristics of obtained inclusions are presented in Chapter 4, along with the results of indentation properties obtained by probing inclusions in selected samples. The last chapter (Chapter 5) presents the details of strength determinations made on silicon oxide inclusions precipitated within iron melts. The in-situ experiments and finite element simulations show that micrometre-sized SiO_2 inclusions precipitated within iron can reach strain and stress levels on par with the highest values reported for dry silica.

Chapter 2 – Literature review

2.1 Non-metallic inclusions in steel

2.1.1 Inclusion sources

Current steel production methods inevitably lead to the precipitation, in the liquid metal, of small particles of oxide or sulphide, which remain trapped in the alloy and form part of the final solid steel microstructure. These non-metallic inclusions (NMI) usually have dimensions on the order of one to a few hundred micrometres and are known to affect the alloy's mechanical properties, most often in a negative way.

Exception made for intentionally re-sulphurized grades, the origin of sulphide inclusions in steel is generally to be traced in the raw materials since sulphur is mainly present as an impurity that comes with coke and other fuels. Sulphide is predominantly found in combination with Mn forming MnS inclusions, but CaS or (Mn,Ca)S inclusions can also be found if the steel is treated with Ca, as can sulphides containing Ce and other rare earth metals if those are incorporated in the alloy [1].

Oxide inclusions have two distinct origins. On the one hand, *exogenous* oxide inclusions are the consequence of the entrainment, by flowing steel, of fragments of the refractory oxides that are used to contain or protect the liquid metal [2,3]. This is because, for industrial melts, liquid metal handling is usually performed in containers made of or covered with refractory oxides. In addition, most steel fabrication processes are carried out under the protection of a layer of liquid oxide (the slag) which acts as a barrier, simultaneously minimising oxidation of the liquid metal and optimising its composition by equilibration of the metal and slag compositions. An immediate consequence is that, in handling the melt, great care must be exerted to avoid mixing the two liquids or forming areas where the metal comes in direct contact with air. The control of exogenous inclusions is of paramount importance since those tend to be large oxide particles or aggregates, generally being the most harmful to the steel properties.

Endogenous oxide inclusions are formed during ladle treatment as a consequence of the addition to the melt of elements, such as Al, Si, Mn, and Ca, that form oxides more stable than those of iron (and carbon). The formation of oxide inclusions during this step is intentionally triggered and serves to decrease the amount of oxygen dissolved in the iron, which is brought from a typical value of a few hundred ppm to a level on the order of only a few ppm [4]. Steel deoxidation was initially intended to avoid gas evolution during metal solidification, caused by the abrupt decrease of oxygen solubility when the metal transitions from the liquid to the solid state. Without the deoxidation step, the solidification of steels would be accompanied by the formation of carbon oxide gas, a phenomenon usually referred to as *effervescence*. Nowadays, the aim of the deoxidation step goes beyond avoiding effervescence and serves to satisfy user requirements for low-oxygen steels [5].

Over the past decades, improvements in steel cleanliness have been mainly driven by user demands for lower inclusion content. Large exogenous inclusions have been nearly eliminated by the implementation of clean liquid metal handling practices, with cornerstones being the implementation of shrouding in continuous casting and the use of uphill teeming in ingot casting [6–10]. Alternative steel processing routes, such as electroslag remelting, are also employed to modify or control the inclusion content [11]. Despite the advances in clean steel technology, processes used to decrease the inclusion content still represent an additional costs to alloy production. Consequently, requirements in inclusion control are primarily dependent on the intended use of the alloy since not only the amount but also the type and characteristics of the oxide inclusions tolerated in different steels are strongly linked to the final application [12].

2.1.2 Inclusion nucleation, growth, and removal

Deoxidation reactions are rapid: inclusion nucleation starts within seconds after the addition of deoxidiser elements. However, the time required to complete the deoxidation process in the ladle is usually affected by the time needed to dissolve the metallic additions and that required to homogenise the melt, which is a function of the ladle size [11,13].

Inclusions nucleated directly after the addition of deoxidisers are usually referred to as *primary inclusions.* Their chemical composition and that of the melt is determined by the equilibrium of reactions of the type:

$$x[M] + y[O] \leftrightarrow M_xO_y \qquad K_e = \frac{a_{M_xO_y}}{(a_M)^x (a_O)^y}$$
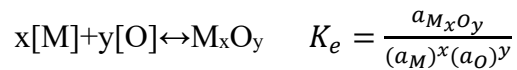
where elements dissolved in the melt are between brackets, K_e is the equilibrium constant of the reaction, and a is the activity of each component. Residual amounts of oxygen that remain in the melt after the formation of primary inclusions would then tend to segregate to the liquid during the solidification process, increasing the amount of dissolved oxygen in the unsolidified metal and triggering the formation of new oxide inclusions, usually referred to as *secondary inclusions* [14]. The extent to which secondary inclusions are formed depends on the remaining dissolved oxygen content in the alloy and on the melt composition evolution during solidification. As a result, secondary inclusions are prone to precipitate when weak deoxidisers such as Si and Mn are used and are less frequent when strong deoxidisers such as Al are employed (since such elements capture most of the oxygen while the alloy is fully liquid).

The choice of deoxidiser elements is generally defined by the steel composition and final use of the alloy. For example, steels deoxidised with Si-Mn are generally used for applications where machinability and excellent drawability are paramount [15–19]. In contrast, the use of Al-deoxidation yields alloys of very low oxygen content [1] but produces alumina inclusions with elevated hardness and stiffness. In addition, residual amounts of Al can have a strong effect on grain refinement due to the formation of aluminium nitrides such that Al-killed steels are known to have fine-grain structures [20]. Other elements, such as Ca, Ce, or Te, can be added during deoxidation to provide other oxide inclusions with specific characteristics [21–

25]. The most salient example is the use of Ca-treatment to form liquid calcium aluminates instead of solid alumina particles, mainly in order to avoid the clogging by alumina clustering of the nozzles that are used to duct the alloy before it is cast [21–24].
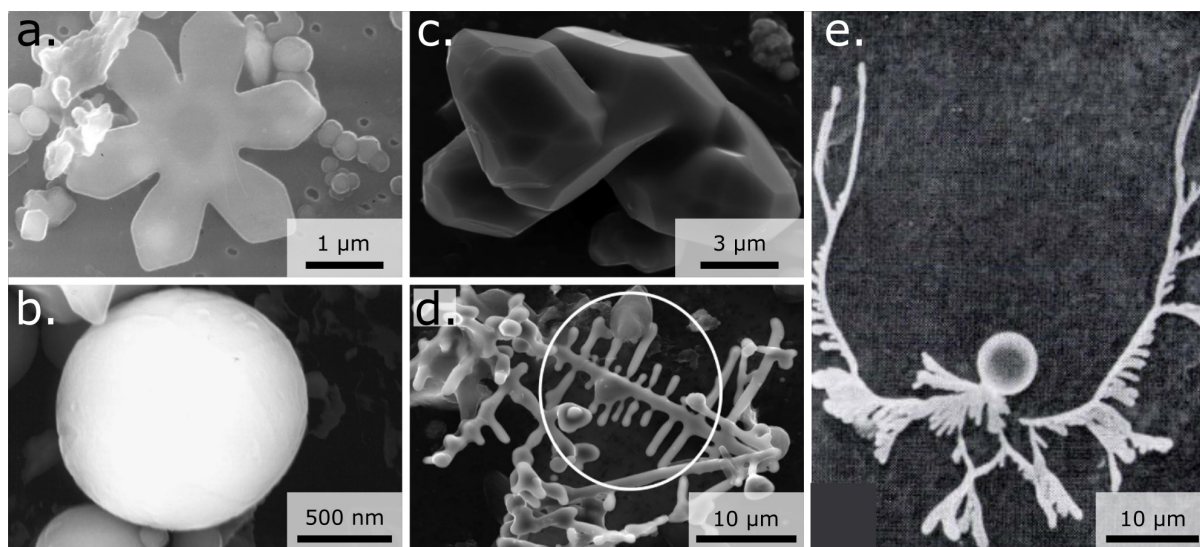

Figure 2.1 Examples of morphologies observed in oxide inclusions. a) to d) adapted from [26]; e) adapted from [27].

The composition of oxide inclusions is determined by the choice of deoxidising agents but can also be affected by the chemistry of refractories and slag(s) used in processing the steel [5,28–30]. The time scales over which equilibration reactions take place, however, can vary significantly. Inclusion changes due to steel-slag equilibration have been observed to take place within hundreds of seconds (or in other words minutes) [5,31], whereas inclusion precipitation reactions are completed within seconds [13]. In addition, the kinetics of steel-slag equilibration reactions are affected by the amount of stirring and emulsification of the slag, which affects the area over which steel and slag are in contact [5]. An vast amount of work has been dedicated to the development of computational thermodynamic tools which can serve to predict the efficiency of deoxidation and desulfurization reactions as well as the chemical composition of inclusions and steel after these processes [32–39]. Because complete equilibrium is rarely attained, accurate prediction of inclusion compositions is only possible if kinetics are also accounted for [13,24,30,31,40,41]. These can cause significant deviations from thermodynamic equilibrium, with the important consequence that oxide inclusions within a single steel casting usually do not have the same composition (which would be the same as that of the used slag if complete equilibration was attained). As a result, with the exception of oxides consisting of highly stable phases such as alumina, inclusions are usually found to have, within the same metal casting, a realtively wide range of compositions (see, *e.g.* [16,24]).

Regarding the shape of oxide inclusions, a wide variety of morphologies have been reported in as-cast products, illustrative examples are presented in Fig. 2.1. Inclusion shapes are, as expected, affected by the oxide composition and possible collisions with other particles, and hence on fluid flow within the metal. Liquid inclusions naturally tend to take a spherical shape, but inclusions that are solid at steelmaking temperatures have been reported to have spherical, faceted, plate-like or dendritic structures [14,26,42–44]. These morphologies seem to be

affected by the supersaturation degree [43,45], the presence of other oxide pre-existing oxide phases [44] or impurities [46]. In the case of silicon oxide inclusions, dendritic structures have also been linked to the formation of secondary inclusions [27,47].

Nucleated inclusions continue to evolve during steel processing. They can grow, aggregate, or react with other inclusions [48–51]. In the absence of stirring, growth by an Ostwald ripening mechanism has been corroborated [52]. Nevertheless, motionless alloys are rarely found in industrial melts, and even differences in density between the oxides and the steel melt are usually sufficient to induce particle motion. As a result, particles float and migrate, which promotes particle-to-particle collisions within the melt, resulting in aggregation. The speed at which particles travel upwards is determined by Stokes' law, with the particle uprise speed being proportional to the square of its diameter. Flotation times are thus intentionally allowed in steelmaking to decrease the number of large endogenous inclusions, and the process is typically enhanced by argon bubbling or vacuum treatment.

2.1.3 Effects of inclusions on steel properties and processing

Non-metallic inclusions are known to affect many steel properties, including strength, toughness, fatigue behaviour, machinability, surface finish, and welding properties [53–57]. In addition, inclusions can influence different aspects related to the processing of the steel, such as its ability to be formed, drawn, machined, or even cast.

Ductile fracture is directly affected by the presence of NMI, not only in the context of tensile testing but also during forming operations. The mechanism for ductile fracture comprises the nucleation of voids, usually observed at the interface with foreign particles or within the particles themselves, followed by void growth and coalescence [58]. Consequently, the strain to which metals can be deformed before the onset of damage is linked to the volume fraction of foreign particles and is affected by their ability to deform, their intrinsic strength, and that of the matrix-particle interface. Higher inclusion volume fractions, weaker inclusions or interfaces, and stiffer or harder particles are generally associated with lower strains to failure in the alloy [53,54].

Sulphides, particularly if elongated by forming operations, are usually related to low-impact toughness, reduced strength (particularly in the trough-thickness direction if the inclusions are elongated), and high anisotropy in mechanical properties [55,59]. Because sulphide inclusions and their interface with the matrix are weak, voids tend to nucleate at the inclusions by particle fracture when the steel is strained in the rolling direction. An even more detrimental effect is observed if the metal is strained in the trough-thickness direction, where voids are nucleated at relatively low strains due to the low inclusion-matrix interface strength [59,60]. Sulphides have been observed to be detrimental in fatigue experiments performed in torsion. In contrast, in axial fatigue experiments, the effect depends on the hot working ratio, the orientation of the sample with respect to the working direction, and the relative size of other types of inclusions [55,61]. Numerous reports highlight the non-damaging effect of sulphide inclusions in relation to contact fatigue experiments, in which such inclusions are even reported to be beneficial if

present as a layer enveloping other, oxide, inclusions [62]. Finally, the presence of soft sulphides is deliberately increased in free-machining steel grades. Those are re-sulphurized in the presence of sulphide-forming elements such as Mn to reach S contents in the range of 0.08 to 0.13 % (or even up to 0.35 %), as opposed to the maximum allowed content of 0.05 % in ordinary carbon steels. The reason behind re-sulfurization is that these soft inclusions induce, during machining of the metal, the formation of broken chips instead of a long unbroken continuous stringer and provide a lubrication action that prevents tool wear, decreasing machining costs [6].

Inclusions have also been found to have a positive impact on steel properties by acting as nucleation sites for acicular ferrite, particularly in welded structures. Acicular ferrite is important to achieve a good balance between strength and toughness in components that cannot be further strengthened by deformation. Ref. [63] reviews some of the mechanisms that have been proposed to explain why inclusions act as ferrite nucleation sites. In addition, aluminium-killed steels are usually associated with fine-grained heat-treated microstructures. The reason for this is not the presence of alumina inclusions *per se* but rather the fact that excess aluminium combines with nitrogen to produce AlN precipitates at low austenitising temperatures, with AlN having a strong effect limiting austenite grain growth [20].

Oxide inclusions are often associated with detrimental effects also in the processing of steel. In this respect, a common issue during the casting of commercial steel grades is the clogging of the nozzles that feed the mould, which disrupts production, decreases productivity, and can lead to a quality loss in the final product [29,36,64,65]. Clogging is observed mainly in Al-killed steels and is caused by the agglomeration of alumina or $MgO \cdot Al_2O_3$ spinel inclusions, which adhere to each other and to the refractory walls of the nozzles. The high agglomeration tendency of alumina inclusions has been related to the poor wetting of solid alumina by liquid iron [48,66,49], a consequence of the high interfacial energy between the iron melt and the alumina. This causes the formation of a cavity between two alumina particles to be energetically favoured if those are sufficiently close to each other [49]. The resulting liquid/void meniscus creates an attractive force between the particles, pulling them together much as slight amounts of water pulls hair together into strands. In turn, this leads, at molten steel temperatures, to the mutual sintering of the particles once they are in contact along a portion of their surface [49,67]. The interfacial energy and hence the degree of wetting and ensuing sintering has been observed to depend on the liquid iron composition, particularly in relation to the O and S contents [51]. The effect is usually mitigated by adding Ca to the steel, as this tends to transform solid alumina inclusions into liquid calcium aluminates, which remain spherical as they coalesce [4,21–24,68].

As already mentioned, inclusions can cause defects during forming operations by promoting void nucleation and reducing steel ductility [9,69]. Another frequent problem associated with non-metallic inclusions is the fact that they cause the presence of surface imperfections on cold-rolled products. These imperfections, which are not tolerable in steels used for exposed applications, are caused by the presence, near the surface, of large oxide inclusions (< 20 μm), which do not deform at the same rate as the metallic matrix and leave line defects, usually called slivers, Fig. 2.2 a [64,70].

Other than the previously mentioned issues, which are common to many commercial steel grades, oxides inclusions have been largely studied in the context of specific steel groups to solve issues related to the production and use of those specific steel families [56].

For tire cord steels, the importance of inclusions stems from the fact that the steel must be drawn to very small diameters. If hard, brittle inclusions are present in the metal, those can cause the wire to fracture as it is being produced (Fig. 2.2 b) and generate substantial productivity losses. For this reason, steels drawn to very small diameters are generally deoxidised with Si with the goal of obtaining inclusions that are deformable at drawing temperatures since it is generally recognised that Al-rich inclusions, which tend to be hard, brittle and highly refractory, lead to a higher frequency of wire fracture [17,16,71,15]. It has been observed that the deformability of inclusions generally correlates with the melting temperature of the oxide [72,69] and, as a consequence, a vast amount of the research related to inclusion engineering in the context of tire cord steel production focuses on identifying, with extensive use of thermodynamic prediction packages, oxide compositions that are both technologically feasible and likely to yield low melting point inclusions [17,16,71,15].
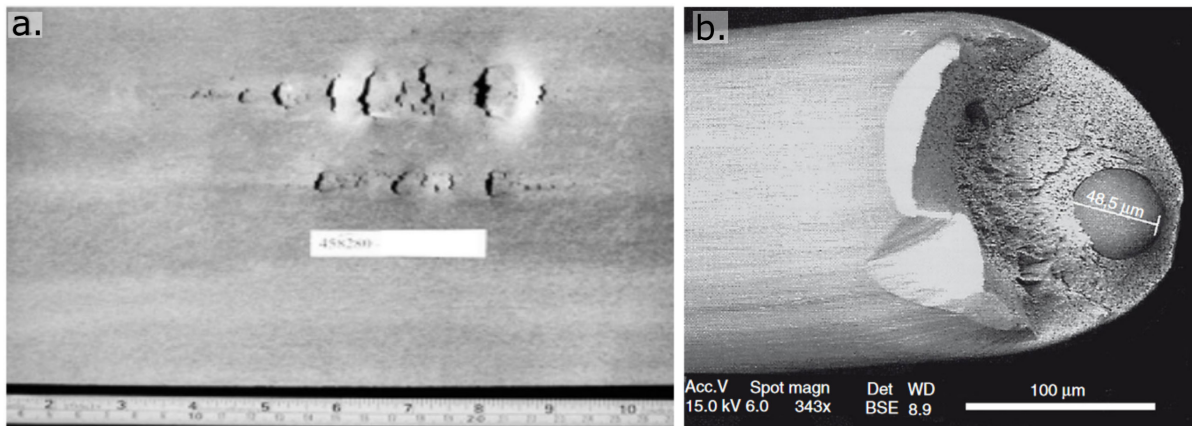

Figure 2.2 Examples of damage caused by non-metallic inclusions during steel processing. a) surface defects in rolled products, reproduced from [57] with permission of Elsevier Science & Technology Journals; b) wire fracture caused by an inclusion during drawing **[73]** (Reprinted with permission of ASM International. All rights reserved. www.asminternation.org).

For bearing steels, the requirements in inclusion control are chiefly determined by the desired fatigue properties of the steel. The topic is complex: the fabrication process has been shown to have a major effect on the fatigue performance of steel bearings [62,74], but at the same time, due to the wide variety of oxide compositions that can be observed in relation to different steel processing routes, our understanding of the key inclusion characteristics that affect the fatigue performance is, still nowadays, somewhat unclear. The fact that the steel processing history, through the type and amount of NMI, has a determining effect on the fatigue life of bearings was clear from early times to the extent that Swedish bearing steel production did not shift to modern, more efficient, electric arc melting until the inclusion population in the latter process was sufficiently controlled in such way that bearing lives could be maintained [75]. Over the years, it became clear that a lower inclusion content usually leads to longer fatigue lives, and it was recognised that larger inclusions are usually responsible for early fatigue failures. Clear correlations have, however, been hard to establish, in part due to challenges in the characterisation of the inclusion content [10,76,77]. The subject is further complicated if the

very high cycle fatigue regime is considered because, in this regime, inclusions are always associated with crack initiation sites, while hydrogen trapped at the inclusions has been observed to play an important role in the process of voiding [78–80].

The most straightforward way of obtaining information about harmful inclusions is to analyse the characteristics of inclusions at fatigue damage and fracture origin sites. This can provide detailed information about the size, location, and chemical composition of each inclusion actually responsible for crack or void nucleation; however, such observations are only possible after a metal piece or sample has failed. An extended approach to predict the fatigue performance is to determine the steel *total* oxygen content, which generally correlates well with the fatigue life. The technique has the advantage of being repeatable and easily implemented at the steel shop level; however, it does not provide information about the inclusion population characteristics, such as the distributions of type, size, or morphology, which likely also play an important role. For example, it has been observed that, for the same (total) oxygen content, electroslag remelted steels can present longer fatigue lives than bearing steels fabricated by more conventional processing routes [81]. The reason has been attributed to differences in the size distribution of the inclusions, which illustrates the difficulties in the identification of a single, controlling parameter that can be viewed as chiefly responsible for the influence exerted by inclusions on the fatigue of bearing steels.

When discussing the effect of NMI on fatigue properties, it is important to highlight that those are only detrimental for steel components of high microstructural hardness (typically higher than 400 H_V), for which the fatigue limit is seen to deviate (to lower strengths) from the linear relationship observed between hardness (and hence yield strength) and fatigue strength, Fig. 2.3 [78]. This is related to the fact that, for low metal hardness (or in the high-stress, low-cycle fatigue regime), fatigue cracks originate at slip bands, while for high metal hardness (or in the low-stress, high-cycle fatigue regime), cracks tend to originate from inclusions [55].

In their influence on steel mechanical properties, the following inclusion characteristics are usually deemed important:

    i)   inclusion shape and/or aspect ratio,
    ii)   matrix-inclusion adherence,
    iii)   matrix-inclusion elastic mismatch,
    iv)   matrix-inclusion mismatch in thermal expansion coefficient,
    v)   inclusion size.

Contradictory arguments are found when trying to elucidate which among these inclusion attributes are the most significant for fatigue performance. A good illustration of the lack of agreement in this respect can be found in the different explanations that various authors give to the fact that calcium aluminate inclusions are usually pointed out as the most harmful inclusion type for fatigue properties, followed by alumina and spinel inclusions, while manganese sulphides are reported to be the least detrimental, or even beneficial [82–85,55].
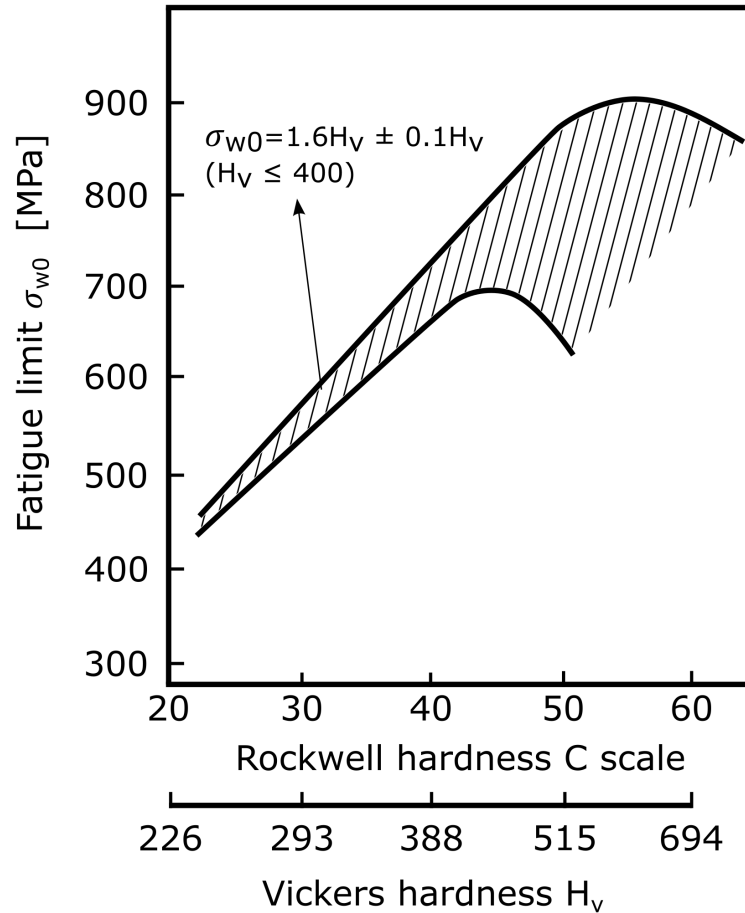
Figure 2.3 Relationship between fatigue limit and hardness for iron alloys. Redrawn from **[86]**.

On the one hand, Kiessling considered the plasticity of non-metallic inclusions as the most relevant parameter and related the non-damaging effect of MnS inclusions to their deformability since MnS are observed to be among the most deformable inclusions while Ca-aluminates are among the least deformable types [69,84] (though alumina and spinel inclusions are also not seen to deform along with steel, see Fig. 2.5).

On the other hand, Brooksbank and Andrew [82] attributed the harmful effect of calcium-aluminate inclusions (and the non-damaging effect of MnS) to the presence of residual stresses that are generated due to significant differences between the thermal expansion coefficients (CTE) of inclusions and steel. They measured the CTE of different types of inclusions [87,88], determined the stress distribution that would result after metal cooldown and concluded, based on a good correlation between CTE and "damaging effect", that differences in the thermal expansion coefficient seem to explain differences in fatigue behaviour. Other authors point out that this hypothesis is incorrect because stresses of tensile character are always produced around inclusions, with the location being dependent on the sign of the CTE mismatch, but with inclusion always being sites of stress concentration [78]. It is thus suggested that such stress concentration would inevitably lead to crack nucleation at inclusions, regardless of the type of inclusion and regardless of its CTE, leading to inclusion fracture or debonding from the matrix.

Moreover, other authors ascribed the differences in the damaging effect of different types of inclusions to the role and characteristics of interfacial bonding or considered debonding as a critical step in the initiation of fatigue cracks [62,83]. For example, Tricot et al. [62] observed that sulphides, and even large carbides, do not act as sites for the initiation of "butterflies" (a predecessor of rolling contact fatigue cracks) and made the hypothesis that the reason for this is related to the fact that sulphides and carbides tend to have coherent interfaces with the iron matrix. More recently, differences in the fatigue life of steels containing different types of inclusions (silicates, alumina, and calcium aluminates) were reported in experiments where oxygen content and inclusion size were kept constant [89]. Results were interpreted as the consequence of differences in the characteristics of the inclusion-matrix interface. More specifically, cracks were visible before the fatigue experiments at the interface of calcium aluminate and alumina inclusions (probably due to previous forming operations) but were not observed at the interface of steel with silicate-type inclusions, which are correlated with longer fatigue lives.

Finally, it has also been argued that the type of inclusion should have no effect on the fatigue strength of high-strength carbon steels and that the determining parameter should be, in fact, the inclusion size [78]. The particles are thus considered to be mechanically equivalent to voids of similar size. In this perspective, the detrimental effect of calcium aluminate inclusions is thought to be a mere consequence of the fact that those tend to be larger. Along a related line or reasoning, other authors have pointed out that particle-matrix decohesion has been observed after cold or hot forming processes and that voids could thus preexist mechanical testing, giving some justification for the assimilation of inclusions to equally sized voids [54].

2.1.4 Documented properties of oxide inclusions

Given the relevance that oxide inclusions can have for the performance of steel products and their processing, knowledge of the properties of the different types of inclusions themselves has importance. This section summarises data reported on the mechanical properties of non-metallic inclusions. When possible, references are to data collected by directly testing oxide inclusions, but a few values are given for data retrieved from measurements in bulk samples of the corresponding oxide. For other inclusion data, such as information on the crystalline structure, melting point, density, and optical microscopy images, the reader is referred to the book by Kiessling and Lange [84].

Deformability

A direct manifestation of the importance of intrinsic inclusion mechanical properties can be observed in the changes that inclusions undergo when the steel is deformed at different temperatures. For this reason, inclusions are often classified according to their ability to co-deform with steel during metal processing into at least three major groups: i) inclusions that are highly deformable and elongate forming stringers, ii) those that fracture during processing and also lead to stringers that are equally long but composed of multiple inclusions fragments, and iii) inclusions that do not co-deform and maintain a globular or equiaxed shape after

forming operations (Fig. 2.4). The ISO standard for steel cleanliness assessment [90] additionally differentiates inclusions that are elongated and have round edges (sulphide type) from those which are elongated but present sharp edges (silicate type), while some authors also distinguish between ductile inclusions (single phase) and fragile-ductile complex inclusions [4,57].
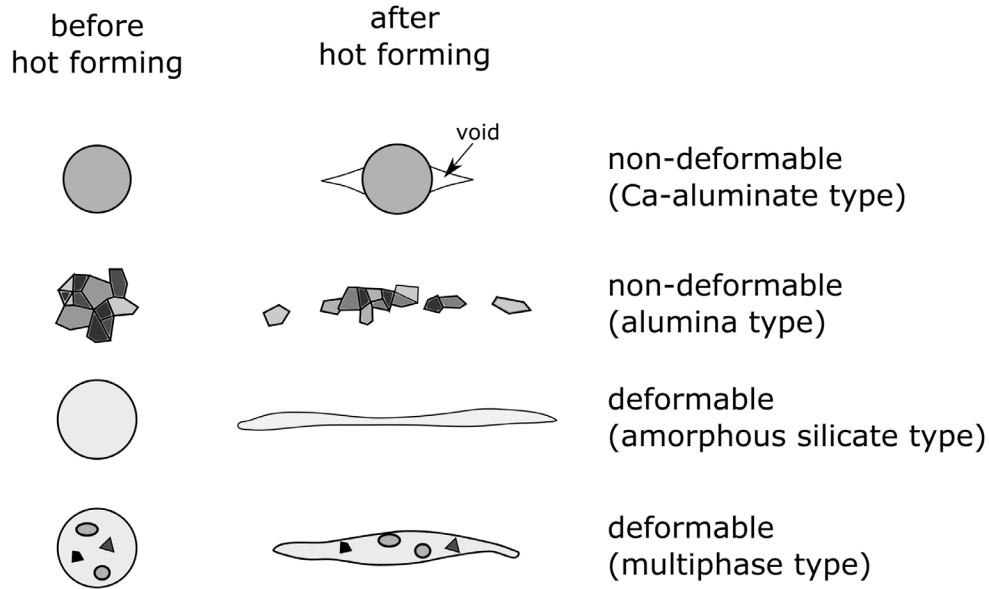

Figure 2.4 Morphologies of different types of oxide inclusions before and after hot forming processes. Redrawn from [91].

In this context, studies aiming at characterising inclusion plasticity usually refer to the inclusion *index of deformability υ*, defined as:

$$\upsilon = \frac{\epsilon_i}{\epsilon_s}$$

where ϵ_i is the inclusion elongation observed after the steel has been subjected to a true elongation of magnitude ϵ_s. Values for the deformability index of up to two have been reported for different oxide inclusions at hot-working temperatures. Nevertheless, for alumina, calcium aluminates and rare earth oxides, the deformability index is considered to be virtually zero [69], Fig. 2.5. As a general rule, crystalline inclusions, or crystalline phases within inclusions, are considered to be non-deformable [91], except for FeO inclusions, which have been reported to have υ values in the range of 0.2 to 0.6 and which, unlike other oxides, have a deformability index that decreases when the deformation temperature increases [84].

The deformability index is related to the ability of the oxide phase to accommodate permanent deformation imposed by the surrounding matrix and therefore measures the amount of ensuing internal damage (in the form of voids or highly strained metal) around the inclusion after deformation processing of the steel. The index is linked to the hardness of both substrate and matrix materials. Theoretical calculations suggest that, for particles that are weakly bonded to the matrix, a low index of deformability is obtained for inclusions with hardness values two times or more above that of the matrix [92,93]. According to those calculations, particles with

strong bonds to the matrix could be deformed even if they have a hardness six times higher than that of the metal [92].
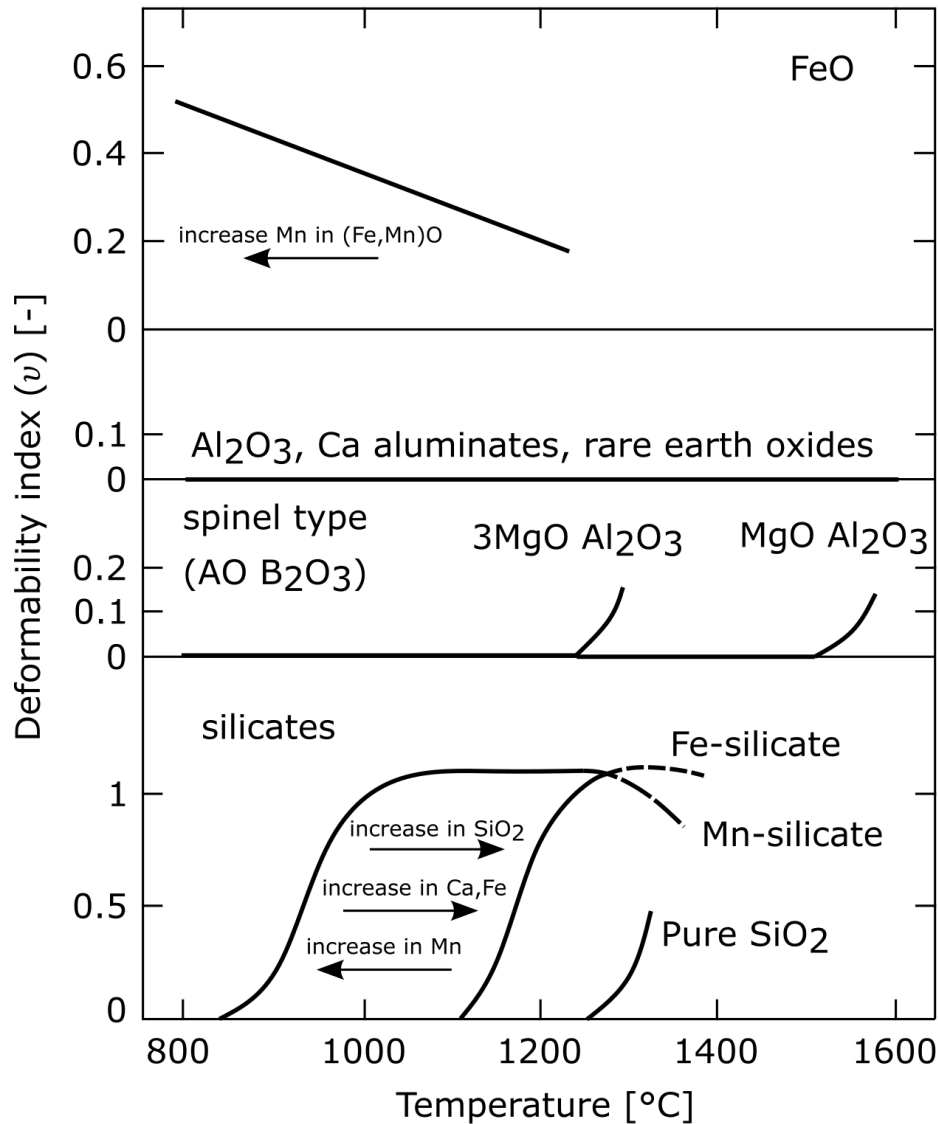
Figure 2.5 Deformability index of different types of oxide inclusions for temperatures in the steel hot forming range. Redrawn from **[84]**.

Deformable oxide inclusions can be obtained when a high fraction of the oxide is amorphous and has a glass transition temperature near the range of forming temperatures. In seeking a path to produce inclusions that are deformable at hot working temperatures, multiple studies have been aimed at identifying low melting point oxides that are either semi-liquid or low-viscosity glasses at a target deformation temperature [16,17,71]. Experimental observations show that for manganese silicate inclusions, there seems to be an optimum amount of Al_2O_3 content of about 15 % leading to low melting point oxides. In contrast, higher alumina contents seem to lead to the precipitation of alumina-rich-phases of low ductility [69]. For calcium aluminate inclusions, empirical observations show that oxides with more than 20 wt.% CaO retain a globular shape through all forming operations [94].

Hardness and elastic modulus

Hardness values provide direct information on the ability of inclusions to deform permanently. Measurements on inclusion phases are often reported at room temperature and on synthetic oxide mixtures; however, with the advent of micro-mechanical testing techniques, an increasing number of reports can be found that probe the hardness and elastic modulus of individual inclusions directly [93,95–97]. A summary of reported inclusion hardness values is presented in Table 2.1.

Reports of the elastic properties of oxide inclusions, which influence the extent of elastic mismatch between the inclusions and the matrix, are scarce. In the literature concerned with inclusions, stoichiometric oxide compositions have received more attention than non-stoichiometric mixed oxide inclusions. Nonetheless, even for the often-present calcium aluminate inclusions, reported values of the elastic properties are rare. The most likely reason for the lack of data on the elastic properties of oxide inclusions is the difficulty in probing small volumes of material, such as those found in non-metallic inclusions. Reported values, measured on single inclusions by using modern instrumented indentation techniques or in bulk oxide phases using methods that are appropriate for bulk materials, are also summarised in Table 2.1.

Thermal expansion coefficient

The coefficient of thermal expansion (CTE) is a relevant inclusion property because thermal expansion mismatch during metal cooldown can lead to the development of residual stresses and can promote the nucleation of voids at the inclusion-metal interface. Reported values in the literature can be found in [87,88,82] or in [94] and are summarised in Fig. 2.6
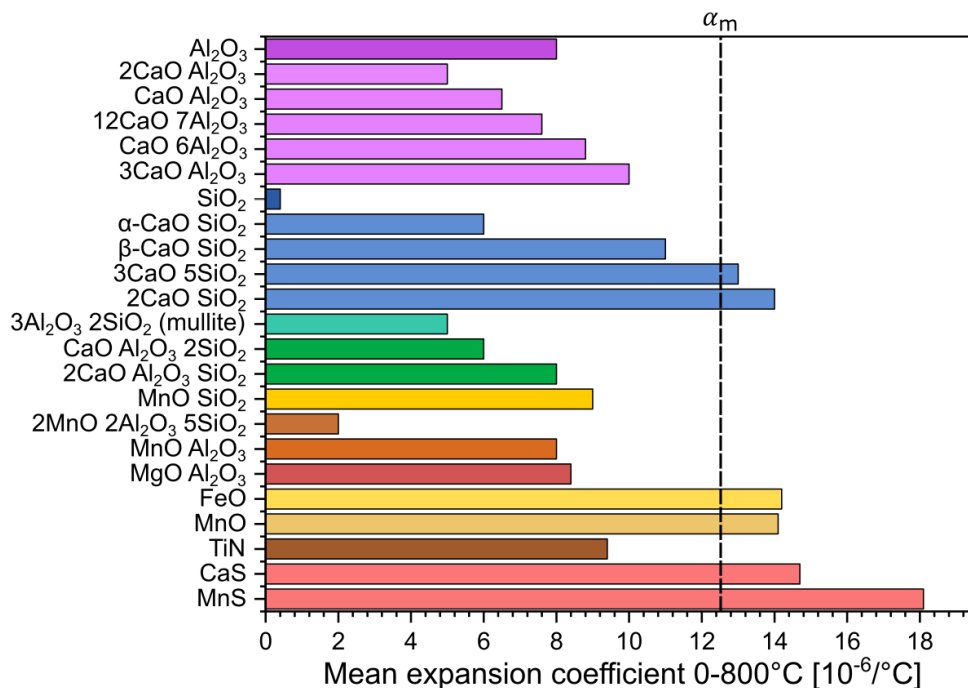

Figure 2.6 Thermal expansion coefficient for different types of inclusion phases in the range of 0-800°C and average expansion coefficient of 1 % C 1.5 % Cr steel matrix from 850 °C to room temperature (dashed line). Redrawn from **[82]**.

Table 2.1 Values of hardness and Young's modulus reported in the literature for non-metallic inclusions and oxide phases observed in inclusions.

Inclusion/oxide composition	Sample nature	Experiment details/obsv.	Hardness (GPa)	Young's Modulus (GPa)	Ref.
Al_2O_3	Inclusion or synthetic oxide [a]	Microhardness	29.5-44.1	-	[84]
	Inclusions	Nanoindentation	32	-	[95]
	Inclusions	Nanoindentation	24.3 ± 3.8	364 ± 30	[98]
SiO_2 (cristobalite/ tridymite/quartz)	Inclusion or synthetic oxides [a]	Microhardness	≈ 15.7	-	[84]
SiO_2 (fused silica)	Reference sample used for calibration in nanoindentation	Nanoindentation	9.5	72	[99–101]
$2SiO_2 \cdot 3Al_2O_3$	Inclusion or synthetic oxide [a]	Microhardness	14.7	-	[84]
$CaO \cdot Al_2O_3$	Inclusion or synthetic oxide [a]	Microhardness	9.1	-	[84]
$CaO \cdot 2Al_2O_3$	Inclusion or synthetic oxide [a]	Microhardness	10.8	-	[84]
	Inclusions	Nanoindentation	9.6	126	[95]
50.9 % CaO -45 % Al_2O_3 -2.3 % SiO_2 - 1.7 % FeO (at. %)	Inclusions	Nanoindentation	-	122 ± 7	[102]
$CaO \cdot 6Al_2O_3$	Inclusion or synthetic oxide [a]	Microhardness	21.6	-	[84]
	Inclusions	Nanoindentation	18.2	195	[95]
$CaO \cdot SiO_2$ (* wollastonite)	Inclusion or synthetic oxide [a]	Microhardness	9.8	-	[84]
	Synthetic oxide (mixing, melting, crushing and sintering)	Microhardness (H) / acoustic resonance (E)	5.5 [(*)]	105.5 [(*)]	[103]
$CaO \cdot 2SiO_2$ (anorthite)	Synthetic oxide (mixing, melting, crushing and sintering)	Microhardness (H) / acoustic resonance (E)	7.4	89.9	[103]

Inclusion/oxide composition	Sample nature	Experiment details/obsv.	Hardness (GPa)	Young's Modulus (GPa)	Ref.
$2CaO \cdot SiO_2$	Inclusion or synthetic oxide [a]	Microhardness	9.6	-	[84]
$2CaO \cdot Al_2O_3 \cdot SiO_2$ (gehenite)	Synthetic oxide (mixing, melting, crushing and sintering)	Microhardness (H) / acoustic resonance (E)	6	116.2	[103]
12 % CaO – 11.7 % Al_2O_3 – 76.3 % SiO_2 (at. %)	Synthetic glass mixture	Nanoindentation	6.3	83.1	[104]
32.5 % CaO - 32.3 % Al_2O_3 - 35.2 % SiO_2 (at. %)	Synthetic glass mixture	Nanoindentation	7.2	103.4	[104]
MnO	Inclusion or synthetic oxide [a]	Microhardness	3.9	-	[84]
$MnO \cdot Al_2O_3$	Inclusion or synthetic oxide [a]	Microhardness	15.6	-	[84]
$MnO \cdot SiO_2$	Inclusion or synthetic oxide [a]	Microhardness	7.4	-	[84]
$2MnO \cdot SiO_2$	Inclusion or synthetic oxide [a]	Microhardness	9.3	-	[84]
$MnO \cdot SiO_2 \cdot Al_2O_3$	Inclusion or synthetic oxide [a]	Microhardness	3.9	-	[84]
$2MnO \cdot 3SiO_2 \cdot Al_2O_3$	Inclusion or synthetic oxide [a]	Microhardness	10.3	-	[84]
$\approx 3MnO \cdot 3SiO_2 \cdot Al_2O_3$	Inclusions	Nanoindentation	10	150	[98]
MnS	Inclusions	Microhardness - room temperature	1-2	-	[93]
	Inclusions	Microhardness - 300°C	0.6-1	-	[93]
	Inclusions	Microhardness - 550°C	0.5	-	[93]
	Inclusions	Microhardness - 750°C	0.35	-	[93]
	Inclusions	Nanoindentation	2	121	[96]

[a] Microhardness values have been measured on oxide inclusions or synthetic oxide mixtures, but information on which phases have been evaluated in which form is not given in the reference.

Matrix-inclusion interfacial strength

It is generally considered that oxide-metal inclusion interfaces are weak and that carbides and nitrides tend to form stronger bonds with the iron matrix than do oxides. This idea is partly due to the observation that voids nucleate at larger strains near (or at the interface with) cementite when compared to oxide particles [105,106]. Unfortunately, quantitative determinations of interfacial strength are complex and, thus, scarce. A few calculations have been reported based on the critical strain at which voids are observed to nucleate at the interface of the iron matrix with inclusions [107], yttria reinforcements [106] or cementite [108,109]. These calculations usually assume that the particle interface strength is the parameter controlling the nucleation of voids. It has been shown, however, that other void nucleation sites are possible. In aluminium matrix composites, it has been shown that the damage mechanism can be determined by the matrix properties, notably its yield strength and work hardening behaviour, in such a way that particle fracture is more prone to be observed for high yield strength and work hardening materials [110]. In addition, other authors considered the mechanism of void nucleation at the interface with second phases during ductile fracture to be a statistical process [111], and there is still debate on whether the damage mechanism is determined by a critical stress or a critical strain [112].

Void nucleation at inclusion-steel interfaces has been reported as a result of forming operations [54,89]. Substantial evidence for the formation of such voids exists, at least for globular calcium aluminate inclusions [84,102]. Numerical simulations show that voids can be created around inclusions during metal working if differences exist between the particle and matrix yield behaviour and that interfacial failure can result either from stresses that are tangential or normal to the particle surface [113].

Reported values for the interface strength between inclusions and iron alloys are presented in Table 2.2. For elongated MnS inclusions, the damage mechanism has been observed to depend on the orientation of the applied stress with respect to the particle. Particle fracture usually takes place when the metal is tested in the longitudinal direction, with inclusions fracturing at stresses in the order of 1120 MPa [60]. Conversely, particle-matrix decohesion has been observed when the metal is tested in the short transverse direction, with an estimated interfacial strength of 810 MPa [60].

Table 2.2 Reported values of the interface strength measured experimentally for different inclusions/precipitates in iron alloys

Particle	Interface strength (MPa)	Reference
Y_2O_3	1000 - 1600	[106]
MnS	1100 - 1400	[107]
	810 ± 50	[60]
Fe_3C	1200 - 2000	[108,109]

2.2 Techniques used for the determination of inclusion properties

The properties of different types of inclusions, or their effect on steel behaviour, have been primarily determined indirectly from macroscopic analysis and simple models of the metal-inclusion behaviour. Such is the case for determinations of the inclusion deformability index or the inclusion-matrix interface strength. Because of the size of NMI, direct determinations of inclusion properties require techniques capable of probing small volumes of material, on the order of a few hundred cubic micrometres. Examples of direct inclusion property determinations comprise hardness measurements and, more recently, elastic modulus determinations through instrumented indentation. The present section summarises micromechanical testing techniques that can directly probe the mechanical properties of oxide inclusions in ferrous alloys. Emphasis is placed on techniques related to those used over the course of this research project, with a focus on the principles of the testing techniques, their main challenges and limitations.

2.2.1 Micromechanical testing

Over the last decades, various testing techniques have been developed to measure mechanical properties at the micrometre level. Initially driven by the need to characterise the behaviour of materials used for micro-electro-mechanical systems (MEMS) [114,115] or the properties of thin films [116], these techniques have also allowed the exploration of the micromechanical behaviour of many other material systems and continued to contribute to a better understanding of the fundamental deformation and fracture processes [117].

Some of the most widespread techniques for micromechanical testing include nanoindentation (see the following section) and micro-compression experiments. The latter are generally performed on pillars of either circular or square cross-sections (*e.g.* see Refs. [118–123] for different materials and geometries); however, studies are also reported on other, more complex structures [124]. Micromechanical tests performed in compression have the advantage of being relatively simple to implement, with force generally applied by a flat punch of hard and stiff material. These can provide information, for example, on the yield stress, deformation mechanisms, and stress-triggered phase transformations. Micromechanical tests in tension are more rich but, comparatively, more difficult to perform because of challenges related to the gripping and alignment of the sample. This has led to a number of custom-designed solutions [125–127], with interesting alternatives being tests performed by the pushing on structures with geometries designed to produce shear stresses [128–130] or more classical bending experiments. The latter have been reported for nano or micrometre-sized fibres [131–135], as three-point bending experiments [136], or as cantilever bending experiments [137–140]. Finally, micromechanical tests have also been designed to study crack propagation [140–146]. For these experiments, chief difficulties at the microscale are the production of a pre-crack on the sample and the achievement of conditions for testing where linear elastic fracture mechanics are obeyed and which ensure stable crack propagation [143,147].

One major challenge faced when performing mechanical tests at a small scale is sample preparation and manipulation. Either because the material already exists or is produced at the micro-scale, or because the interest is on the properties of a bulk existing material, the isolation and handling of specimens require strategies to avoid altering the studied material. A largely used approach, but that is not necessarily free of artefacts [145,148–150], is that of milling the desired sample geometry with a focused ion beam (FIB) into a larger block of the material (*e.g.* Refs. [123,128,142,145,150]). This is usually done on a phase or structure at the surface of bulk material. In addition to allowing manipulation of the (macroscopic) sample with hands/tools, the bulk acts as a fixed end in bending, tensile, or compression experiments, as observed in the examples presented in Fig. 2.7. This approach can be used, for example, for micromechanical test samples produced from bulk material, for thin films that can be maintained attached to their substrate, or for particulates or fibres that are present in a matrix to which they can remain linked [136,151–153]. Other techniques used for the production of small-scale structures or materials amenable for micromechanical testing include advanced additive micro-manufacturing techniques, selective modification of glasses by femtosecond laser processes combined with wet chemical etching [135,154], reactive ion etching [120,155,156], and the use of combinations of micro-casting techniques with chemical dissolution of the mould [157,158].
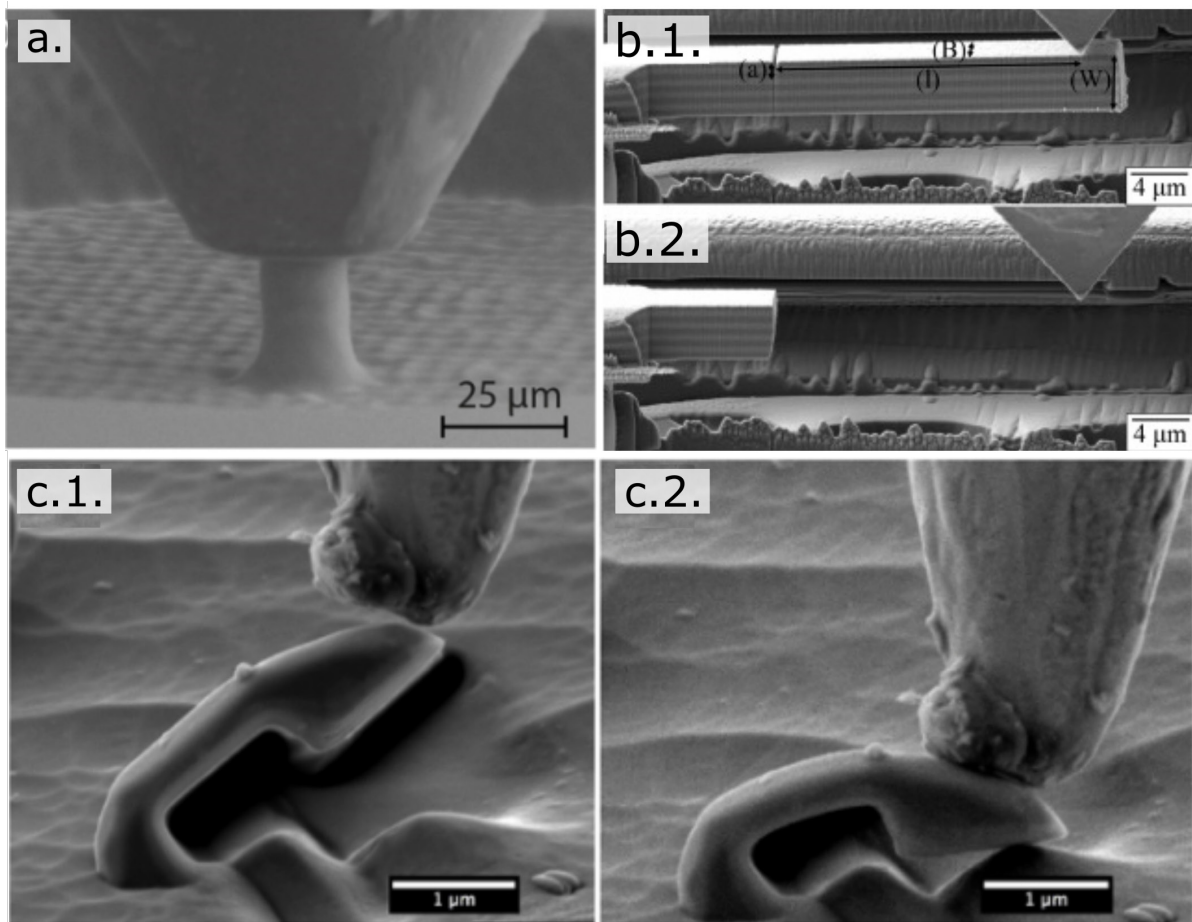

Figure 2.7 Examples of geometries used for micromechanical testing experiments a) pillar compression [154]; b) cantilever bending of notched samples (reproduced from [146] with permission from Elsevier Science & Technology Journals); c) "C-shape" bending for strength measurements (reproduced from [153] with permission from Elsevier Science & Technology Journals).

Among the various existing techniques, micromechanical testing methods have also been designed to probe the strength of microscopic particles while keeping the external surface in a pristine condition. A first example is the meridian crack test, a method suitable for spherical particles that, during testing, are compressed between platens of controlled hardness [159,160]. A loading condition is achieved through an appropriate choice of the platen material in which maximum tensile stresses are reached, either in the inner region of the spherical particle or at its surface, but away from the contact region between the platen and the particles. This method requires probed particles to be highly spherical and to have dimensions that allow their observation using optical microscopy (the diameter of studied particles was from 25 μm to 35 μm). Another technique, employed in this thesis for the determination of oxide inclusion strength, is suitable for smaller particles on the condition that they be i) partially embedded (and partially exposed) in a matrix material and ii) can be machined by Focus Ion Beam (FIB) milling to carve a notch on one of their sides [151–153]. The notched particles are then tested in bending by applying a compressive force, either *ex-situ* or *in-situ* in a scanning electron microscope (*e.g.,* Figs. 2.7 c1 and c2) until failure is observed. The results of the tests, including force-displacement data, are coupled with bespoke finite element simulations to obtain the state of stress and strain on the particles at the point of failure. Because of the "C" geometry of the test, maximum principal stresses are developed in the external surface of the micromechanical test samples. The obtained results are thus not affected by artefacts related to FIB-milling, such as ion implantation or the amorphization of the surface of the sample, which are only expected to be present in the inner part of the notch. Nevertheless, if the particles are exposed on the surface of a material by chemical dissolution of its matrix, special consideration must be taken in selecting a dissolution agent to ensure that artefacts are not originated by interactions between the particle material and the solvent. Under these conditions, the method enables a true measurement of the particle strength.

2.2.2 Nanoindentation

Nanoindentation experiments can be considered to be a specific case of micromechanical testing. These are among the most easily implemented tests and can provide information on the mechanical properties of small volumes of materials, for which the most commonly derived quantities are the hardness (H) and elastic modulus (E).

The extraction of elastic properties values from nanoindentation data is based on a quantitative understanding of the factors affecting the force and displacement measurements observed when forcing the mutual contact of a punch, which acts as a probe, with a flat, semi-infinite, solid. If a certain number of conditions are met by the sample and the nanoindentation tip, the Oliver-Pharr method [161] can be directly applied to extract the hardness and elastic modulus values after analysis of the load-displacement curve. On the one hand, the most important condition that a nanoindentation tip must meet is that it be made of a hard and stiff material, of which elastic properties are known. In addition, its geometrical characteristics are important. The most commonly used tip geometries include pyramidal and spherical indenters, the former having the advantage that it has a self-similar geometry regardless of indentation depth, while, with a spherical indenter, the surface-to-depth ratio during indentation changes a function of the

indentation depth. Because the size of the imprint is usually too small to be measured by imaging the surface of the tested sample, the projected area of the tip as a function of its distance from the apex is usually calibrated by indenting at different depths a reference material of known properties.

In instrumented indentation experiments, the most generally derived quantities are the hardness, H, and the reduced elastic modulus, E_r, of the probed material. These are calculated as:

$$H = \frac{P}{A_c} \tag{2.1}$$

$$E_r = \frac{1}{\beta} \frac{S\sqrt{\pi}}{2\sqrt{A_c}} \tag{2.2}$$

where the indentation load (P) is directly measured during the test, while the unloading stiffness (S) and the corresponding projected contact area (A_c) are derived from the load-displacement curve. Parameter β, which can be taken equal to 1.05 [162], is a constant introduced to correct for deviations from axial symmetry in the indenter geometry. The reduced modulus E_r is a combination of the elastic properties of the indenter (sub-index i) and indented material (sub-index s) defined by:

$$\frac{1}{E_r} = \frac{1-v_i^2}{E_i} + \frac{1-v_s^2}{E_s} \tag{2.3}$$

Oliver and Pharr pointed out that, while the load is being removed, the contact area gradually changes. As a result, the unloading curve is not linear but is better described by a power law function of the form:

$$P = A(h - h_f)^m \tag{2.4}$$

where A and m are fitting parameters, h_f is the final indentation depth, and h is the indenter tip displacement at load P. The unloading stiffness is defined as the derivative of Eq. 2.4 computed at maximum load:

$$S = \frac{dP}{dh}\Big|_{P=P_{max}} \tag{2.5}$$

Oliver and Pharr determined the contact depth (h_c) from the difference between the maximum depth measured during the indentation test (h_{max}) and the elastic sink-in of the sample surface around the indenter. In the absence of pile-up formation, the latter is expressed using Sneddon's solution for the deformation of a half-space under a conical indenter. This leads to the following expression for h_c [161]:

$$h_c = h_{max} - \epsilon \frac{P}{S} \tag{2.6}$$

where ϵ is a constant of value $\epsilon = 0.75$ [161,162].

Accurate determination of the contact depth allows the contact area to be computed after calibration of the tip with a reference material of known elastic modulus. The contact area, A_c, is usually described as a function of the contact depth (h_c) by a function of the form:

$$A_c = C_0 h_c^2 + C_1 h_c + C_2 h_c^{1/2} + C_3 h_c^{1/4} + C_4 h_c^{1/8} \qquad (2.7)$$

where all C_i are fitting parameters, with C_0 usually taken as 24.5 for a Berkovich indenter.

For the analysis to be valid, the sample must be assimilable to a semi-infinite linear elastic solid of homogeneous properties. While it has been shown that permanent deformation around the indenter does not significantly affect the measurements (unless considerable pile-up or sink-in is produced around the indenter) inhomogeneities in the elastic (and plastic) behaviour of the material can be expected to affect the load-displacement curve and thus lead to inaccurate measurements. This is, for example, what occurs when probing the properties of coatings or thin films [163–165], or those of individual phases on multiphase materials or embedded particles [95,166–170]. Those are, paradoxically, the situations where nanoindentation studies become particularly useful (if not the only possible technique) to obtain information on the material properties.

Indentation techniques can also contribute to the study of other properties related to the mechanical behaviour of materials, such as cracking behaviour, strain rate sensitivity, or strain- and stress-triggered phase transformations. In addition, similarly to other micromechanical testing techniques, significant advances are currently being achieved concerning the conditions in which indentation experiments can be performed, with notable improvements in terms of testing environments [171–174] and selection of the testing temperature, which can now be varied from -150°C up to 800°C. Challenges for successful nanoindentation testing at elevated temperatures are the temperature homogeneity across the sample and the possible interference exerted by chemical interactions between the tested material and the probe or grips. In addition, accurate knowledge of the stiffness of the load frame and the indentation tip is essential for nanoindentation experiments, which means that the elastic properties of heated (or cooled) elements need to be known at the testing temperature. This has led to the proposal of complementary techniques performed simultaneously or after indentation experiments to track and analyse changes in the probed material [171,175].

Chapter 3 – Indentation of embedded particles

Disclaimer: This chapter contains mostly literal reproductions of full paragraphs and figures from the manuscript A. Slagter, J. Everaerts, A. Mortensen, Nanoindentation of embedded particles, *Journal of Materials Research* (2023). In this work, the author of this thesis contributed to the derivation of the presented method, to the design of finite element simulations and experiments, and to the implementation of both simulations and experiments. The author was also the writer of the first draft of the manuscript, was active in all following iterations after submission and review and produced the figures.

3.1 Introduction

Instrumented indentation, or nanoindentation experiments, provide a rich source of information on the local mechanical behaviour of materials. The two principal properties that can be derived after nanoindentation of a flat surface are the hardness (H) and elastic modulus (E); these can be calculated with good accuracy using well-established schemes such as that of Oliver and Pharr [161], which build on a solid understanding of the factors affecting measured loads and displacements when indenting a semi-infinite continuum with a hard probe of defined geometry. A review of the Oliver and Pharr method is given in Section 2.2.2.

Data interpretation schemes designed for instrumented nanoindentation rely, however, on several assumptions; among those are: the probed material is assimilated to a homogeneous, semi-infinite solid, and ii) knowledge of the indenter elastic properties is required. Yet, for many of the situations where nanoindentation is interesting, such as probing the properties of small volumes of material or thin films, those assumptions are not met and, as a consequence, specific testing strategies and/or correction techniques need to be implemented in order to obtain meaningful data.

A vast body of literature addresses the extraction of elastic modulus and hardness values from films deposited on substrates of a different material. Interest in using nanoindentation to extract information on the mechanical properties of films on substrates is almost as old as the instrumented indentation technique itself. The first model to correct for substrate effects when measuring the elastic modulus was based on empirical observations and was proposed by Dorner and Nix [176] in 1986. The work of Gao et al. [177] followed a few years later with a model based on moduli-perturbation analysis for multi-layered materials. Over the years, numerous authors have addressed the subject, proposing simpler models, studying the range of validity of existing models, or optimizing them for certain testing conditions or types of material [178,179,164,165,180].

Comparatively, the extraction of the elastic properties of particles embedded in a matrix of different stiffness has been far less explored; yet, the question is relevant to many situations, such as our understanding of multiphase material micromechanics or simply probing phases of small volumes. Experimental approaches have been proposed by Jakes et al. [170] and Buchheit and Vogler [169], who suggested a correction method based on the determination of

a 'structural' or 'system' compliance. The methods generally assume a constant ratio of hardness to modulus squared for the tested material and determine the local extra compliance induced by the surrounding matrix at each indentation location by using either a multiple unloading indentation strategy or a continuous stiffness measurement (CSM) technique.

The problem has also been addressed through numerical simulation. Based on finite element models of indentations performed with a conical indenter on a semi-spherical particle, Yan et al. [167,168] have defined a particle-dominated depth over which the results of elastic modulus determinations are affected to less than 10 % by matrix effects. Their results indicate that the particle-dominated depth depends largely on the ratio of the elastic modulus of the particle to that of the matrix and suggest that the indentation depth should be kept to less than 5 % of the particle radius. Other finite element simulations and experimental measurements were performed by Leggoe [166], with a focus on ceramic reinforcements in metal matrix composites (MMC). It was found that, for indentations performed using a spherical indenter (and for the particle geometries and range of properties analysed), the total displacement experienced by the indenter is what the particle material alone would yield were it to be sufficiently large and not surrounded by the matrix, plus a term accounting for the presence of the matrix. The latter, namely the additional penetration (Δu) of the indenter caused by the presence of the matrix at load *P,* is inversely proportional to the particle diameter (D_p) and is related to the elastic modulus of matrix (sub-index *m*) and particle (sub-index *p*) by:

$$\frac{\Delta u}{P} = \alpha \frac{1}{D_p} \left(\frac{(1-v_m^2)}{E_m} - \frac{(1-v_p^2)}{E_p} \right) \tag{3.1}$$

where α is a proportionality constant, estimated from finite element simulations to be 0.925 for spherical particles (embedded to the equator) and 0.802 for cylindrical particles of depth equal to their diameter.

Finally, the problem was addressed by Lamagnere et al. [95], who studied, by means of nanoindentation, the hardness and elastic modulus of non-metallic inclusions embedded in a steel matrix. Their approach to the problem was to demonstrate, by finite element simulations, that the effect of the matrix on the indentation experiments did not cause deviations that exceeded 5 % of the elastic modulus value, particularly for the range of dimensions of their non-metallic inclusions (assuming those have a spherical geometry) and for the expected elastic properties of particle and matrix. An interesting aspect of their work is that they considered in their simulations particles embedded to different depths (¼, ½ and ¾ of a sphere) and showed that the effect of the matrix on the nanoindentation results would depend not only on the real particle radius but also on its relative depth into the matrix.

We show in the following that an equation close to Eq. 3.1 can be used to calculate an average extra compliance produced by the presence of a matrix around the particle, which can be used to correct both hardness and elastic modulus values gathered after indenting a sufficient number of particles. This extra compliance can be estimated regardless of the type of indenter used and regardless of the difference in elastic properties between matrix and particle. We thus extend Leggoe's results to include spherical and cylindrical particles embedded to different depths, we analyse the conditions under which the extra compliance calculation remains valid, and we

show that a key condition for the approach to be valid is that a sufficient number of particles, on the order of 30 or more, be tested.

3.2 Estimating the matrix-induced change in compliance

When probing the properties of a particle embedded in a semi-infinite material with different elastic properties, there is an extra (positive or negative) displacement induced by the matrix. This has an effect on both the unloading stiffness, S, and the contact depth, h_c, (see Section 2.2.2 for details) and, if not accounted for, it leads to an inaccurate determination of both the elastic modulus and nanoindentation hardness

In Ref. [166], Leggoe proposes viewing the influence exerted by the matrix on data collected by testing embedded particles as being a 'secondary indentation' in the sense that, when probed by nanoindentation, the hard and stiff ceramic reinforcements of metal matrix composites that were probed in his work could be seen to act as indenters themselves, pressed against the more compliant matrix material. In the following, we build on this idea to derive a (more) general expression for the influence exerted by the surrounding matrix on nanoindentation data collected by indenting, at sufficiently low loads, embedded particles in a two-phase particulate material.

The derivation considers only elastic contributions from material situated below the particle material (where deformations are expected to be small) and builds on the principle of superposition of elastic deformations. The resulting equation is thus valid only if (i) the zone of permanent deformation around the indenter is confined to the indented particle in such a way that its size and characteristics are not affected by the presence of the matrix and if (ii) the indentation load is kept sufficiently low such that the matrix does not deform plastically. Condition (i) is generally satisfied if the indentation is kept from the particle-matrix interface at a distance greater than ten times the indentation depth [181]. Condition (ii) requires that the indentation load divided by the in-plane particle surface area remain well below the matrix hardness (or three times the matrix uniaxial yield stress [180]). Under these assumptions, since the extra deformation coming from the matrix is purely elastic, the problem can be analysed in terms of compliances (or displacements at fixed load).

We thus decompose the indenter-particle-matrix system into the addition of smaller ideal sub-systems (Fig. 3.1). In this construction, the short-range deformations (elastic and plastic) immediately around the sharp indenter are considered to be identical (i) in a semi-infinite homogeneous sample entirely made of particle material (A in Fig. 3.1) and (ii) in the embedded particle (T in Fig. 3.1). Beyond the particle/matrix interface, all strain is assumed to be well within the range of linear elastic deformation in either A or T of Fig. 3.1. Given that the material in these two systems differs, strain fields beyond the particle/matrix interface are not the same in A or T of Fig. 3.1.
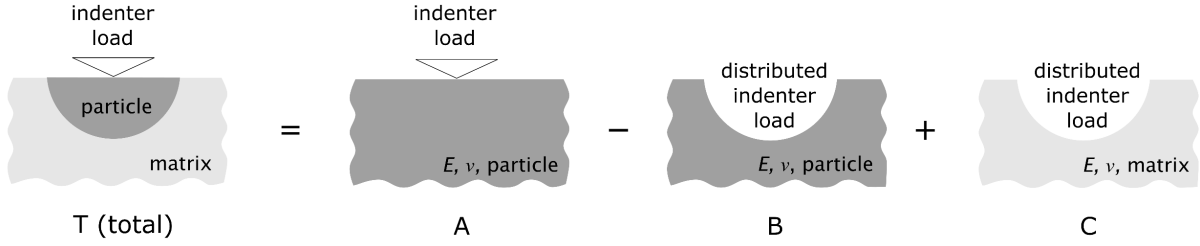
Figure 3.1 Schematic representation of the idealized sub-systems into which the total compliance (C_T) of an indented particle embedded within an elastically different matrix can be divided (see text for details).

Having assumed that the difference between the indented embedded particle and a semi-infinite material with particle properties is to be found in the material (and ensuing deformation) beyond the particle, then the total displacement of the indenter tip in T can be expressed as the total displacement in A minus the displacement in B (this difference represents the total tip displacement in T due only to strain within the particle), plus the displacement in C. The total system compliance (the inverse of its stiffness S) can then be expressed as the following linear combination of the compliance of each of the three sub-systems:

$$C_T = C_A - C_B + C_C \tag{3.2}$$

To (approximately) compute compliances in B and C, we assume that the probed particles can themselves be considered to act as an indenter (the nature of which is unimportant since terms related to its elastic constants cancel out in $C_C - C_B$, see Eqs. 2.2 & 2.3).

The terms in Eq. 3.2 can then be described as follows:

C_A is the compliance of a uniform semi-infinite solid having properties of the particle when it is indented under the same indenter and conditions as the embedded particle;

C_B is the compliance that would be displayed by a uniform semi-infinite solid having properties of the particle when it is probed with an indenter of shape and dimensions equal to those of the particle;

C_C is the compliance of a uniform semi-infinite solid with properties of the matrix when it is being probed with an indenter of shape and dimensions equal to those of the particle.

In other terms, the elastic contribution of the matrix results in an "extra" (positive or negative) compliance ΔC which can be defined as the difference between the compliance observed experimentally in the composite system, C_T, and the compliance, C_A, that would be observed in a semi-infinite (homogeneous) material having the unknown particle elastic properties:

$$\Delta C = C_T - C_A \tag{3.3}$$

Note that C_T can be measured experimentally while C_A is the compliance-corrected value that would lead to an accurate determination of the elastic modulus of the particle material alone following established schemes such as the Oliver-Pharr method. Under present assumptions, from Eq. 3.2:

$$\Delta C = -C_B + C_C \tag{3.4}$$

The assumption made here, namely that the particle acts as an indenter in the matrix, is essentially equivalent to considering that the indented particles are: (i) infinitely rigid (the imposed particle displacement field is uniform); (ii) have a frictionless interface with the matrix (only forces that are perpendicular to the particle-matrix interface and that push on the matrix are transferred); and (iii) that the indented particles are much smaller than the composite sample. If these approximations can be made, then the compliance (C) of each of the two ideal sub-systems B and C in Fig. 3.1 can be written as:

$$C = \alpha \frac{\sqrt{\pi}\,(1-\nu^2)}{2\sqrt{A}\,E} \tag{3.5}$$

where E and ν denote the Young's modulus and Poisson's coefficient of the indented material, and A denotes the projected contact area of the particle assimilated to an indenter. Note that Eq. 3.5 naturally has the same form as Eq. 2.2, but written in terms of the compliance (C) instead of the stiffness (S), since $S = 1/C$. We have also replaced the factor $1/\beta$ (of Eq. 2.2) by a slightly more general parameter α characteristic of the indenter (β is a constant traditionally considered in the literature to account specifically for the lack of axial symmetry of a pyramidal indenter). In Eq. 3.5 α is then a proportionality constant, theoretically equal to unity for a uniform displacement imposed with a punch of axisymmetric geometry, but whose value will vary if, for example, the indented particles (acting as indenters themselves) do not present axial symmetry [178,182], or if the interfacial pressure distribution deviates from that corresponding to an imposed uniform displacement [183].

An underlying assumption in the present derivation is that the remaining matrix material can be regarded as a homogeneous and continuous solid. In a material where the particles represent a minority phase, the matrix and surrounding particles can generally be assimilated to the matrix. If the particles represent a large fraction of the material, then the matrix will probably be better represented by the composite material. In what follows, we consider the former case and thus take the matrix material past the particle/matrix interface to be the (unreinforced) matrix. For a highly loaded two-phase material, the approach proposed here remains unchanged; however, iteration might have to be used to deduce particle properties since the matrix elastic modulus is calculated using particle properties. Alternatively, one might, in such a case, use results from measurements of the composite elastic properties, *i.e.* by indenting the particle/matrix composite with a probe much larger than the particles to define the matrix compliance to be used in computations.

Substituting Eq. 3.5 into Eq. 3.4, the following expression for the extra compliance is obtained:

$$\Delta C = \alpha \frac{\sqrt{\pi}}{2\sqrt{A_p}} \left(\frac{(1-\nu_m^2)}{E_m} - \frac{(1-\nu_p^2)}{E_p} \right) \tag{3.6}$$

where A_p is the projected contact area of the particle (acting as a secondary indenter), and subscripts p and m designate particle and matrix, respectively.

For particles with a circular cross-section, the term $\frac{\sqrt{\pi}}{2\sqrt{A_p}}$ is equivalent to $\frac{1}{D_p}$, with D_p the diameter of the particle cross-section visible along the surface of the sample. Eq. 3.6 then takes the same form as that proposed by Leggoe [166] (Eq. 3.1).

In summary, the above derivation shows that the extra compliance resulting from the difference in stiffness between the particle and its surroundings depends on the matrix and particle elastic constants and on the dimensions of the probed particle through the square root of its projected contact area. Results of the above derivation are, within assumptions made, valid for indentations performed with any indenter and for any combination of elastic modulus, as long as particle indentation itself is not affected and the particle can be seen as a secondary indenter.

3.3 Corrected computation of E and H

Corrected values for E and H can be computed after determining the extra compliance, ΔC, caused by the presence of the matrix. As expressed by Eq. 3.6, ΔC can be calculated knowing the particle dimensions and the elastic properties of both particle and matrix. The matrix reduced modulus, if not already known, can generally be probed directly by nanoindentation of the matrix material, provided that it can be obtained free of particles, or if the volume fraction of particles is sufficiently low such that the presence of the particles does not significantly affect matrix indentation. Determining the particle elastic modulus, however, is usually the aim of the indentation measurements, and therefore an accurate value of ΔC is generally not immediately available. In this situation, the average initial (raw) value of the particle reduced modulus obtained by probing embedded particles can serve to compute an initial value for ΔC. This initial value can then be used to make a first estimation of the corrected elastic modulus, and this value can once more serve to calculate a second, more accurate, approximation of the elastic modulus. Following this procedure, iterations can be performed until the difference between corrected elastic modulus values before and after the last iteration falls below a chosen value.

Once ΔC is known (or estimated by iteration), then the unloading stiffness, S^{corr}, can be simply corrected as:

$$S^{corr} = \left(\frac{1}{S} - \Delta C\right)^{-1}.$$

(3.7)

The contact depth can then be corrected, again on the hypothesis that the short-range displacements around the indenter are not modified by the presence of the matrix. The measured displacement is then the sum of displacements caused by (i) permanent deformation within the indented material plus (ii) displacements emanating from the elastic sink-in of the indenter into the particle and (iii) elastic sink-in of the particle into the matrix. Under this assumption, and if the elastic sink-in of the matrix around the particle can still be described as if the particle was an indenter (that is, if Sneddon's solution for the displacements around an axisymmetric indenter is also valid for the particle indenting the matrix), then the corrected contact depth h_c^{corr} can be computed, following Eq. 2.6 (Section 2.2.2), as:

$$h_c^{corr} = h_{max}^{corr} - \epsilon P(C^{corr})$$

where both terms on the right-hand side are corrected for the extra compliance, namely $h_{max}^{corr} = h_{max} - P\Delta C$, and $C^{corr} = C - \Delta C$. Therefore:

$$h_c^{corr} = (h_{max} - P\Delta C) - \epsilon P(C - \Delta C)$$

$$h_c^{corr} = h_{max} - \epsilon PC + \epsilon P\Delta C - P\Delta C$$

$$h_c^{corr} = h_c - P\Delta C(1 - \epsilon) \tag{3.8}$$

where h_c is the raw value for the contact depth (calculated from h_{max} according to Eq. 2.6, Section 2.2.2). With this corrected value of the indenter/particle contact depth, a corrected value of the contact area (A_c^{corr}) can, in turn, be computed using the contact area expression (Eq. 2.7, Section 2.2.2) and parameters corresponding to the tip area calibration. Corrected values for the reduced modulus and the hardness of the probed material can then be calculated as:

$$E_r^{corr} = \frac{1}{\beta} \frac{S^{corr}\sqrt{\pi}}{2\sqrt{A_c^{corr}}} \tag{3.9}$$

$$H^{corr} = \frac{P}{A_c^{corr}} \tag{3.10}$$

3.4 Finite Element Calculations

The preceding derivation aims to account for the influence exerted by elastic inhomogeneity on indentation data generated when probing individual particles embedded within a two-phase material. Its premise is, following the derivation by Leggoe [166], that indented particles can be viewed as a second large indenter that probes its surrounding material viewed as an elastic continuum. Equation 3.6 makes no assumption regarding the shape of the particle; however, this is bound to exert an influence. Leggoe [166] assimilated the particle to a half-sphere or to a cylinder as tall as its radius; however, even if the particles can be assimilated to spheres, there is a difference between the response of a hemisphere and that of a shallow spherical shell or a nearly whole embedded sphere, as shown by [95].

Finite element models were therefore constructed to simulate variously embedded isotropic linear elastic spherical particles, as well as cylinders of different aspect ratio and axis normal to the plane of polish, pushed into a large body of surrounding homogeneous isotropic linear elastic "matrix" material. These were built using Abaqus/CAE 6.14-1 (Dassault Systèmes Simulia Corp., Providence, RI, USA, 2014). 2D axisymmetric models were built using CAX4R elements, and the indenter probing the particle was modelled as an analytic rigid cylindrical punch. The particle and the surrounding continuum were modelled as isotropic linear elastic solids. Details of the geometry and dimensions of the models are presented in Fig. 3.2. The mesh was validated by comparing the results with the analytical solution for the compliance of a flat punch acting on a semi-infinite solid with homogeneous properties, refining the mesh until the deviation fell below 2 %.
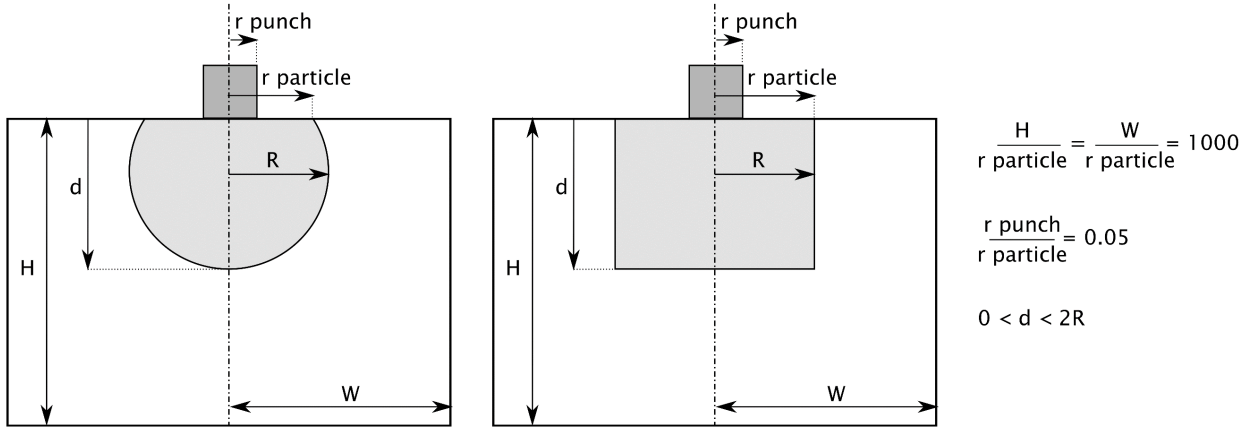
Figure 3.2 Schematic representation of the geometry and dimensions used for finite element simulations.

For the first round of models, perfect bonding was assumed between the particle and the matrix, the interface between the two being simply defined by an abrupt change in elastic properties. In order to explore the effect of the interface bond strength on the dimensionless compliance, a second round of models was run with all parameters remaining the same except for the properties of the interface between the particle and matrix, which was taken to be frictionless.

In the simulations, a fixed displacement was imposed on the punch while the resultant reaction force in the direction of the imposed displacement was used to calculate the compliance of composite systems (C_T) and monolithic systems (C_A). The difference between C_T and C_A was computed for different particle elastic modulus values and represents a determination of ΔC for each simulated particle geometry, size, and combination of particle and matrix elastic properties. These values were subsequently made dimensionless to highlight the fact that obtained results are not limited to the chosen particle dimensions and elastic modulus in the simulations but rather scale with those. We, therefore, made dimensionless the finite element results by the elastic properties of the particle and the diameter of the particle along the surface of the sample (D_p), such that:

$$\Delta C^{adim} = \Delta C \, D_p \, \frac{E_p}{(1-\nu_p^2)} \tag{3.11}$$

Therefore, Eq. 3.6 can be expressed in dimensionless form by combining Eq. 3.6 and Eq. 3.11 to give:

$$\Delta C^{adim} = \alpha \left(\frac{(1-\nu_m^2)E_p}{(1-\nu_p^2)E_m} - 1 \right) \tag{3.12}$$

3.5 Results

Figure 3.3 presents the results of the finite element simulations in a plot of the dimensionless compliance, ΔC^{adim} versus $\frac{(1-\nu_m^2)E_p}{(1-\nu_p^2)E_m}$ (see Eq. 3.12) for (a) spheres and (b) cylinders, both with a fully coherent interface, and (c) spheres assuming a frictionless interface.

Deduced values of α, calculated by a least-squares fit of points in Figs. 3.3 a, b & c are plotted in Fig. 3.3 d versus the ratio of the particle depth (d) to diameter ($2R$). As seen, α varies with the particle relative depth but remains essentially the same regardless of whether the particles are spherical or cylindrical, or are spheres loosely bonded to the matrix except, in this last case, for particles embedded to less than the equator, for which the value of alpha remains approximately equal to unity.
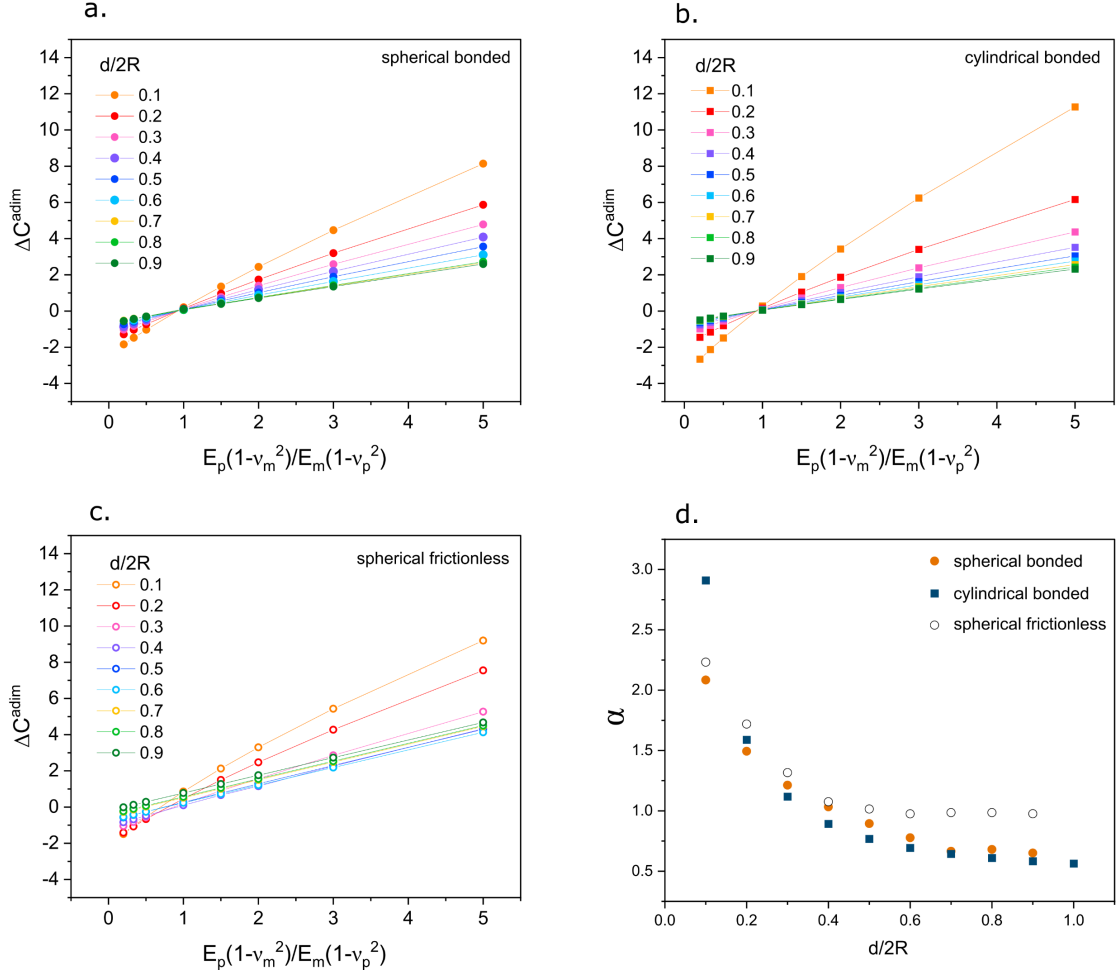

Figure 3.3 a) b) and c): dimensionless compliance ($\boldsymbol{\Delta C^{adim}}$) versus $\frac{(1-\nu_m^2)E_p}{(1-\nu_p^2)E_m}$, computed from finite element simulations of particles embedded to different relative depths in an isotropic elastic matrix having different elastic constants (depths, d, expressed as a fraction of the particle diameter, $2R$). a) spherical particles with a perfectly bonded interface; b) cylindrical particles with a perfectly bonded interface; c) spherical particles with a frictionless interface; d) value of the slope obtained by minimum square fit of lines in a) to c).

3.6 Discussion and experimental implementation

Finite element simulations show that Eq. 3.6 (or in dimensionless form Eq. 3.12) adequately captures, for simulated geometries, the extra compliance caused by elastic modulus inhomogeneity between the surrounding matrix and the indented particle. This can be seen in

Figs. 3.3 a to c: although there is a small deviation from linearity at high values of $\frac{(1-\nu_m^2)E_p}{(1-\nu_p^2)E_m}$,

this remains negligible and the observed behaviour remains close to linear for all explored particle depths. Equation 3.12, which was derived by assimilating the particle to a punch pressed onto the matrix surface, thus leads to an appropriate functional description of indentation, even by deeply embedded non-conical indenters.

The value of the proportionality constant α, however, appears to not only be different from unity (the expected value of α for a particle with axial symmetry acting as a rigid indenter) but also to vary with the depth to which the particle is embedded below the matrix surface. In practice, this creates a difficulty, given that it is generally not possible to guess the particle depth or true diameter when viewing only its intersection with the free surface along which nanoindentations are conducted. Though not constant, however, the values of α vary within a relatively well-defined range, which for the studied cases is $0.5 < \alpha < 3$. We therefore propose that, if a large number of particles is tested within a sample, then by averaging data under the assumption that the depth to which the particle is embedded in the matrix relative to the plane of polish varies randomly, the proper materials properties can be obtained if an average value of α is used in data interpretation.

From the results of simulations performed here, calculated average values of α give $\bar{\alpha} = 1.06$ for spherical particles with a coherent interface, $\bar{\alpha} = 1.41$ for spherical particles with a frictionless interface, and $\bar{\alpha} = 1.09$ for cylindrical particles with a coherent interface. The relative insensitivity of $\bar{\alpha}$ to the particle shape suggests that, if the particle can be taken to be well bonded to the matrix, then relatively accurate results might be obtained by taking $\bar{\alpha}$ only slightly above unity.

We test and illustrate this averaging approach using two composite systems. Both feature silica-based glass particles, which are embedded in a matrix of respectively higher and lower elastic modulus than the particles (Fig. 3.4). The volume fraction of particles in each system was not measured directly but is sufficiently low that interactions between neighbouring particles can be neglected and that the elastic modulus of material surrounding each particle can be taken to be that of the matrix.

For the first system, a composite material made of roughly equiaxed soda-lime glass fragments embedded in epoxy was fabricated by grinding an optical microscope glass slide with a mortar and pestle and then sieving the powders to isolate particles retained between sieves with holes of side length 40 and 20 μm. The glass slide could be probed independently, such that the modulus of the particles was known and the method could be tested for its accuracy.

For the second system, roughly spherical silica inclusions 2 to 5 μm in diameter embedded in iron were tested. These samples were fabricated by melting oxygen-containing high-purity iron and then deoxidizing the liquid metal with a Fe-5 %Si prealloy. During deoxidation, the added silicon combines with the oxygen in the melt to form oxide inclusions, which remain in the metal structure after cool-down and solidification (details of the sample fabrication can be found in Chapter 4, and more specifically, results shown here correspond to Sample Si_CC). The nanoindentation results for those silica inclusions were compared to indentations performed on a fused silica reference sample used for calibration of the tip area function,

assumed to come close to (but not necessarily to equal, given the density-dependence of silica glass properties) the silica making the inclusions.

All indentations were made using a Hysitron TI-950 apparatus (Bruker, Billerica, Massachusetts, US). Accurate positioning of the indents on the particles was possible thanks to the 500 nm XY axis resolution while positioning the indenter. The scanning capability of the instrument was used to provide an image of each tested particle before and after the tests, of size 50 x 50 μm for the glass slide in epoxy and size 10 x 10 μm for the silica inclusions in iron. The area of the indented particles along the surface was measured from such images using the *Image J* software for image analysis [184]. For the monolithic samples (glass slide or silica calibration piece), arrays of >100 indents were performed using a separation between indents greater than 50 μm.

The extra compliance, ΔC, was calculated using Eq. 3.6 with $\alpha = 1.06$ for the silica inclusions in iron (based on the observation that those where generally spherical), and with $\alpha = 1.075$ for the glass fragments embedded in epoxy, this being the average of calculated $\bar{\alpha}$ values for spherical and cylindrical particles strongly bonded to the matrix. Measured reduced modulus values were used instead of $\frac{E}{(1-v^2)}$ in order to avoid assuming Poisson's coefficients for the matrix or tested particles (note that the elastic properties of the indenter are also involved in computing the measured reduced modulus; however, its effect is cancelled since it affects equally the particle and matrix material). An exception was made for the elastic properties of the metallic matrix, since pile-up development when indenting the metal leads to an underestimation of the contact area and an overestimation of the elastic modulus of the matrix. Elastic properties of the iron were therefore assumed to be $E = 210$ GPa and $v = 0.3$, which in combination with a diamond tip having $E = 1140$ GPa and $v = 0.07$ lead to a reduced modulus for iron of 192 GPa.
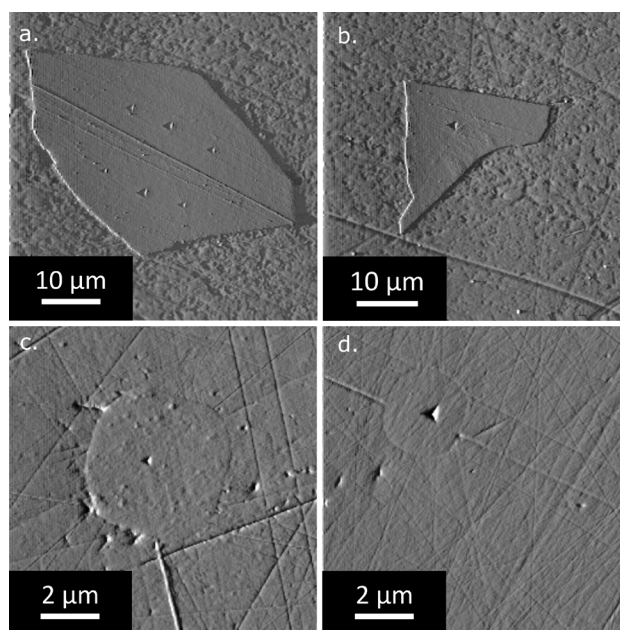

Figure 3.4 Images obtained by scanning the surface of probed particles with the Berkovich tip after indentation; a) & b) glass-slide fragments in epoxy resin, c) & d) silica inclusions in iron.

Equations 3.7 to 3.10 were used to compute the corrected modulus and corrected hardness. Once a corrected value for the reduced modulus was obtained, a new iteration for the calculation of the extra compliance (and other quantities) was made, since the corrected value represents a better estimation of the real modulus of the indented particles than the original, uncorrected, measurement. Iterations were repeated until the difference in reduced modulus between iterations (average values) was below 2 GPa. This was achieved in all cases after less than 3 iterations.

Measured hardness and reduced modulus values for indented particles, before (larger blue circles) and after (orange squares) the derived correction, are presented in Fig. 3.5, along with results obtained for their monolithic counterparts (smaller black circles). Corrected data points (orange squares) for both systems in Fig. 3.5 are computed as if the particle modulus was unknown, meaning by iteration as described above (starting with the average apparent indented embedded particle modulus and iterating from there).

Two observations emerge. The first is that data are strongly dispersed, both before and after the correction. Corrected data can even on occasion (*e.g.,* Fig. 3.5 a) be more dispersed than are the raw data. A reason for this is that the correction of measured compliances tends to shift by a greater amount data points for which the measured stiffness is higher (see Eq. 3.7).
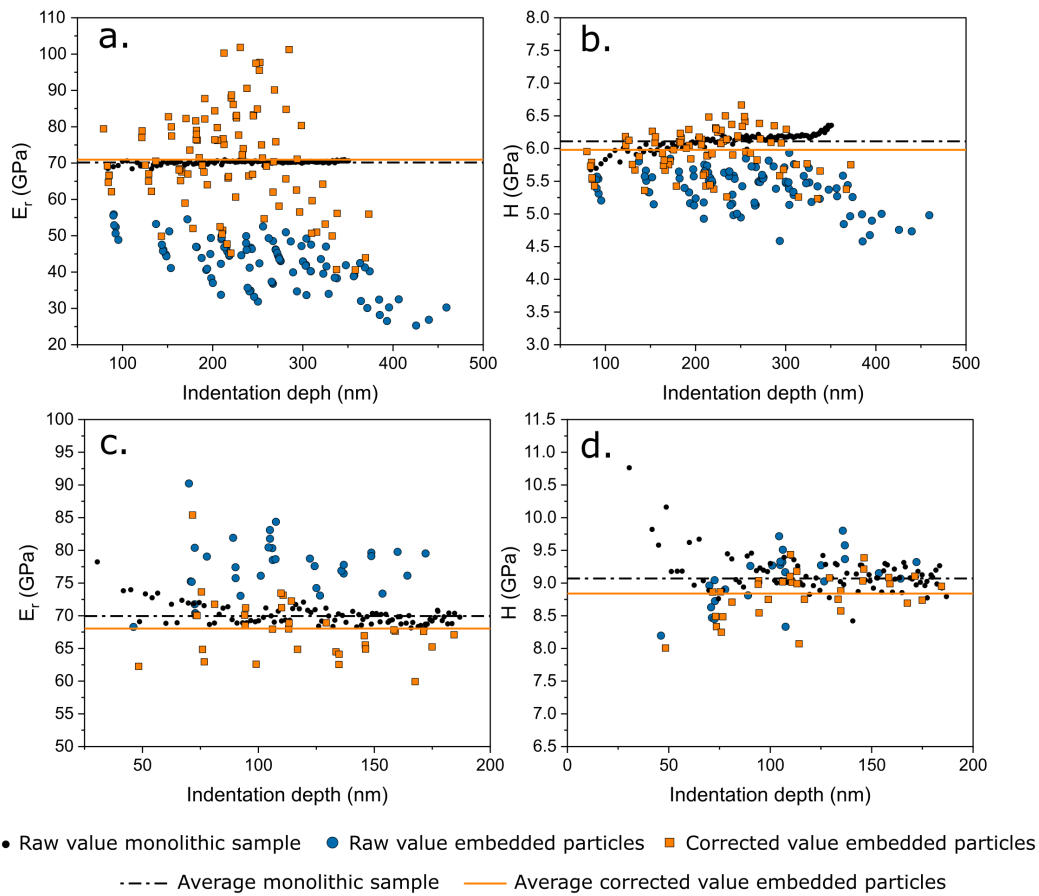

Figure 3.5 Reduced modulus and hardness values obtained by nanoindentations performed on a) & b) glass particles embedded in epoxy, and c) & d) silica inclusions in iron. Results after implementation of the present iterative correction procedure are compared with similar values obtained by indenting a monolithic sample with the same composition.

The second observation is that there is a good agreement between the *average* of corrected indented particle values and the results obtained from the monolithic samples. The dispersion in obtained modulus or hardness values measured by indenting embedded particles can be explained by (i) variations in particle morphology or depth, which affect, as shown above, the value of α, and by (ii) variations in the particle size, which enters (for a given indentation) the extra compliance through the square root of the particle area along the surface of the sample (Eq. 3.6). By adopting a constant (average) value for alpha, the outcome is that corrected values are not necessarily less dispersed than raw values but display the right average after correction. Provided a large number of particles are tested and provided the depth at which those particles are intercepted by the plane of polish is random, then the average corrected value lies close to the real modulus (and hardness) of the particles, as can be observed in Fig. 3.5 by comparison of the average over all corrected data points (orange continuous line, computed as if the particulate relative stiffness was unknown), and the average of values measured with the two particulate materials in bulk form (black dashed-dotted line). We have not sought to evaluate the correlation between precision and number of particles tested; however, present data show that around 10 % precision or better is obtained by testing 30 or more particles, whereas the average of raw data can be off by as much as 40 % (see reduced modulus data in Fig. 3.5). It can also be noted in Fig. 3.5 that the elastic inhomogeneity has a larger influence on the apparent (uncorrected) elastic modulus than it has on the apparent hardness. This is not surprising since the matrix effect is primarily observed on the unloading stiffness. Still, since the stiffness enters the contact depth determination and hence the computation of the tip area function, if the extra compliance is large, then the induced variation in the contact area, and hence in the hardness, is also significant (Fig. 3.5 b). This holds even if the plastic deformation build-up around the indenter has not changed, and even if the matrix has remained in the elastic regime.
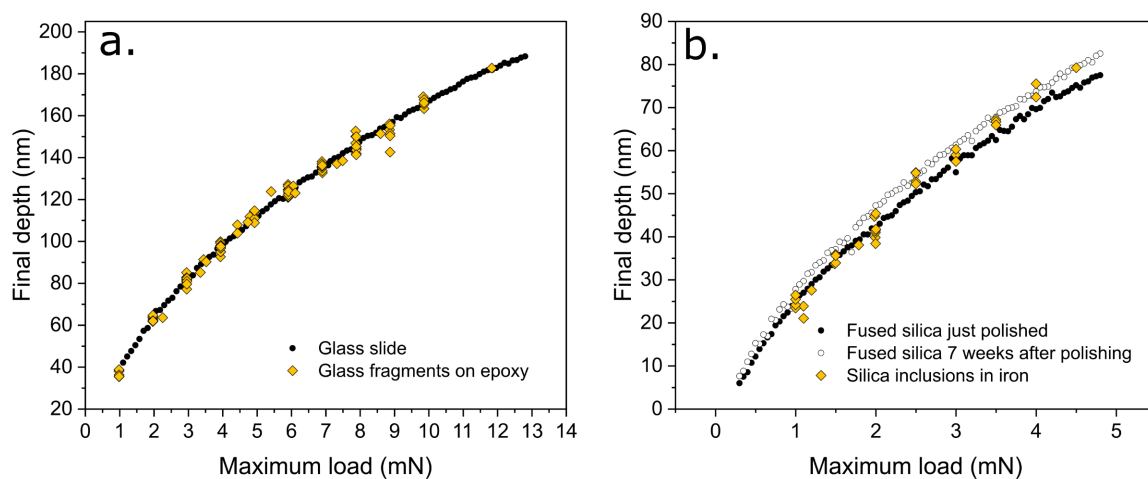

Figure 3.6 Final depth versus maximum load for indentations performed on: a) soda-lime glass (glass slide and glass-slide fragments on epoxy) and b) pure silica (fused silica and silica inclusions in iron).

Empirical evidence showing that the permanent deformation in the particle around the Berkovich indenter is not altered by the matrix can be found by comparing the final depths of indentations performed on embedded particles with those performed on their monolithic counterparts at equal peak load. This is because final depths, unlike (nanoindentation) hardness

values, are not affected by the compliance of the system and give a true indication of permanent deformation processes under the indenter. Figure 3.6 presents final depth measurements on the embedded glass slide fragments and on the silica inclusions compared with those obtained in their semi-infinite counterparts. For the glass fragments in epoxy, the final depths of indents performed on individual particles are in good agreement with those observed for its macroscopic counterpart. For silica inclusions, indentations on the fused silica reference sample were performed not only immediately after polishing the surface of the sample with a diamond suspension (down to 0.1 μm) but also, for the same sample, seven weeks after the polishing was performed. It is observed that final depths for indentations performed on silica inclusions generally lie between those observed for the just-polished sample and the "aged" surface, with the final depth in the latter always being slightly larger than in the freshly polished sample. This variation over time on the final depth observed in fused silica samples is associated with the formation of a soft, hydrated layer on the surface of the silica, which leads to a small increase (2-4 nm) of the permanent deformation depth when the sample is left in an environment containing moisture [185,186].
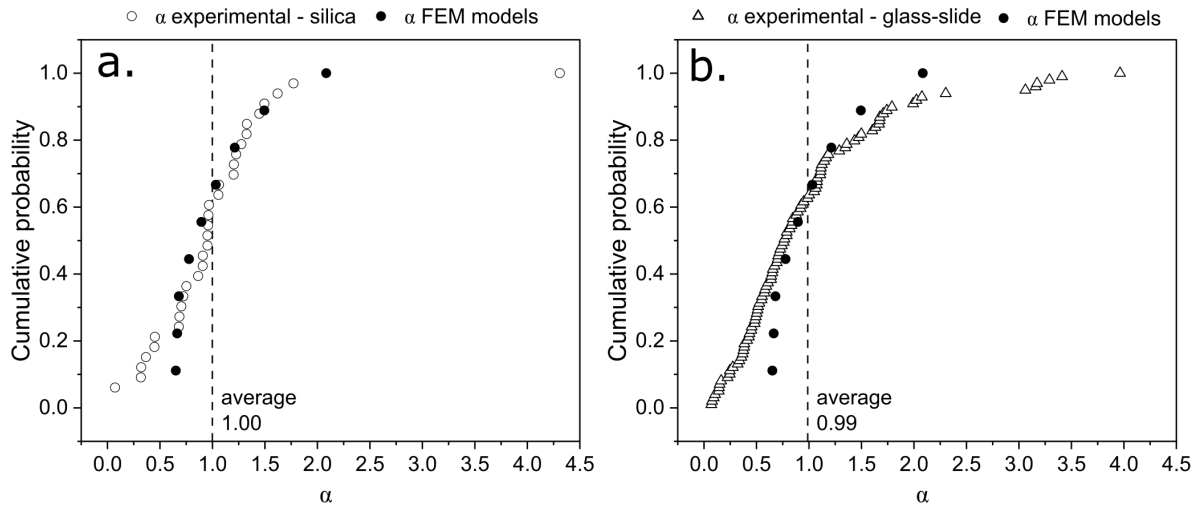

Figure 3.7 Cumulative probability function of alpha values obtained by finite element simulations (spherical particles fully bonded to the matrix shown here) compared with those obtained in a) experiments performed on silica inclusions in iron and b) glass-slide fragments in epoxy.

As a final check, the reduced modulus of the monolithic samples, in conjunction with experimental data obtained by probing the embedded particles and the matrix properties, was used to back-calculate the value of alpha that would correspond to the deviation observed in each of the measurements performed on individual particles. In order to do this, the extra compliance associated with each single indentation was calculated using Eq. 3.3:

$$\Delta C = C_T - C_A$$

with C_T the (experimental) compliance of each indentation performed on a particle, and C_A the (experimental) compliance of a similar indentation performed in its monolithic counterpart and at the same peak load. Each compliance value was computed as the inverse of the experimentally measured unloading contact stiffness. Then simply reorganizing Eq. 3.6, the corresponding value of alpha was computed as:

$$\alpha = \frac{\Delta C \, 2\sqrt{A_c}}{\sqrt{\pi} \left(\dfrac{(1 - \nu_m{}^2)}{E_m} - \dfrac{(1 - \nu_p{}^2)}{E_p} \right)}$$

with A_c the area of the particle measured along the surface of the sample.

Figure 3.7 shows the cumulative probability distribution function for (i) the values of alpha observed experimentally (open symbols) and for (ii) values calculated by finite element simulations (filled symbols). Exception made for tail ends of the distributions (which can be affected by a number of factors, such as an embedded particle depth so shallow as to affect particle indentation itself), the agreement is satisfactory, not only for the silica in iron inclusions (Fig. 3.7a), which are known to have (in most of the cases) a spherical morphology, but also for the glass fragments in epoxy, which have a morphology that clearly deviates from being spherical.

3.7 Summary and conclusions

A method is proposed to correct data for the influence of elastic inhomogeneity when probing by nanoindentation particles embedded in a given different matrix, with a goal to enable the measurement of the reduced modulus and hardness of phases that are unavailable in bulk form, either because they are particulate or because they were precipitated within another, solid matrix phase. The method is defined by estimating the extra compliance (positive or negative) that is induced by the matrix in the nanoindentation signal.

Implementation of the method requires measurements of:

i) the area of the particle along the surface on which indentations are placed;

ii) the nanoindentation response of the particulate material to indentations separated from the particle/matrix interface by at least ten times the indentation depth and conducted on a sufficient number of particles (30 or more seems appropriate)

iii) the elastic (or reduced) modulus of the matrix;

iv) a first estimation of the elastic (or reduced) modulus of the indented particle. This can be obtained by averaging raw nanoindentation data collected on the embedded particulate material.

Provided those 30 or more particles are selected randomly and tested along a polished surface, then if Eq. 3.6 is applied with $\alpha = 1.075$ on data from each particle and resulting values are averaged across all measurements, after iteration and convergence, the scheme provides a reasonable correction for the influence of the matrix compliance on nanoindentation measurements, giving access to the intrinsic reduced modulus and hardness of the material making the particles. The method was implemented and its efficiency was demonstrated on two systems of opposite phase stiffness contrast.

Chapter 4 – Production and properties of oxide inclusions in iron alloys

This chapter describes experiments by which iron samples containing oxide inclusions were produced with the goal of characterizing the resulting inclusion composition, structure, stiffness, and hardness. Deoxidation was performed on iron melts containing oxygen, using a selected number of the most commonly used deoxidizing agents, namely Al, Si, Ca and Mn. The experimental set-up and results of deoxidation experiments are described, including a description of observed inclusion morphologies and chemical compositions. The latter are then compared with thermodynamic predictions of the Thermo-Calc software used in conjunction with TCOX9 database. Finally, in selected samples, inclusions thus produced are characterized by nanoindentation, using, where applicable, the approach described in the previous chapter. Small portions of this chapter, namely details of the sample fabrication set-up and nanoindentation results corresponding to one particular sample (Si_CC), have been published as part of the two publications that correspond to Chapters 3 and 5. The rest of this chapter, including the production and indentation testing of mixed oxide inclusions, has not been submitted for publication at the time of submission of this thesis. The experiments and calculations described here, as well as write-up of this thesis chapter were chiefly conducted by the undersigned.

4.1 Introduction

As discussed in previous chapters, oxide inclusions are inevitably present in steels and are known to affect alloy properties, generally in a negative way. For certain steel alloys, intrinsic inclusion characteristics such as their strength play a critical role in the productivity of forming operations or the performance of steel products. An example of this is with steels used to produce tire cords: these are drawn to small diameters, which makes the presence of hard and brittle oxide particles particularly damaging as these can cause the cord to break while it is being processed. Another example is that of steels used to fabricate bearings and components, which are subjected to contact fatigue, the lifetime of which is often determined by the nucleation of damage at inclusions [15,17,57,89].

In alloys for which the inclusion properties are critical, the complete fabrication process needs to be controlled not only to obtain steel with the appropriate composition and microstructure but also to avoid oxide inclusions with detrimental characteristics, given that their presence in the alloy cannot be eliminated entirely. This is done by careful consideration of the chemistry of the melt, and also of the refractories and the slag that are in contact with the liquid metal, in addition to metal handling techniques, all of which can influence the characteristics of the oxide inclusion population. Given the number of variables influencing the characteristics of oxide inclusion in industrially produced alloys, the analysis of oxides observed in laboratory-produced samples is of interest since this simplifies the link between inclusion properties and conditions in which they precipitate.

In the following, deoxidation experiments leading to the precipitation, in iron, of oxide inclusions belonging to the systems Al_2O_3-SiO_2-CaO and MnO-SiO_2-FeO are described. These samples are used to study the structure and composition of resulting inclusions, and to measure their local main mechanical characteristics by means of nanoindentation.

4.2 Experimental methods

4.2.1 Production of iron samples containing oxide inclusions

Iron samples containing oxide inclusions were fabricated by the deoxidation of high-purity iron melts with the goal of generating conditions for the in-situ precipitation of small proportions of discrete oxide particles within the iron melt. A typical deoxidation experiment consisted of: i) induction melting of oxygen-containing iron to a temperature in the range 1550-1600°C, ii) dropping a pre-alloy of iron with the deoxidizing element(s) into the melt, ii) leaving time for melting of the pre-alloy and inclusion formation (times usually in the range of 30-180 s), iii) cool-down and solidification of the sample.

Initially, to guarantee that sufficient oxygen was present before deoxidation, iron lumps were melted with small amounts of Fe_2O_3 powder before adding the pre-alloys containing the deoxidizer (see Table 4.1, Section 4.3.2.1 for details). Later, it was determined that iron lumps used for the study, because they were not vacuum-remelted, contain residual amounts of oxygen. Oxygen contents in the iron lumps were thus measured by the inert gas fusion technique (LECO ON 736, LECO, St. Joseph, MI) and were found to be in the range of 200-300 ppm. Oxide inclusions in samples of this work are therefore the result of reactions between oxygen from one or both of these sources and the deoxidizer additions.

All deoxidation experiments were performed in an argon atmosphere, using gas of 99.998 % purity. To this end, before heating the sample, the air in the chamber was evacuated to a pressure of 10^{-2} mbar, the chamber was purged with argon gas four times, and then filled with argon to atmospheric pressure for the experiment. The temperature was monitored during the experiments by means of a two-colour pyrometer (Impac ISR 6 Advanced, LumaSense Technologies, Milpitas, CA).

Samples were melted using either a ceramic crucible (alumina or quartz) or a cold crucible set-up, presented in Fig. 4.1. The latter was designed and built in the laboratory to improve control over the oxide inclusion composition after the observation that, under certain circumstances, residual amounts of elements present in ceramic crucibles (particularly Al) could be found in the composition of oxide inclusions. The cold-crucible set-up consists of a copper mould intensively refrigerated with water and featuring a series of regularly spaced slits which serve to limit the amount of induction heating of the Cu. Its main advantage is that of remaining cold during the melting operation, preventing chemical interactions between the charge and the crucible. Its main drawback, however, is the formation of strong thermal gradients across the molten iron sample: the intensive cooling and the need to keep the crucible cold usually cause

regions of the sample to remain solid during the process, which thus do not participate in the deoxidation reactions. Despite the resulting sample inhomogeneity, the technique is preferred when performing deoxidation experiments in which inclusions are not to contain aluminium.
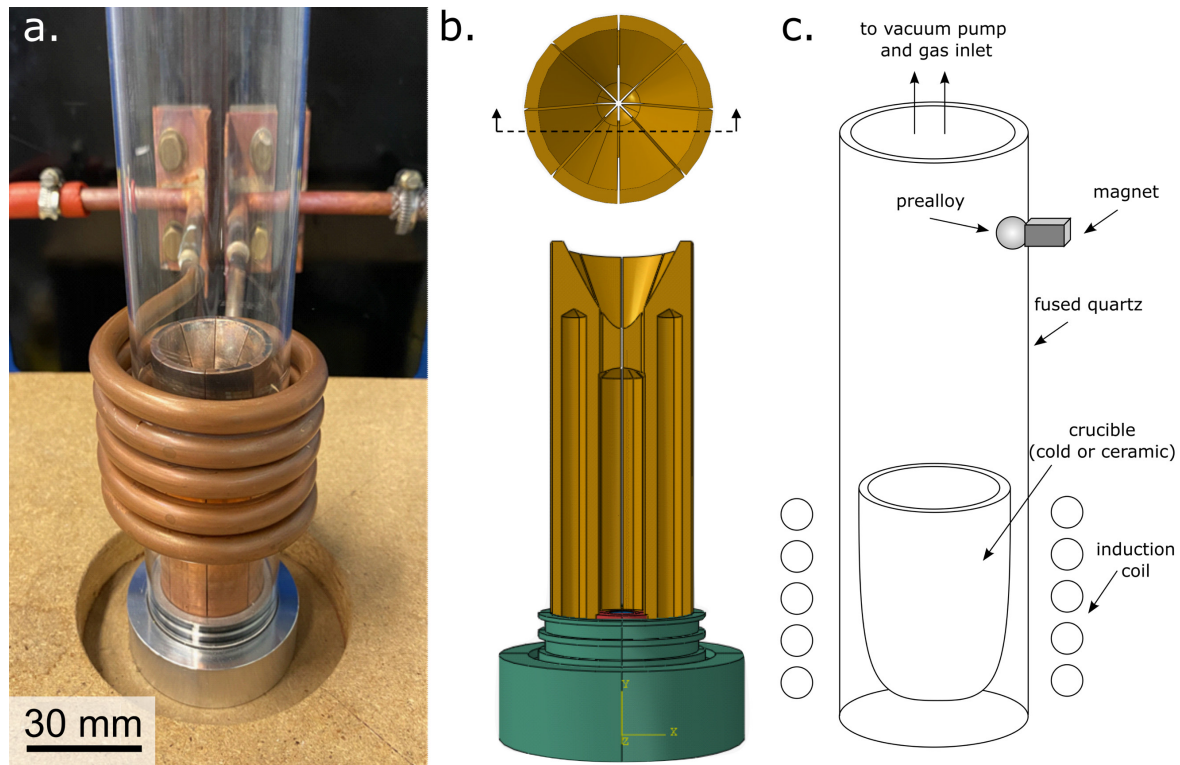

Figure 4.1 a) photography and b) schematic cross-section of the cold-crucible set up used for the production of iron samples containing oxide inclusions; c) schematic drawing depicting the strategy used in both crucible set-ups to drop iron pre-alloys for the deoxidation experiments.

Iron pre-alloys used for deoxidation were fabricated by arc-melting iron lumps with controlled quantities of the element(s) Al, Si, and/or Mn. Before being added to the melt, the pre-alloys were held at a relatively high position in the inner side of the quartz tubes by a neodymium magnet placed on the external (cold) side of the tube (Fig. 4.1 c). Once the iron was liquid, the magnet was removed, releasing the pre-alloy lump, which then fell and dissolved into the melt. The one exception to this method were the additions (in the form of Ca-silicide) used to deoxidize with calcium, as these were not pre-alloyed due to the very low solubility of Ca in iron. To add calcium, therefore, the deoxidizer was introduced with the iron lumps in the crucible from the beginning of the experiment. A special mechanism was devised to "encapsulate" the deoxidizer in the solid iron (Fig. 4.2). This was intended in part to limit the evaporation of Ca, which boils at a temperature below the melting point of iron, and also to keep the deoxidizer away from the crucible walls which were either cold, which would limit reaction, or hot and made of alumina, which is less stable than Ca oxide and would thus react with it. The Ca-silicide powder was thus first incorporated at the bottom of a threaded hole drilled in the iron lump, Fig. 4.2 a (on occasions, the iron was previously arc-melted to obtain a shape that was more appropriate for drilling a hole). The hole was then closed tightly with a small bolt produced out of the same high-purity iron material. The bolt was produced by arc-melting and casting its lower portion into a cylindrical cavity so as to create a small rod which

49

was then threaded, Fig. 4.2 b. All the iron pieces used for the encapsulation, shown in Fig. 4.2 a & b, were cleaned with acetone in an ultrasound bath after the drilling and threading operations.
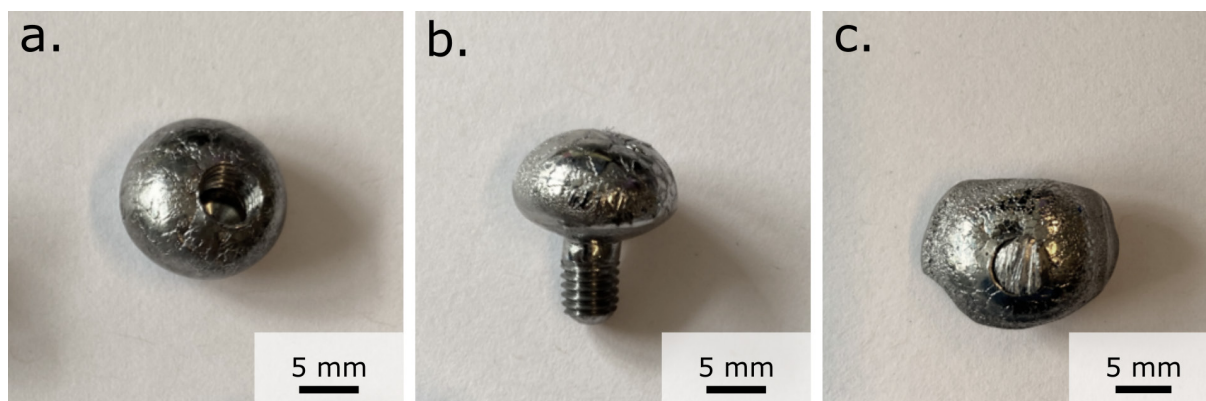

Figure 4.2 Images of the system used to "encapsulate" ca-silicide powder inside high-purity iron. a) high-purity iron lump after arc-melting (to produce a globular shape) and after drilling and threading a hole in one of its sides; b) high-purity iron piece produce by arc melting and casting, which was threaded and used to close the hole shown in a); c) metal piece after the encapsulation of the powder in which the top portion of the piece shown in b) was cut after screwing the iron bolt shown in b) into the hole shown in a).

4.2.2 Microstructural characterization

For the characterization of observed inclusions, samples were prepared using conventional metallographic techniques, including sawing, wet grinding with SiC paper, and polishing with diamond suspension down to a diamond particle size of 0.25 μm. When the size and/or geometry of the samples were not adequate for handling, the aforementioned steps were performed after hot mounting the samples in an electrically conductive epoxy resin. The inclusions were observed along polished cross-sections using optical and scanning electron microscopy (SEM). For inclusions of relatively small size (approximately less than 10 μm), the electrical conductivity of the metallic matrix was sufficient to avoid charging effects in the SEM. For relatively large inclusions (~ 10 μm or more) charging effects on the surface were sometimes observed during imaging; in those few cases, the deposition of a thin carbon coating was used to improve the chemical conductivity before SEM imaging and elemental analysis.

The chemical composition of observed inclusions was determined in the SEM by means of energy dispersive spectroscopy (EDS), using an acceleration voltage of either 8 keV or 15 keV (the latter being preferred for inclusions containing Mn). EDS spectra were collected over an elliptical area delimited inside the inclusions but in a region remote from the inclusion/iron interface (*e.g.,* see Fig. 4.3 c) or by selecting a point along the polished inclusion surface. For inclusions observed to be composed of multiple phases, EDS spectra were collected at selected separate points within each of the phases along the polished inclusion surface. For each sample that was studied, EDS spectra were collected from several inclusions (> 20 if possible), from different regions of the sample to account for variations in the composition of the oxides across the molten iron samples.

The elemental composition obtained by EDS was then used to calculate the local oxide molar fractions by computing the ratio between cations and assuming the following metal-oxygen stoichiometries: SiO_2, Al_2O_3, MnO, CaO, FeO.

No iron signal was collected from inclusions produced by Si, Al and/or Ca deoxidation of diameter (at the intersection with the sample surface) above ~ 5 μm while iron trace signals were occasionally detected by EDS on particles in this system of apparent diameter lower than this; we take this as a sign that the iron signal was present in those smaller inclusions because the e-beam/matter interaction volume extended into the iron matrix. Larger amounts of FeO were detected in inclusions deoxidized with Si-Mn. These could be a consequence of the lower deoxidizing power of the additions; however, this may also be a result of the increased interaction volume caused by the greater acceleration voltage of 15 keV (vs 8 keV).

Finally, the 3D morphology of observed inclusions was characterized after removing a layer of the iron matrix by selective chemical etching using a concentrated nitric solution (~30 % HNO_3 in ethanol) or by electropolishing (using Struers A2 electrolyte). Oxide inclusions partially exposed at the surface of the iron samples were imaged using SEM. Exposed inclusions with a composition corresponding with pure SiO_2 were also analysed for their structure using confocal Raman spectroscopy (inVia™ confocal Raman microscope, Renishaw); spectra were collected with a 532 nm laser, using a x 100 objective and a confocal set up.

4.2.3 Nanoindentation of selected inclusions

The stiffness and hardness of oxide inclusions were probed by placing indentations on inclusions observed in selected samples of this work. In order to correlate the nanoindentation response with the chemical composition of the oxides, individual inclusions were first labelled by carving a number into the neighboring matrix using FIB milling (Fig. 4.3 a) before being probed by nanoindentation and analyzed for elemental composition using EDS as described in Section 4.2.2. This strategy allows the mechanical properties and chemical composition to be unequivocally linked but renders the work more time-consuming. For this reason, this procedure was implemented only for inclusions observed in two samples, namely one containing inclusions corresponding to the Al_2O_3 - SiO_2 - CaO system (sample CaSi_S) and another to the MnO - SiO_2 - FeO system (sample SiMn2_CC). Both contained oxide inclusions which appeared to be single-phased when observed by optical and electron microscopy.

Samples for nanoindentation were fixed onto a magnetic holder using a high-temperature wax (Pelco Quickstick™ 135 Mounting Wax or similar). All nanoindentation experiments were performed using a Hysitron TI 950 apparatus (Bruker, Billerica, Massachusetts, US) using a Berkovich diamond tip and indentation loads up to 1.3 mN. The precise indentation load for each individual test was chosen as a function of the particle size in such a way that indentations depths would be approximatively ten times smaller than the distance of the indent location to the matrix/inclusion interface. Accurate positioning of the indents on the particles was possible thanks to the 500 nm XY axis resolution while positioning the indenter. The scanning capability of the instrument was used to provide an image of each tested particle before and after the tests,

which were used to determine the inclusion area along the surface of the iron sample using the *Image J* software for image analysis. Indentations were performed using a loading function with loading-holding-unloading segments of duration 5-2-5 seconds, respectively. If inclusions were big enough to accommodate more than one indentation, the results of those indentations were averaged to obtain one hardness and elastic modulus value per particle (as required by the averaging procedure detailed in the previous chapter).
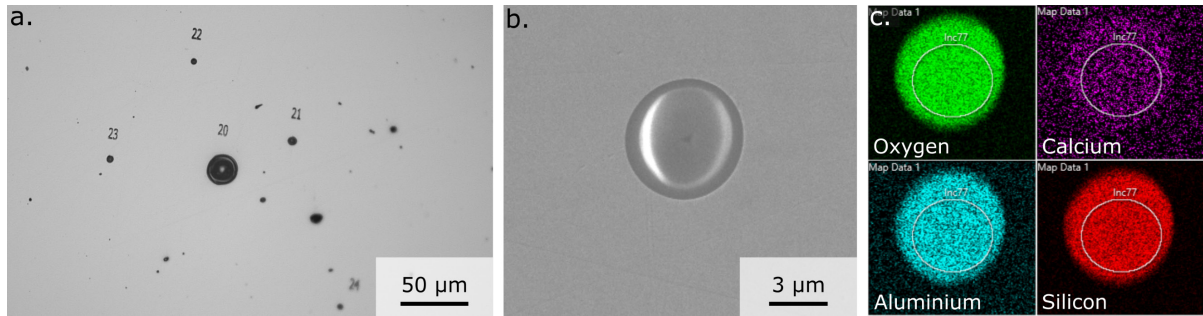

Figure 4.3 a) Optical microscopy image illustrating the labelling method used to identify individual inclusions; b) SEM image of an inclusion after nanoindentation; c) elemental mapping obtained by EDS after indentation (white circles delimit the area where EDS data were collected for determination of the inclusion composition).

The procedure described in Chapter 3 was then implemented to account for substrate elasticity contributions, using $\alpha = 1.06$ (Eq. 3.6). The matrix was assumed to have (isotropic) elastic properties corresponding to $E = 210$ GPa and $\nu = 0.3$, which in combination with a diamond tip having $E = 1140$ GPa and $\nu = 0.07$ lead to a reduced modulus for iron of 192 GPa. Iterations to compute the extra compliance and the elastic modulus were performed until the difference between the raw and corrected values for the reduced modulus fell below 2 GPa. This was, in all cases, achieved after two iterations.

4.3 Results

4.3.1 Macroscopic aspect of the samples

Except for alumina inclusions, which were observed to aggregate and adhere to ceramic crucible walls (Fig. 4.4 a), oxide particles were generally dispersed across most of the molten iron volume. In particular, samples produced using ceramic crucibles led to a homogeneous distribution of inclusions (Fig. 4.4 b), the amount of which decreased considerably if the alloy was kept liquid for relatively long times (>5 minutes). Samples produced using the cold crucible set-up led to comparatively more heterogeneous materials. The volume of the sample was, on occasions, separated into two major areas: i) one which has remained solid during the deoxidation and that had not reacted with the deoxidant; within those regions, iron oxide inclusions are usually observed, and ii) one that was liquid and where deoxidation effectively took place since inclusions compositions effectively contained the deoxidizer additions. In

those samples, oxide inclusions resulting from deoxidation reactions were found in the area associated with complete melting or at the line delimiting the two regions.
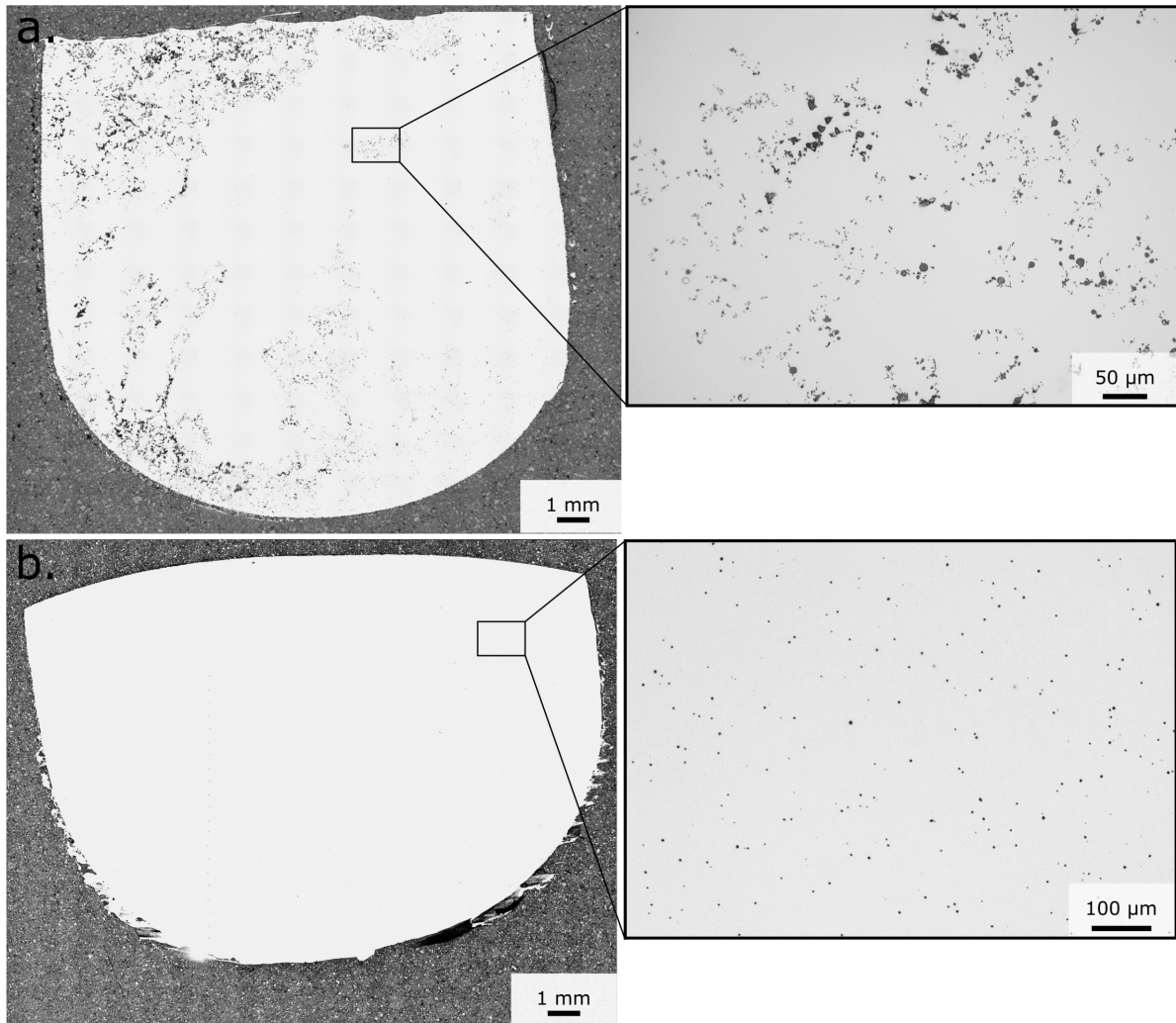

Figure 4.4 Macro and microscopic views of representative samples where inclusions were seen as a) aggregates (Sample Al_A), b) homogeneously dispersed (Sample Si_A).

4.3.2 Inclusions belonging to the system Al_2O_3-SiO_2-CaO

4.3.2.1 Characteristics of observed inclusions

Table 4.1 lists deoxidation experiments producing inclusions in the system Al_2O_3-SiO_2-CaO, for which representative inclusion morphologies and chemical composition are presented in Fig. 4.5. These include deoxidation experiments in which Si or Al alone were used to deoxidize, as well as experiments in which calcium silicide was used to produce mixed oxide inclusions.

Deoxidation experiments using Al as a deoxidizer led to pure alumina inclusions. These were observed as aggregates of either equiaxed or dendritic structures (Fig. 4.6), irrespective of the type of crucible used (alumina or cold). Silicon deoxidation experiments (with or without Ca and Al additions) led to inclusions with spherical or near-spherical morphology, Fig. 4.5 and Fig. 4.7a. In particular, inclusions produced by pure Si deoxidation carried out in the cold crucible apparatus, for which the chemical composition corresponded to pure SiO_2, were observed to have most often a spherical morphology. Alternatively, at times, a dendritic morphology (Fig. 4.7 b) was observed similar to that documented in Refs. [27,47], or, to a still smaller extent, a rosette morphology (Fig. 4.7c), analogous to that described in Ref. [187]. Although thermodynamic considerations indicate that cristobalite is the stable form of silica at the temperature at which these oxides are likely to have precipitated ($\approx 1600 \,°C$), their spherical morphology suggests that present silica inclusions are amorphous. This was confirmed by confocal Raman spectroscopy data, presented in Fig. 4.8. As seen, the inclusions give broad intensity shifts instead of narrow bands characteristic of crystalline structures; furthermore, data from the inclusions closely resemble the spectrum measured for fused quartz while differing markedly from the spectrum emitted by crystalline quartz (*e.g.,* see Fig. 1 of Ref. [188]).

While no clear correlation was determined for the relationship between the chemistry of observed inclusions and their size, it was found that when inclusions have a high SiO_2 content, as in samples Si_CC and Si_A, the particles were generally small ($< 5 \,\mu m$) and had a relatively narrow diameter distribution. Both more significant size variations and larger inclusions were observed for mixed oxide inclusions (one can, for example, compare the size of the inclusions shown in Figs. 4.5 a & c with those in Fig. 4.5 d or those in Fig. 4.11).

Table 4.1 Summary of deoxidation experiments that lead to inclusion in the system Al_2O_3-SiO_2-CaO.

Sample name	Crucible	Deoxidizing element(s)	Nominal deoxidant addition (wt. % deoxidant across the entire sample volume)	Fe_2O_3 addition (massic ppm oxygen added across the entire sample volume)	Figure 4.5
Si_A	Ceramic (Al_2O_3)	Si	0.9 wt. % Si	~2200 ppm O	a
Al_A	Ceramic (Al_2O_3)	Al	1.54 wt. % Si	~200 ppm O	b
Si_CC	Cold	Si	0.38 wt. % Si	-	c
CaSi_S	Ceramic (SiO_2)	Ca&Si	0.12 wt. % Ca-silicide	-	d
CaSiAl_CC	Cold	Ca&Si&Al	0.08 wt. % Al 0.64 wt. % Ca-silicide	-	e

In terms of inclusion composition, deoxidation experiments carried out with one single deoxidant (simple deoxidation) generally led to inclusions of uniform chemistry, provided that the amount of deoxidant was sufficient to trap all oxygen and thereby avoid mixed oxides with iron. In samples produced in the cold crucible, this led to the formation of either pure SiO_2 or pure Al_2O_3 particles. For samples deoxidized with Si but produced in an alumina crucible, inclusions contained traces of Al in the order of 3 at. % resulting from contamination by the crucible material. As mentioned before, inclusions produced by silicon deoxidation experiments carried out in the cold crucible had a composition (determined by EDS measurements) corresponding to pure SiO_2, with no trace of Al, Fe, or other metals, Fig. 4.8 b.
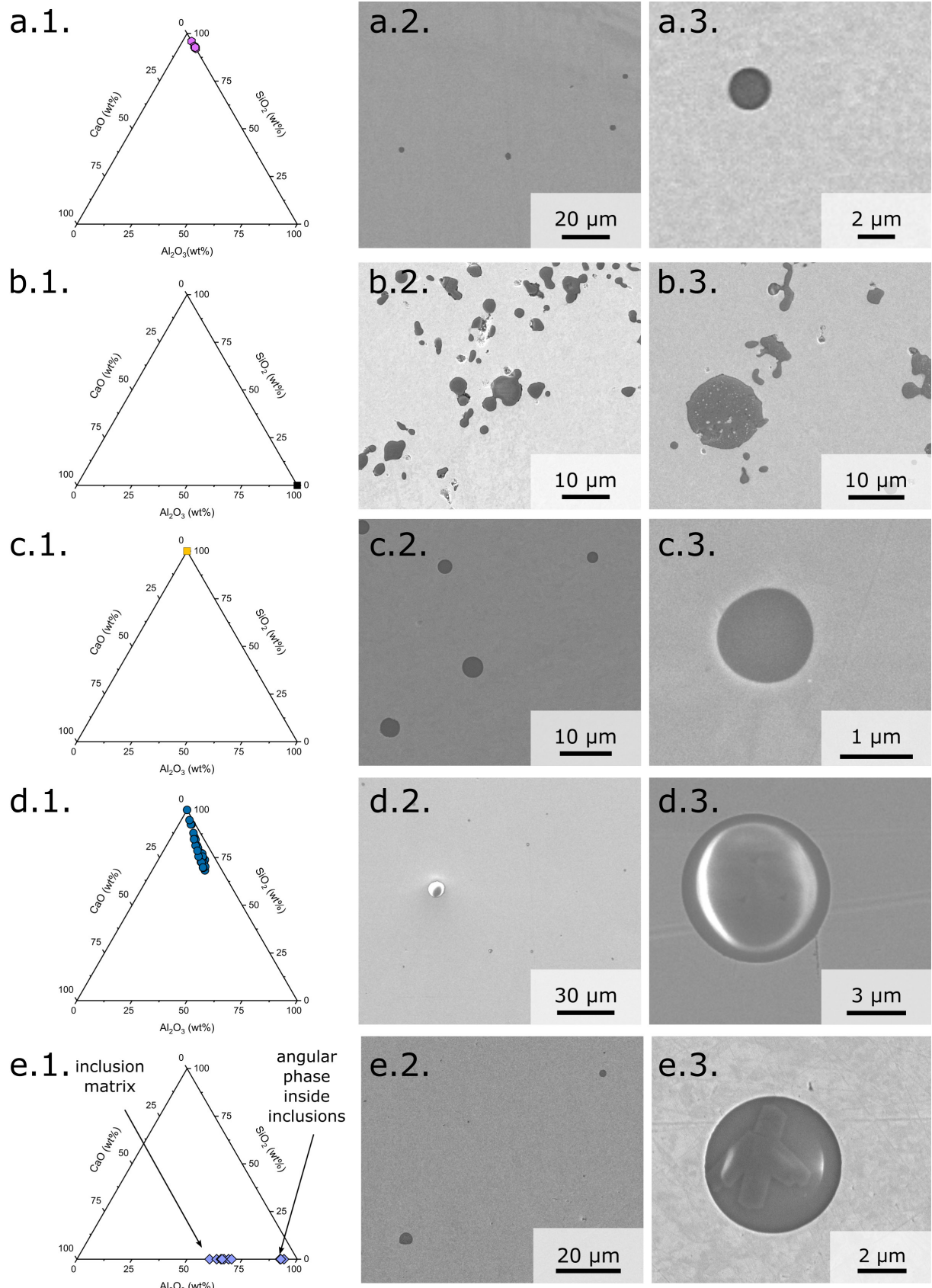
Figure 4.5 SEM images and chemical compositions of inclusions belonging to the system Al_2O_3-SiO_2-CaO. Images correspond to samples listed in Table 4.1 as follows: a) Sample Si_A; b) Sample Al_A; c) Sample Si_CC; d) Sample CaSi_S; e) Sample CaSiAl_CC.
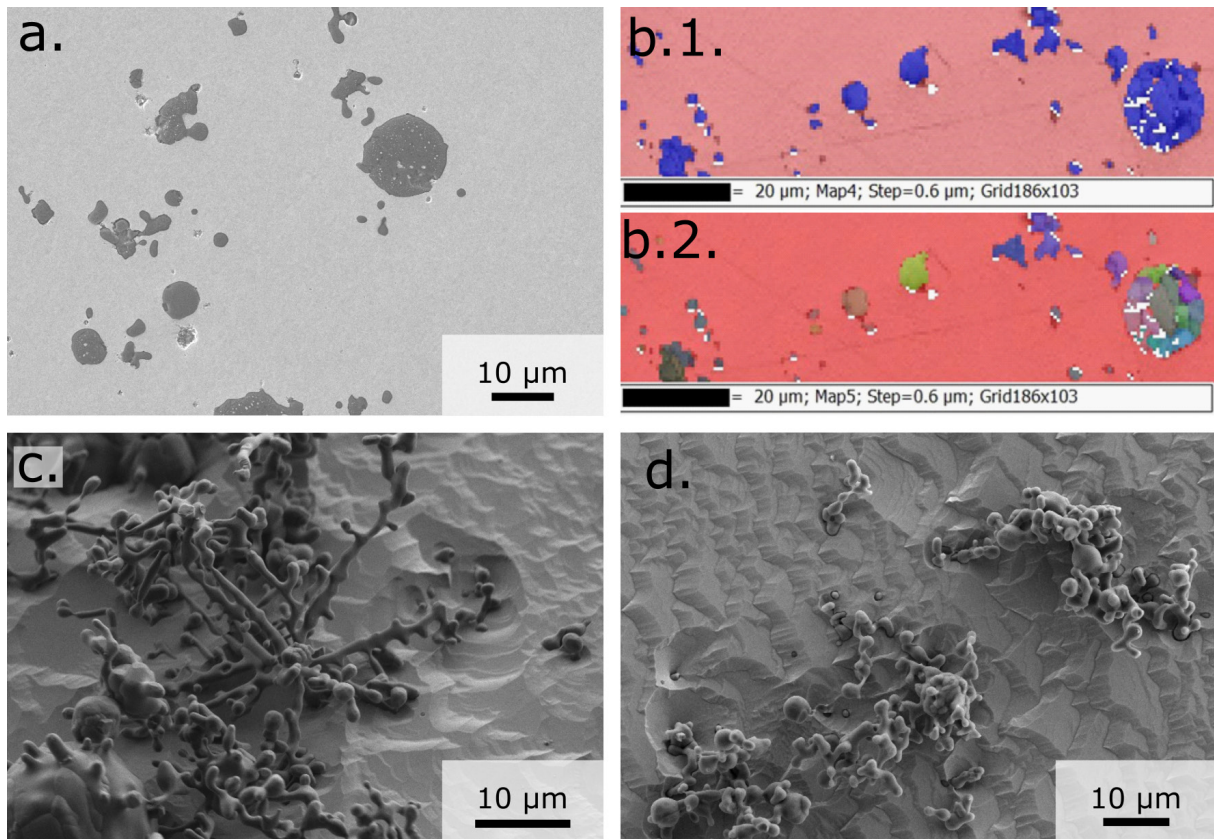
Figure 4.6 Examples of observed alumina inclusions. a) SEM image and b) EBSD signal along a polished cross-section: b.1) phase map where alumina = blue and iron = pink, b.2) orientation map in Euler mode where iron = pink and different colours are used to present different alumina crystal orientations; c) and d) SEM images after chemical dissolution of a layer of the iron matrix where c) dendritic and d) aggregated alumina structures can be observed.

Deoxidation experiments carried out with more than one deoxidant (complex deoxidation) often led to oxide inclusions with compositions that varied across the sample and, on occasion, to inclusions containing several phases. Measured inclusion chemical composition variations observed across a single sample are consigned in the ternary plots of Figs. 4.5 a, d & e. An example of multi-phase inclusions in the Al_2O_3-SiO_2-CaO system is shown in Fig. 4.5 e. An additional observation is that inclusions produced by deoxidation experiments with Ca-silicide were observed to contain considerable amounts of Al, even when not produced in alumina crucibles. The presence of Al in the Ca-silicide powder used for deoxidation was confirmed by EDS analysis, yielding around 2 wt. % of the powder composition when the overall average composition comprising multiple particles was analyzed; however, when EDS determinations were performed at random point locations, aluminium was either not detected or measured to be present in a concentration of up to 22 wt. %. This implies that the aluminium as an impurity is not homogeneously distributed in the Ca-silicide powder.
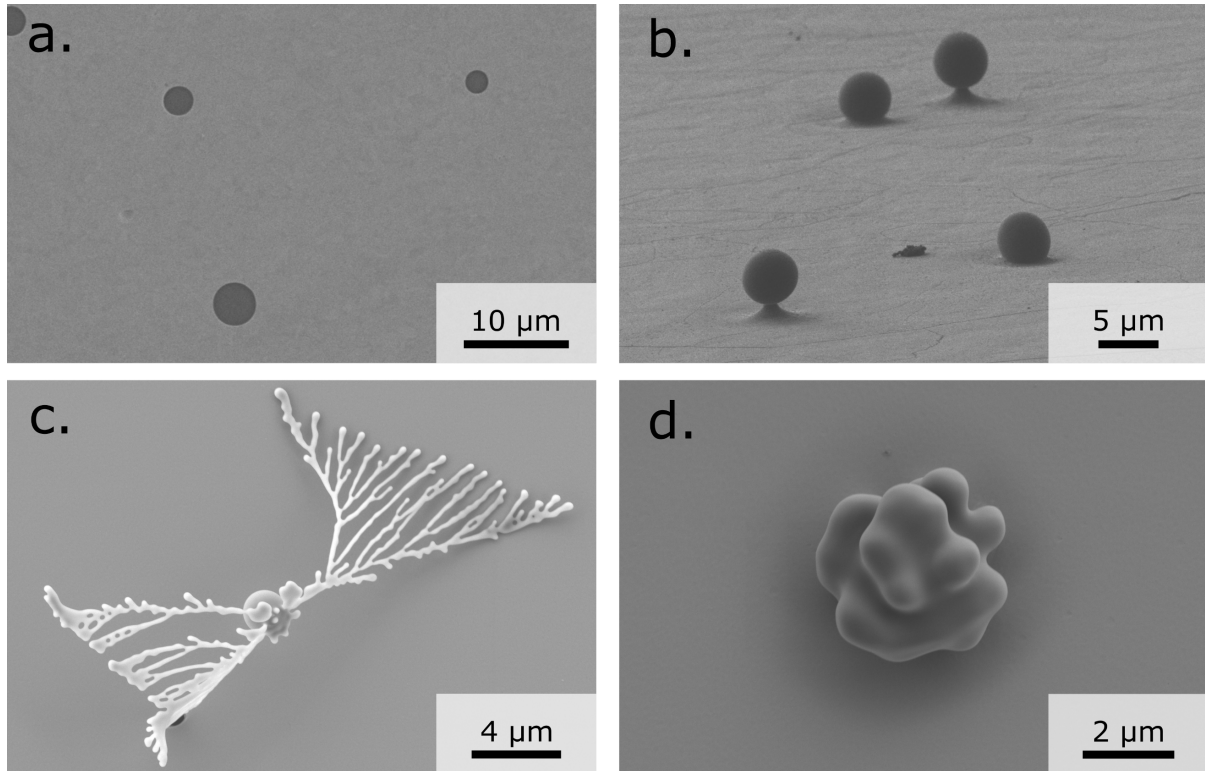
Figure 4.7 Examples of silicate inclusions observed on: a) a polished cross-section; b), c), and d) after dissolution of a layer of the iron matrix by electropolishing. Morphologies corresponding to c) and d) were only observed for high-purity silica inclusions in this work, while spherical morphologies are common to various silicate oxide inclusions
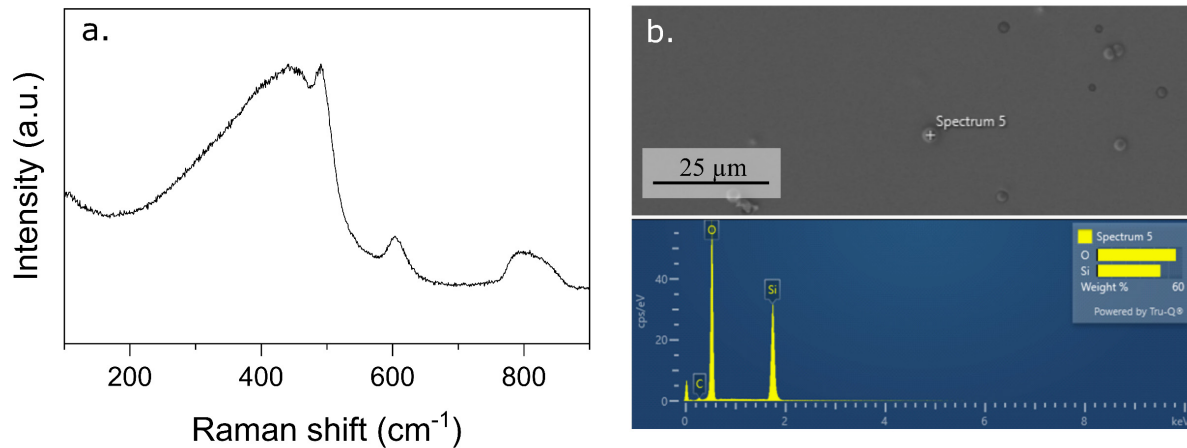

Figure 4.8 a) Raman spectrum, and b) EDS spectrum, collected from SiO_2 inclusions observed Sample Si_CC. Spectrum collected on inclusions exposed after dissolution of the iron matrix by electropolishing.

4.3.2.2 Nanoindentation results

Figure 4.9 presents the chemical composition of individual inclusions belonging to the Al_2O_3-SiO_2-CaO ternary diagram that were labelled (using FIB milling) and probed by nanoindentation. Those correspond to inclusions found in Samples CaSi_S and Si_CC. Figure 4.10 presents the obtained nanoindentation results (those obtained by probing SiO_2

inclusions in Sample Si_CC were also presented in Chapter 3). Because the compositions of inclusions in these two samples lie approximatively along a common line on the ternary diagram of Fig. 4.9, nanoindentation results for these two samples are presented in a single plot as a function of the silica content (the only component in inclusions of Sample Si_CC). In Fig. 4.10, raw values for the indentation modulus and hardness are represented using hollow symbols, while values obtained after accounting for substrate elasticity contributions are represented with colour-filled symbols (using $\alpha = 1.06$, that is, considering all particles as if they were embedded to the same depth, representative of a random particle depth distribution, see Chapter 3).

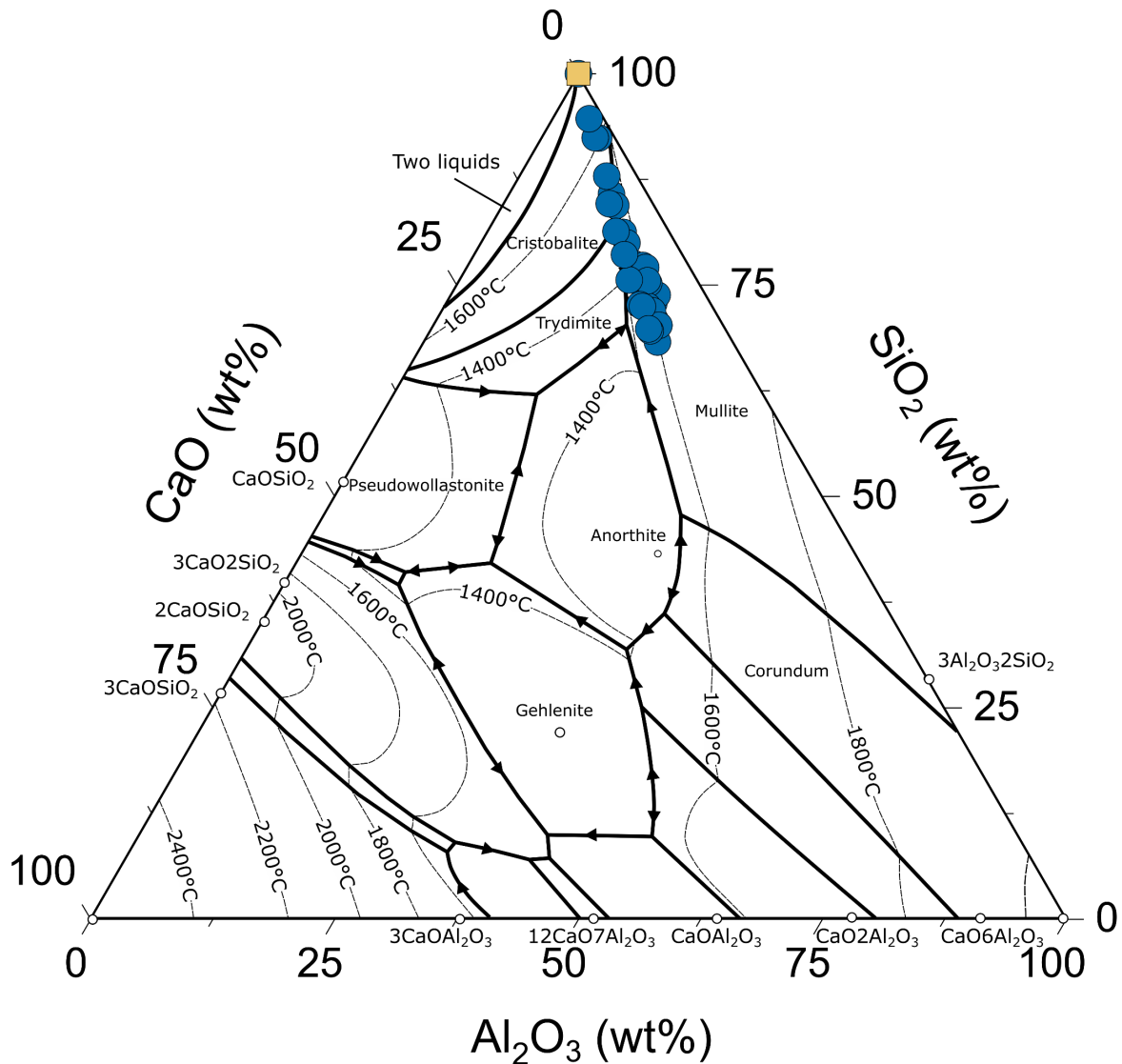**Figure 4.9** Chemical composition of inclusions obtained in the Al_2O_3-SiO_2-CaO system corresponding to Sample Si_CC (yellow squares) and Sample CaSi_C (blue circles). Each symbol corresponds to the composition determined in one single inclusion.
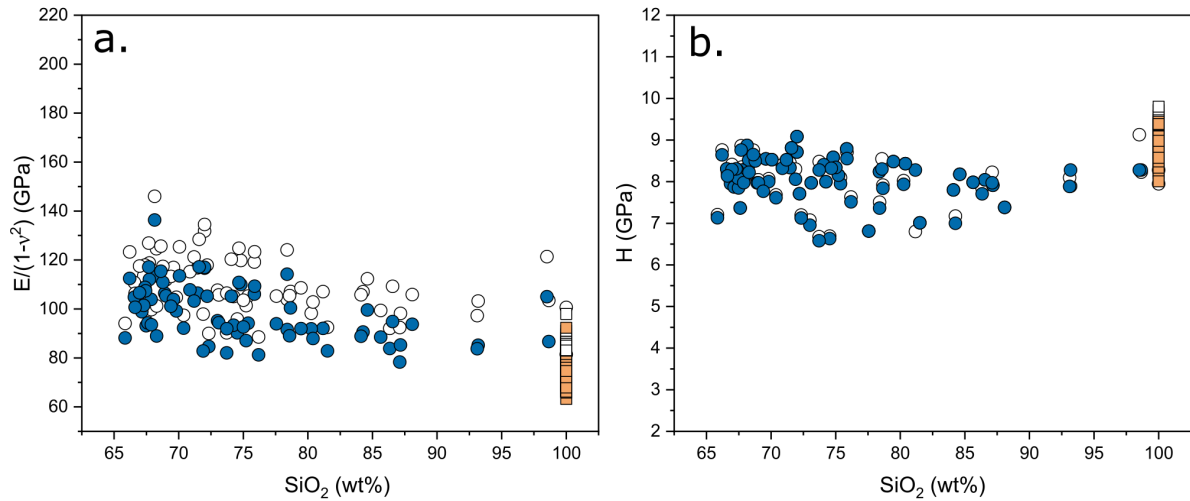
Figure 4.10 Nanoindentation results obtained by probing individual inclusions on Sample CaSi_C (circles) and Si_CC (squares, data already presented in Chapter 3). Hollow symbols correspond to raw data; colour-filled symbols correspond to values after accounting for substrate elasticity contributions using the method described in Chapter 3 and α=1.06. Each point corresponds to indentation properties determined on one single inclusion.

4.3.3 Inclusions belonging to the system MnO-SiO$_2$-FeO

4.3.3.1 Characteristics of observed inclusions

Table 4.2 presents the details of deoxidation experiments that led to inclusions in the system MnO-SiO$_2$-FeO, namely deoxidation experiments in which Si and Mn additions were used to deoxidize iron melts. Representative inclusions found in those samples are presented in Figure 4.11.

Table 4.2 Summary of deoxidation experiments that lead to inclusion in the system MnO-SiO$_2$-FeO.

Sample name	Crucible	Deoxidizing element(s)	Nominal deoxidant addition (wt. % deoxidant across the entire sample volume)	Fe$_2$O$_3$ addition (massic ppm oxygen added across the entire sample volume)	Figure 4.11
SiMn_CC	Cold	Si Mn	0.3 wt. % Si 1.2 wt. % Mn	-	a-c
SiMn2_CC	Cold	Si Mn	0.6 wt. % Si 4.5 wt. % Mn	-	d-f

As can be observed on Fig. 4.11, inclusions belonging to the MnO-SiO$_2$-FeO system were usually found to be spherical and to have a relatively wide range of diameters. Two phases are clearly observed in inclusions corresponding to Sample SiMn_CC (Fig. 4.11 a, b & c). The dark phase inside these oxide inclusions has a composition that corresponds to high-purity silica (no Mn or Fe traces are observed when probing the elemental composition of these second phases). The chemical composition of the matrix in those two-phase inclusions and that of (generally smaller) single-phase inclusions is close to that expected for MnOSiO$_2$.

Inclusions in Sample SiMn2_CC appeared to be single-phased when observed by optical or electron microscopy, Fig. 4.11 d & e. Higher magnification imaging under the SEM, however, reveals that some of these oxide particles are in fact multi-phased, as shown in Fig. 4.11 f. Because of the small size of the second phases, chemical identification using EDS could not be performed with accuracy.
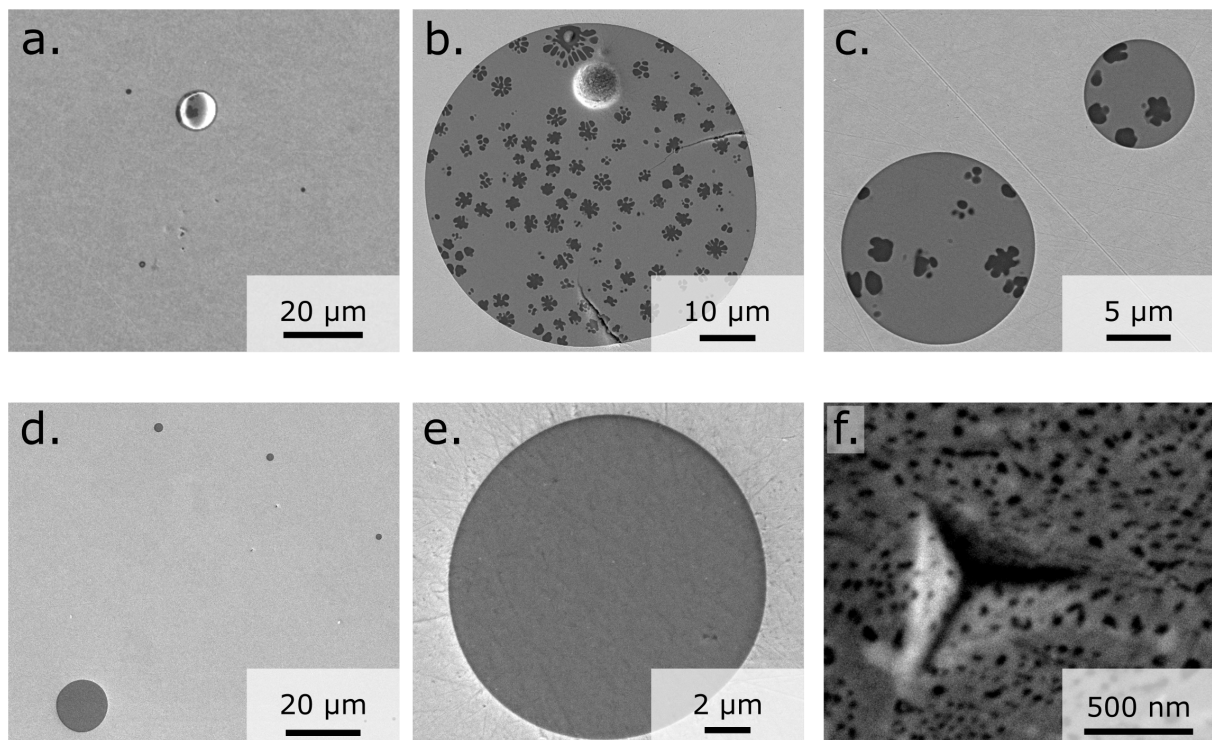

Figure 4.11 SEM images and chemical compositions of inclusions belonging to the system MnO-SiO$_2$-FeO. Images correspond to samples listed in Table 4.2 as follows: a, b, & c) Sample SiMn_CC, d, e & f) Sample SiMn2_CC.
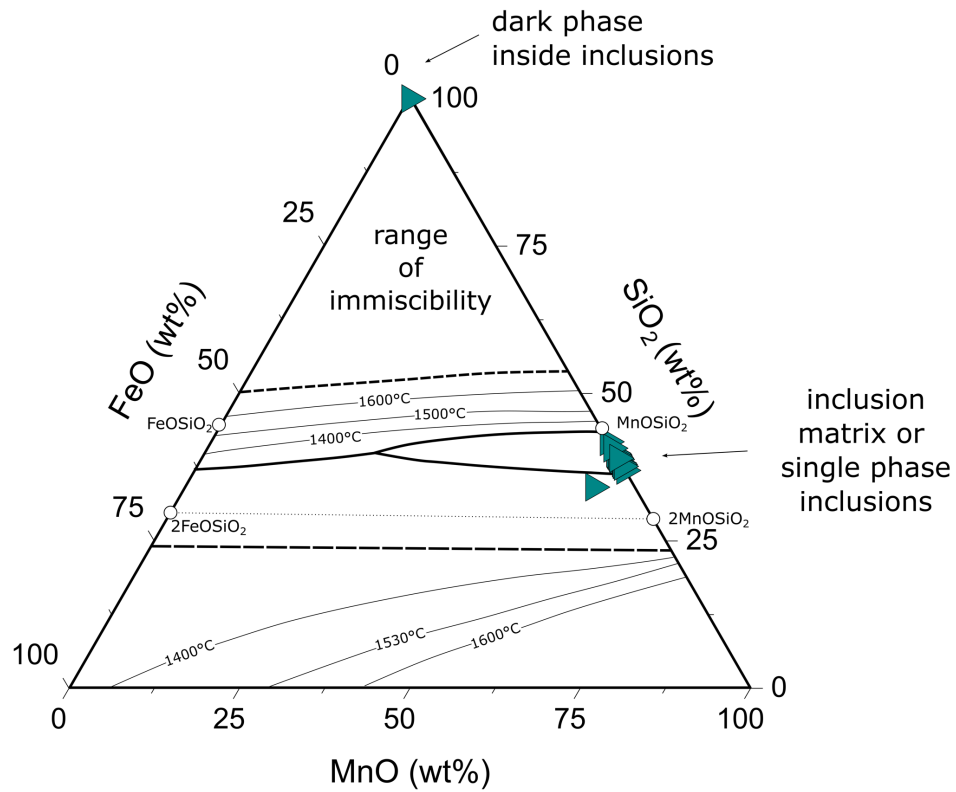
Figure 4.12 Chemical composition of inclusions or inclusion phases observed in sample SiMn_CC (see Fig.4.11 b & c for inclusion phases).
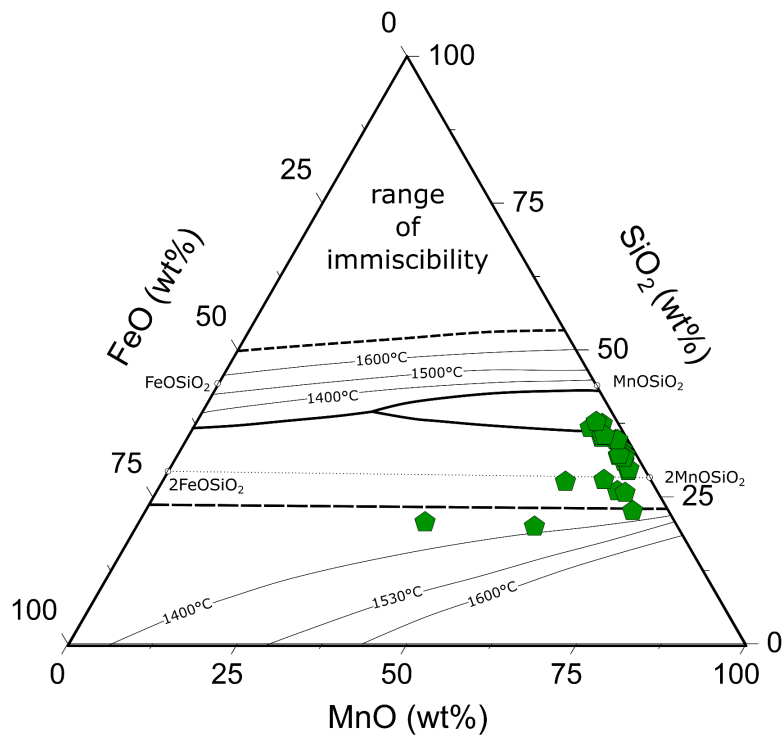

Figure 4.13 Chemical composition of inclusions obtained in sample SiMn2_CC. Each symbol corresponds to the composition determined on a single inclusion.

4.3.3.2 Nanoindentation results

Results of indentations performed on inclusions in Sample SiMn2_CC are presented in Figs. 4.14, where hollow symbols correspond to raw indentation data and colour-filled symbols correspond to values after accounting for substrate elasticity contributions using the method described in Chapter 3 and using $\alpha=1.06$. Furthermore, in Figs. 4.15 and 4.16, E and H values are presented as a function of the chemical composition of the inclusion.
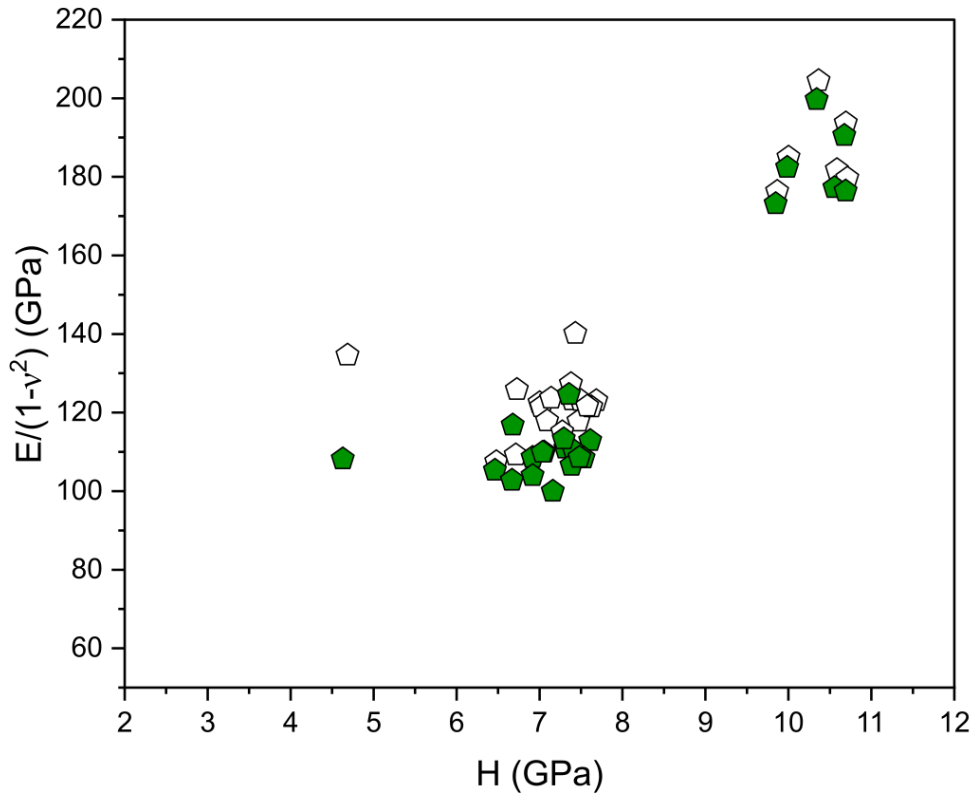

Figure 4.14 Nanoindentation results obtained by probing individual inclusions on Sample SiMn2_CC; hollow symbols correspond to raw data; colour-filled symbols correspond to values after accounting for substrate elasticity contributions using the method described in Chapter 3 and using $\alpha=1.06$. Each point corresponds to one inclusion.

Figure 4.15 Raw indentation modulus results (without correction for matrix effects) presented as a function of the inclusion composition for Sample SiMn2_CC. The dotted line delimits the approximate MnO content for which a transition in indentation properties is observed (see Fig. 4.14).
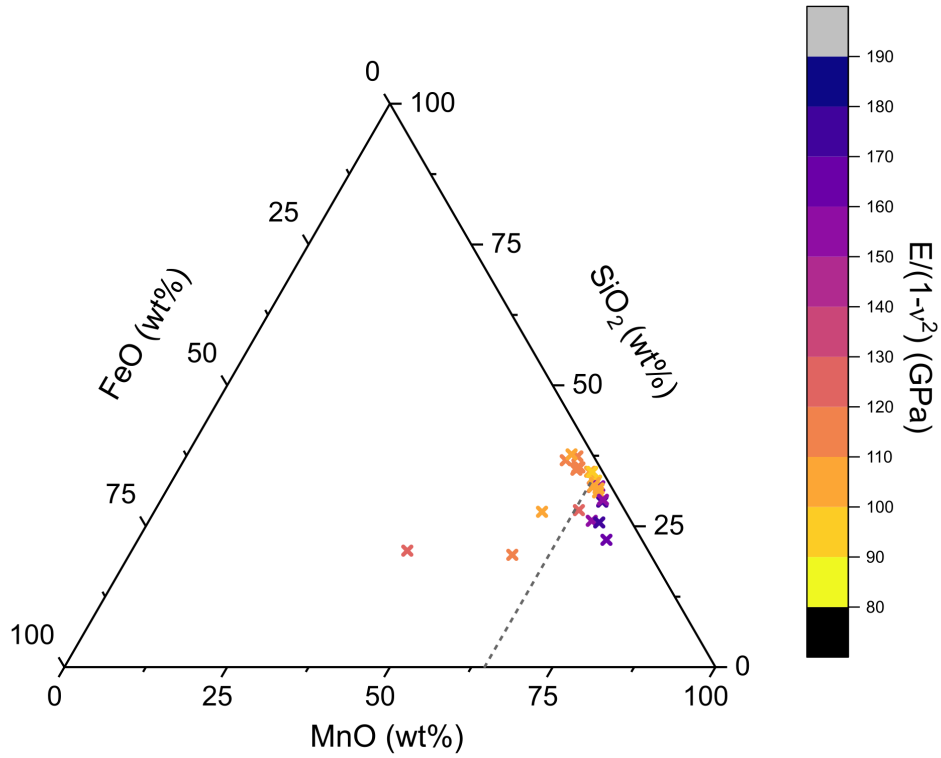

Figure 4.16 Raw indentation hardness results (without correction for matrix effects) presented as a function of the inclusion composition for Sample SiMn2_CC. The dotted line delimits the approximate MnO content for which a transition in indentation properties is observed (see Fig. 4.14).
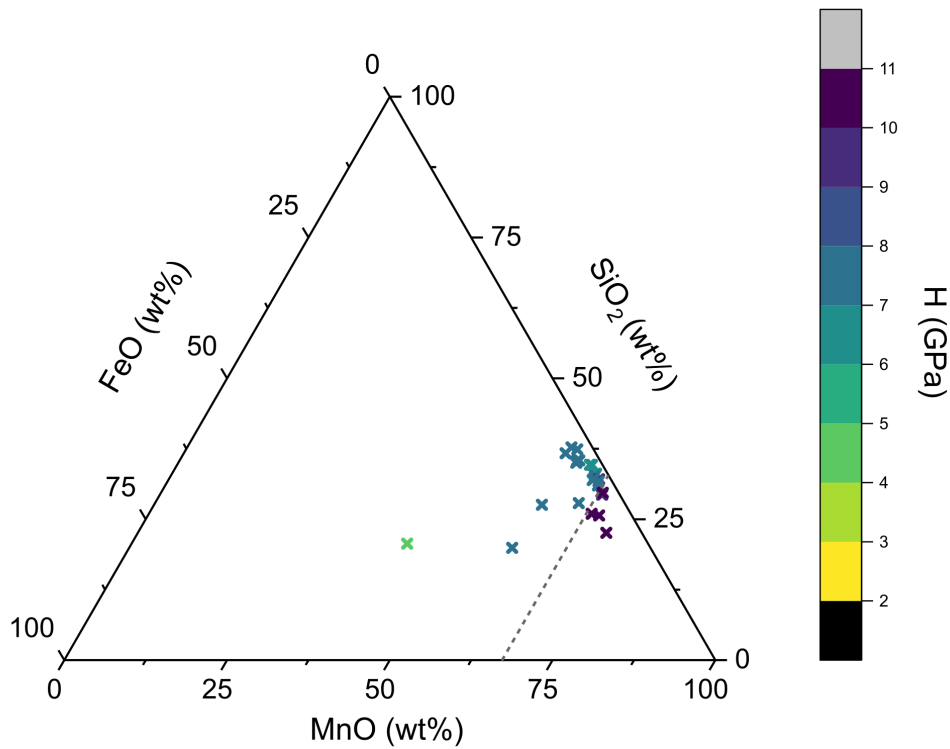
4.4 Discussion

4.4.1 Inclusions belonging to the Al_2O_3-SiO_2-CaO system

4.4.1.1 Characteristics of observed inclusions

The tendency observed in this work of alumina inclusions to form aggregates is consistent with the reported behaviour of this type of inclusions [42,48,51,66]. Observed morphologies, however, are limited to aggregates of roughly equiaxed particles or dendritic structures. Plate-like or highly faceted alumina inclusions, reported in the literature [26,42,43], have not been observed in samples of this work; their formation may therefore be attributed to steps in material processing or to elements that were absent in present laboratory experiments.

Pure alumina inclusions are crystalline and present a more irregular interface with the matrix than do other inclusions, as observed in Figs. 4.5 b and 4.6. For all other oxide inclusions, the fact that observed morphologies are usually globular suggests that the oxide was liquid at the time of precipitation. This is consistent with the chemical composition of inclusions in Sample CaSi_S (Fig. 4.5 d.1) and with the composition of the matrix making the inclusions in Sample CaSi_CC (Fig. 4.5 e.1), both lying in a region of the ternary diagram very close to the line delimiting the 1600°C liquidus projection, a temperature that was reached during the melting of the samples. For inclusions observed in Sample CaSi_CC (Fig. 4.5 e.1), the matrix is likely amorphous, while the angular phase observed in the interior of the inclusions is very likely crystalline since it is facetted. We also note in passing that the high difference in composition between the two phases (with chemistries that are close to $CaO \cdot 6Al_2O_3$ for the angular phase and $CaO \cdot Al_2O_3$ for the matrix) is not expected, given the proximity of at least one other oxide phase nearer the average composition of the inclusion along the CaO-Al_2O_3 line; see Fig. 4.9. Structures of inclusions precipitated in the present samples are mostly metastable.

For high-silica inclusions observed in Samples Si_A, Si_CC, and some of the particles observed in Sample CaSi_S (Figs. 4.5 a.1, c.1, and d.1, respectively), the liquidus temperature is above 1600°C. In those cases, inclusions could have reached melting temperatures if the heat generated during the exothermic oxide formation led to an increase in the inclusion temperature that is high enough to locally and briefly melt the oxide particle. Given that in liquid iron the diffusivity of atoms is far lower than that of heat, this scenario is unlikely: heat will be dissipated at a rate far higher than the rate of atom migration required to form the inclusion. The spherical morphology of these particles is therefore likely a result of the fact that the oxide grew within the melt from the onset as a solid glass.

References in the literature to amorphous silica inclusions nucleated and grown within iron or its alloys are scarce. Early suggestions of the precipitation of glassy SiO_2 in iron can be found in the work of Forward [187] and Flemings [14]. A more recent mention to the amorphous structure of SiO_2 inclusions in iron and its alloys can be found in a review by Zhang [189]. Gleining et al. [190] have argued that phases with the SiO_2 composition found in multiphase inclusions within 18CrNiMo7-6 case hardening steel were probably amorphous, since no

diffraction lines from those phases were observed in Electron Back Scattered Diffraction (EBSD) experiments. Looking beyond steel, Wasai and Mukai [191] showed that amorphous silica can precipitate in silicon deoxidation experiments conducted with molten copper. The present data thus provide new, explicit, confirmation of the fact that amorphous SiO_2 forms within pure, oxygen-containing, iron in the presence of dissolved silicon. As a consequence, we believe that it would be relevant to adapt thermodynamic calculations involving SiO_2 formation in iron and its alloys to consider the amorphous form of silica as a possible deoxidation product, in addition to cristobalite. This can be important because, even if the structure of the Si-deoxidation product has a small impact on the total Gibbs free energy of the system, it could potentially have a large impact on the composition of the predicted phases since crystalline forms of SiO_2 have a limited solubility for other elements while the amorphous structure can incorporate relatively large amounts of other metals/metal oxides [192].

The observed variations in inclusions composition across a single melt provide evidence that thermodynamic equilibrium was not attained across the sample. This is consistent with the lack of equilibrium usually observed in (much larger) industrial castings (see *e.g.* [16,24]). While equilibration reactions between the inclusions and the melt are known to be relatively rapid, it has been proposed that lower reaction rates are observed in the equilibration of inclusion compositions with that of the slag or the refractories [13], *i.e.* between oxide phases that are not in direct contact but for which the liquid iron acts as a transfer medium. This lack of global thermodynamic equilibration could be a result of diffusion or interface kinetic limitations. An estimation of distances that the deoxidizer species can travel while the metal is liquid can be obtained by computing $\sqrt{4Dt}$ with D a typical diffusion coefficient for Si, Al, O, Ca and/or Mn, and with t an estimation of the melting time. Precise values for the diffusion coefficients are dependent on the temperature and the species considered, but the interdiffusion coefficient for ferrous liquid alloys can be expected to be in the range of 1×10^{-5} and 2×10^{-4} cm^2/s [193]. Since melting times in experiments of this work were in the range of 30 to 180 s, one obtains diffusion distances in the range of 0.3 to 4 mm. These are lower than the sample dimensions, making inclusion compositional variations across the samples plausible, yet large compared to the observed inclusion spacing (Figs. 4.5 and 4.11), suggesting that interface kinetics are likely also limiting the rate at which the inclusion composition can change.

Because global equilibrium is generally not reached in deoxidation experiments, thermodynamic calculations cannot directly predict oxide inclusions compositions based on the nominal composition of the melt. In the literature related to oxide inclusion formation in liquid iron, different kinetic models have been proposed to account for variations in inclusion composition [13,40]; however, these generally focus on the effect of slag or refractories on an "average" inclusion composition and require the experimental determination of parameters used to characterize the speed at which reactions take place such as mass transfer coefficients, which depend on experimental conditions and on the composition of the system.

Another difficulty related to thermodynamic predictions of inclusions compositions is related to the fact that strong deoxidizers such as Ca and Al have such a strong affinity for oxygen that contents in the ppm range, which are usually difficult to determine experimentally, can have a remarkable effect on the inclusion chemistry. In the case of calcium, moreover, because of its

low boiling temperature, part of the element is evaporated during processing such that the efficiency of Ca-additions is usually very low, making precise values of resulting Ca concentrations in the melt difficult to predict. In the case of aluminium (and also for other highly reactive elements such as Mg), traces of the element can result from the contact with refractories, a fact that is confirmed here with the observed contamination from alumina crucibles. In industrial castings, sources of contamination are broader and could also include slags and trace elements from scrap.

In spite of the above-mentioned difficulties, thermodynamic prediction software and databases remain useful tools and can be used to improve the understanding of the factors controlling the composition of oxide inclusions. Thermodynamic calculations were made considering the nominal composition of Sample CaSi_S, for which predicted and observed inclusion compositions are presented in Fig. 4.17. For the calculation, the nominal Si content was considered (~ 0.7 wt. %) along with different amounts of Ca, which were calculated as a percentage of nominal additions. The oxygen content used for the calculations was 200 ppm, this being the value measured by the inert gas fusion technique in the pure iron lumps used for this study. The presence of aluminium was also contemplated since this element was present as an impurity in the calcium silicide used as a deoxidant. The calculations were performed using the commercial Thermo-Calc software in conjunction with the TCOX9 database and suspending from the database all crystalline phases associated with silica given: i) the spherical shape of present inclusions, ii) the observation that pure silica inclusions observed in iron samples of this work are amorphous, and iii) that amorphous phases have been reported for a wide area of the ternary Al_2O_3-SiO_2-CaO oxides [192]. The phases suspended from the database thus are: CRISTOBALITE, TRIDYMITE, QUARTZ, and MULLITE. The simulations were run for a temperature of 1600 °C and a pressure of 10^5 Pa.

Results are presented in Fig. 4.17. In Fig. 4.17 a, the black symbol shows the predicted inclusion composition (pure CaO) in Sample CaSi_S obtained by assuming that the entire deoxidizer addition (of calcium silicide plus the measured average aluminium content, namely 2 wt. % of the calcium silicide) is incorporated. If one assumes that only a certain percentage of the calcium remains after evaporation (while other elements remain), one obtains the other points in that figure. As seen, with 1 % of the calcium retained, one falls along the line of measured compositions.

To explain why measured inclusion compositions deviate from that prediction and lie along a line, it was then assumed that observed variations in the inclusion chemistry were caused by variations in the local concentration of deoxidizer resulting from heterogeneous mixing. This could be expected if the precipitation of oxide inclusions is sufficiently rapid such that it takes place before melt homogenization, particularly for the case of deoxidant additions in concentrated form (*i.e.*, not pre-alloyed, as was the case for this sample). As seen in Fig. 4.17 b, if one assumes that only 1 % of the Ca in the calcium silicide is incorporated but varies the concentration of deoxidizing elements while keeping the Ca/Si and Al/Si ratios constant, one obtains a series of inclusion concentrations that lie neatly along the line delineating measured inclusion compositions. It is then plausible that oxide inclusions in this sample were initially

precipitated with different compositions because of gradients in the concentration, within liquid iron, of deoxidizer agents.
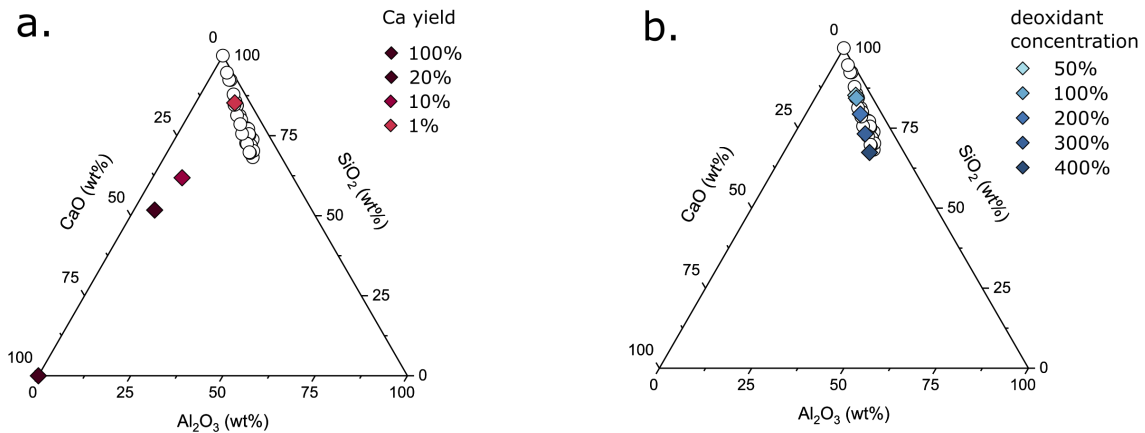

Figure 4.17 Oxide inclusion compositions observed experimentally (hollow circles) and thermodynamic predictions obtained via Thermo-Calc (coloured diamonds). a) Inclusion compositions predicted by considering the nominal deoxidizer addition (0.07 wt. % Si, 0.05 wt. % Ca), 200 ppm of oxygen, and 5 ppm total Al content (2 % of the deoxidizer added) in addition to variations in the Ca-yield (Ca contents corresponding to 0.05, 0.01, 0.005 and 0.0005 wt. %); b) Inclusion composition predictions obtained by considering that only 1 % of the Ca in the Ca-silicide is incorporated and varying the concentration of deoxidizing elements while keeping the Ca/Si and Al/Si ratios constant.

4.4.1.2 Nanoindentation results

Results of indentations performed on oxide inclusions presented in Fig 4.10 show a high level of scatter both before and after accounting for matrix elasticity contribution. As discussed in Chapter 3, this is expected of results obtained by probing embedded particles and, after correction of raw data for the (average) influence of elastic heterogeneity, is caused by variations in the particle relative depth which affect matrix elasticity contributions. As shown in Chapter 3, if the same correction is applied to all indentation points using the parameters that correspond to the average particle depth resulting from a random distribution, a reasonably accurate measurement of the mechanical properties of embedded particles can be obtained by averaging the values obtained by probing a sufficiently large number of particles. This requires, however, that averaging is performed over data that are measured on particles composed of the same material. Indentation values corresponding to inclusions in sample Si_CC (yellow squares in Fig. 4.10) are thus all averaged together since they correspond to the same chemical composition (SiO_2). In contrast, because the composition of inclusions in sample CaSi_S (blue circles in Fig. 4.10) changes gradually, data points were first binned according to the silica content and then averaged within each bin, leading to one averaged value obtained every 5 wt. % SiO_2.
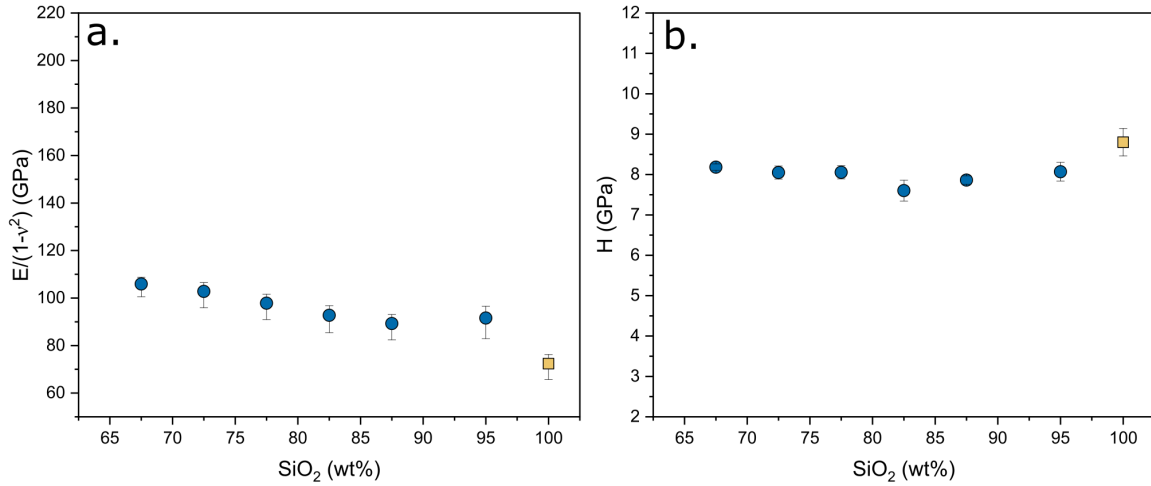
Figure 4.18 Nanoindentation results for inclusions corresponding to samples, CaSi_S (blue circles) and Si_CC (yellow squares) after correcting for matrix elasticity contributions and after averaging values corresponding to oxide particles with composition falling within 5 wt. % SiO$_2$ intervals.

Results after this binning and averaging procedure are presented in Fig. 4.18. Vertical error bars for the elastic modulus were computed by considering the uncertainty associated with the averaging procedure (since these were generally larger than the standard deviation). These were calculated by considering two extreme possibilities for the average relative particle depth of 10 % and 90 % of the particle diameter, corresponding to values of α (Eq. 3.6) of 2 and 0.6, respectively (vs. α = 1.06 used for an average particle depth of 50 %). For hardness values, since matrix elasticity effects are less pronounced, larger error bars are obtained by considering the standard deviation of the averaged datapoints, and therefore the latter were used in computing error bars of average corrected hardness values.

Given that pure silica inclusions have been confirmed to have an amorphous structure and that the results reported by Shelby [192] show that amorphous structures can be expected for a wide range of calcium aluminosilicate materials, inclusions in Sample CaSi_S can be expected to all have an amorphous structure. The gradual change in elastic properties and its relatively good correlation with similar properties measured on pure silica inclusions seem to point to the same conclusion. Assuming that those inclusions are indeed amorphous, the replacement of Si cations in the network for di- or trivalent oxides is expected to lead to an increase in the glass stiffness [101], as observed here. Elastic properties measured in this work are also in good agreement with those reported for aluminosilicate glasses in [104]. The evolution of the stiffness of inclusions of this work within the Al$_2$O$_3$-SiO$_2$-CaO oxide system is thus consistent with the literature and shows a finite, yet small, influence of composition along the line of compositions delineated in Fig. 4.9. Hardness values, however, are larger than those reported in [104]. This might be a consequence of the higher Al$_2$O$_3$/CaO ratio (in at. %) of inclusions in this work (in the range of 1.2 to 2) as compared to data in Ref. [104] (1 and below). The difference is reasonable since, in silicoaluminate glasses, a higher Al$_2$O$_3$/CaO ratio is expected to increase the coordination level of aluminium species [104] and a higher network connectivity is expected to produce an increase in hardness.

4.4.2 Inclusions belonging to the MnO-SiO$_2$-FeO system

4.4.2.1 Characteristics of observed inclusions

The spherical morphology of inclusions observed in Samples SiMn_CC and SiMn2_CC is in good agreement with the fact that, in both samples, the average inclusion composition and (in multiphase inclusions) that of the inclusion matrix lie in a region of the ternary diagram corresponding to a liquid oxide at 1600°C. In addition, the two phases observed in inclusions of Sample SiMn_CC (Fig 4.11 a-c) are in relatively good agreement with the microstructure predicted by the ternary diagram, namely a (Mn,Fe)O·SiO$_2$ matrix containing SiO$_2$ precipitates. Similar structures made of a high silica phase within a manganese silicate matrix can be found on page 47 of Ref. [84].

Although the size of the SiO$_2$ precipitates observed in inclusions of Fig. 4.11 b & c would probably allow the properties of the phase to be probed by nanoindentation, the surface-scanning technique used in this work to place indentations is only able to resolve the metal-oxide interfaces by sensing differences on the surface topography caused by the polishing and differences in the hardness of the iron and the oxide particles. This means that interfaces between different phases inside the oxide inclusions are only discernible if they come with important differences in the hardness of each phase. To work around this difficulty, Sample SiMn2_CC, for which a higher ratio of Mn to Si was used in the deoxidizer, was produced to avoid the precipitation of silica-rich phases. The observed oxide inclusion appeared, in optical and scanning electron microscopy, to be single-phased and to be suitable for nanoindentation testing (Fig. 4.11 d & e). Higher magnification images taken after the indentation testing, however, revealed the presence of two or three different phases at a very fine scale in inclusions of that sample as well (light grey areas can be distinguished in regions of the matrix in addition to the small dark phases in Fig. 4.11 f). As mentioned before, chemical identification of the phases using EDS was not possible because of the small size of the second phases.

4.4.2.2 Nanoindentation results

In spite of the relatively narrow range of measured inclusion compositions, results from indentations in Sample SiMn2_CC are clustered (Fig. 4.14), evidencing the presence of at least two groups of particles: ones with elevated hardness and stiffness and ones with comparatively lower values for both properties. As can be noted in Figs. 4.15 and 4.16, the change in inclusion properties seems to correlate with the MnO content in the oxides with the transition being observed at a MnO content of ~66 wt. %.

If the MnO-SiO$_2$ binary is considered, oxides with a global MnO content immediately higher or lower than ~70 wt. % are expected to transition from a microstructure consisting of MnO + 2MnO·SiO$_2$ to one composed of 2MnO·SiO$_2$ + MnO·SiO$_2$. Hardness values for 2MnO·SiO$_2$ and MnO·SiO$_2$ phases have been reported to be in the order of ~9.3 GPa (microhardness of 950kp/mm^2) and ~7.4 GPa (microhardness of 750 kp/mm^2) respectively [84]. These seem to correlate well with obtained results for inclusions with high and low MnO content in this study. However, if the presence of the 2(Mn,Fe)O·SiO$_2$ phase was the main factor affecting the indentation properties of the different oxide inclusions, then the line delimiting the two groups

of oxide particles should run horizontally (see Fig. 4.13) and not parallel to the MnO content, since $2MnO \cdot SiO_2$ and $2FeO \cdot SiO_2$ are mutually soluble. The reason why higher manganese contents produce harder and stiffer inclusions in this system is, thus, not only related to the crystal structure: seemingly, the composition matters as well. Explaining why this behaviour is observed will likely require a more in-depth study of the inclusion structure than is presented here, using transmission electron microscopy to determine, in particular, the exact structure of the involved phases.

4.5 Conclusions

Laboratory-scale deoxidation experiments in this work illustrate the challenges that come with the production of iron alloys if the characteristics of oxide inclusions are to be controlled. As observed here, even with considerable simplifications of the alloy system, and in laboratory experiments, with control of both crucible materials and melting conditions, oxide inclusions observed in a single centimetre-wide casting usually do not have a unique chemical composition.

Silica inclusions obtained by deoxidation of high-purity iron melts are shown to be amorphous. Across compositions explored here, oxide inclusions have been observed to have different morphologies, but are often spherical, particularly if their composition is such that they are liquid at iron melting temperatures. Their inner structures can be made of one single phase, or comprise multiple phases. In addition, those phases often do not correspond to phases predicted by thermodynamic equilibrium and can, even when thermodynamic equilibrium is obeyed, vary significantly as a result of small variations in deoxidizer concentration within the melt

Variations in the chemical composition of oxide inclusions can lead to drastic changes in the hardness and elastic properties in inclusions of the system $MnO\text{-}SiO_2\text{-}FeO$, while for inclusions in the $Al_2O_3\text{-}SiO_2\text{-}CaO$ system observed variations in hardness and elastic properties were smaller and more gradual.

Finally, it is shown that hard inclusions with elastic properties close to those of iron can be produced by increasing the MnO content in inclusions belonging to the $MnO\text{-}SiO_2\text{-}FeO$ system. This has the interesting potential to minimize local stress concentrations associated, under applied stress, with inclusion/matrix elastic constant mismatch, possibly reducing in turn the rate of crack nucleation in high-cycle fatigue.

Chapter 5 – Strength of silicon oxide inclusions

Disclaimer: This chapter contains literal reproduction of full paragraphs and figures of the following publication: A. Slagter, J. Everaerts, L. Deillon, A. Mortensen, Strong silicon oxide inclusions in iron, Acta Materialia, 242, (2023), to which the author has contributed. Specifically, the author contributed to the sample production and in-situ testing as well as to the elaboration of finite element simulations of the tests. The author of this thesis was also the writer of the first draft of the manuscript and responsible for the production of the figures.

5.1 Introduction

As described in previous chapters, oxide inclusions are important because they influence the mechanical properties of steel: they affect ductility and toughness and they can be responsible for the initiation of cracks leading to fatigue failure. In contrast with the vast amount of thermochemical data relevant to inclusions in steel, the literature dedicated to their structure and mechanical properties is relatively limited. With the advancement of techniques for the measurement of local material properties, it is now possible to study the structure and mechanical behaviour of individual phases having volumes as small as a few cubic micrometres. Yet, to date, only a few studies have made use of these novel tools to characterize steel inclusions. We show here that micromechanical experiments can be carried out *in-situ* on individual oxide inclusions to measure their strength.

The test methodology implemented here is an adaptation of the procedure presented in [151] and implemented in [152,153]; it consists in testing a pre-notched particle having the shape of a "C", by applying a compressive force normal to the notch. Milling of the notch is performed with a focused ion beam (FIB) and the experiments are coupled with finite element simulations to deduce the maximum tensile strain and stress at the point of fracture. An important advantage of this testing technique is that the development of tensile stresses and fracture initiation are expected in a region of the particle that has not been altered by FIB milling; however, implementation of the technique requires that the iron matrix surrounding the oxide particles be removed prior to testing, *e.g.*, by chemical dissolution of the metal, without affecting the inclusion surface to be probed. Because the only composition among the oxide inclusions produced in this work that is known to have a high resistance to etchants capable of dissolving iron is pure SiO_2 (observed in sample Si_CC, see Chapter 4), results presented here correspond to micromechanical testing carried out only on inclusions in that sample.

5.2 Methodology

5.2.1 In-situ testing

Amorphous, spherical SiO_2 inclusions precipitated within iron in Sample Si_CC (see Chapter 4 for details) were partly exposed after selective dissolution of the iron matrix. This was done by electropolishing for 60 s the matrix in a dilute acidic solution (Struers A2 electrolyte, consisting in ~5 % $HClO_4$ dissolved in a mixture of ethanol and 2-butoxyethanol). Micromechanical test samples were carved out of partially exposed spherical oxide inclusions by milling a deep notch with a Ga^+ Focused Ion Beam (FIB) (Zeiss CrossBeam 540, 30 keV, 20 pA to 300 nA).

Spherical inclusions were specifically targeted for the fabrication of micromechanical test samples not only because they correspond to the most commonly observed morphology in our samples but also because their compact and simple geometry simplifies milling operations, modelling of the test, and interpretation of results. During the milling operation, the iron sample was mounted with its polished surface tilted to a 10° angle with respect to the Ga^+ beam axis (Fig. 5.1 a), as this provides ion beam access to all inclusions that have been exposed along the surface of the sample. A V-shape geometry with a large root curvature radius (Fig. 5.1 b) was used for the notch, instead of the rectangular profile adopted in previous work, to adapt the notch to the spherical shape of the silica inclusions. In addition, for most of the test samples, a portion of the upper lip of the "C" was removed to avoid closure of the C before the fracture of the sample (Fig. 5.1 b).

Testing of the C-shaped particles was performed *in-situ* within the SEM under a pressure of ~ 10^{-6} mbar using a nanomechanical testing system (FemtoTools FT-NMT04, Buchs, Switzerland) equipped with rotation and tilt stages. A diamond flat punch, of diameter 5 μm or 10 μm, was used to impose a vertical displacement on the upper lip of the particles. The punch was mounted on a microelectromechanical sensing probe able to measure both normal and lateral forces up to ± 20000 μN. Tests were performed at a constant displacement speed of 0.02 μm/s, leading to a strain rate along the outer surface of the particles in the range from 1 to 4 x10^{-3} s^{-1}. The samples were aligned in such a way that the direction of the ion beam used in the milling step was (i) parallel to the observation direction during testing and (ii) perpendicular to the diamond punch displacement direction (Fig. 5.1 c). Measurements were performed while observing the test in the SEM, with the exception of four additional tests that were performed with the electron beam off, so as to test whether data were affected by exposure to the electron beam. SEM operating parameters during micromechanical tests were a voltage of 3 keV on a FEG source, with a current on the order of 200 pA scanning an area on the order of 60 μm^2 over the ~ 180 s duration of the test. The cleanliness of the flat punch tip surface was confirmed regularly by SEM inspection and the tip was cleaned when necessary following the procedure detailed in Ref. [194].

Figure 5.1 Schematics of a) the positioning of samples for FIB milling; b) the notch geometry used for the testing of spherical inclusions (viewed along the direction of the ion or electron beams); c) subsequent positioning of the sample for in-situ testing in the SEM.

The system compliance, including the elastic deformation of the iron matrix and that of the frame, was measured in separate experiments. These were performed in the vicinity of tested particles by collecting force-displacement data while compressing, one at a time, the top of partly exposed spherical inclusions that had not been FIB-milled.

The total load point displacement measured while compressing emerging intact spherical inclusions is the sum of displacements caused by the elastic deformation of the load train, by compression of the iron matrix under the particle, and by deformation of the (unnotched) particles under the punch. Knowing that loads during C-shaped particle testing are too small to cause plastic deformation in the iron matrix, the contribution to system compliance of compression of the iron matrix under the particle can be estimated using Sneddon's equation; this returns values, for all tested particles, below $2.17 \; 10^{-3}$ µm/mN, well below measured load train compliance values (on the order of 0.1 µm/mN, see below). This particle-size dependent contribution to the compliance can, thus, be neglected. The other particle-size dependent part of the signal is associated with (intact) spherical particle deformation in the punch/particle contact region. The punch displacement (δ) associated with particle deformation under the indenter can be estimated using Hertz contact theory formulated for a hard punch against a spherical elastic solid [183]:

$$\delta = \left[\frac{9P^2\left(1-v_p^2\right)^2}{16 \; E_p^2 R} \right]^{\frac{1}{3}} \tag{5.1}$$

where P is the load acting on the particle of radius R (measured from SEM images), E_p and v_p are elastic constants for isotropic silica (Young's modulus and Poisson's ratio respectively, taken to equal E_p =72 GPa and v_p =0.17 [100,101]). Calculated values of δ were then subtracted from the force-displacement data of each intact sphere test, to compute the (constant) system compliance that accounts for contributions coming only from the load train including the punch and the iron substrate. This compliance was found to be relatively constant from one particle to the other and during each intact particle compression test (thus validating the approach), and to be on the order of 0.11 µm/mN (equivalent to a stiffness of 9000 N/m).

No signs of plastic deformation were observed in the iron during the micromechanical tests; permanent deformation of the iron matrix was only observed during compliance measurement tests performed on small particles at relatively high loads that were above the load range used when testing inclusions in the same size range.

5.2.2 Finite Element Simulations

Finite-element models of each test were formulated using Abaqus/CAE 6.14-1 (Dassault Systèmes Simulia Corp., Providence, RI, USA, 2014) in order to compute the local strain and stress within the inclusion at the moment of fracture, or at peak load if the notched particle did not fail before the notch was completely closed. The 10° tilt of the iron surface was not accounted for in computations, such that calculations were conducted on three-dimensional models comprising half of each tested, partially embedded, notched silica particle. Meshes were built using quadratic tetrahedral elements (C3D10), with the geometry and dimensions of the particles as measured from SEM images. The particles were assumed to be isotropic, with the same elastic constants as above ($E_p = 72$ GPa and $\nu_p = 0.17$ [99–101]).

In addition to models assuming linear elastic deformation of the silica phase, a second FEM model was run for each fractured particle, in which it was assumed that silica also experiences plastic deformation as dictated by the yield criterion proposed by Kermouche et al. [121]. This was implemented in Abaqus/CAE through the Abaqus Cap Plasticity model using parameters from Ref. [195] and listed in Table 5.1 as Model A. This yield criterion considers that plasticity in silica can be caused not only by shear loading, where the yield stress is characterized by a pure shear critical stress (d in the terminology of Ref. [195]), but also by pure hydrostatic compression, where the onset of plastic densification is characterized by a critical pure hydrostatic compressive yield stress (p_c in the terminology of Ref. [20]). Values for (compressive) yielding according to parameters of Ref. [195] correspond to $d = 7.5$ GPa and $p_c = 11.5$ GPa. In this model, plastic deformation driven by hydrostatic pressure is only present in compression, while for stress states comprising hydrostatic tension, yield is only driven by shear following a classical Von Mises criterion.

Finally, a third (modified) elastoplastic FEM model was run for each fractured particle, using a similar yield criterion, but modified to raise d to 11.5 GPa. This was implemented in order to delay yield in tensile stress space and, through this, confine plastic deformation to the inner notch radius, where the stress state is compressive (see Section 5.4, Discussion).

Given the large deformations attained during the micromechanical tests, geometric nonlinearity was included in the models, meaning that the dimensional change of elements that accompanies their deformation was accounted for in subsequent calculations of both stress and strain. The punch was simulated as a discrete rigid element (*i.e.*, as a flat shell) to which the experimentally measured, compliance-corrected, displacement was imposed. Contact between punch and particle was modelled using classical isotropic Coulomb friction with a penalty friction formulation. The friction coefficient in each model was considered constant and equal to the average ratio of lateral to normal forces registered by the force sensor during the corresponding test, with the observed friction coefficient situated between 0.05 to 0.3. In order to reproduce experimental conditions, in which sliding between the punch and particle surfaces was evidenced, the maximum shear stress allowed at the contact area was set to a low value, namely 600 MPa.

Table 5.1 Abaqus/CAE FEM cap-plasticity parameter values, defined first in the word terminology of the Abaqus Documentation, then between parentheses using word and variable terminology from Ref. [195].

Model/Parameter		Model A - as reported in [121,195]	Model B (modification of Model A to delay tensile yield)
Material Cohesion (yield strength in pure shear, d) (GPa)		7.5	11.5
Angle of Friction (friction angle, β)		0.001	0.001
Cap Eccentricity (R)		1.53	1
Initial Yield Surface Position (initial volumetric strain, $\epsilon_{pl}^{vol}\mathrm{I_o}$)		0	0
Transition Surface Radius (yield surface parameter, α)		1	1
Flow Stress Ratio (yield surface anisotropy in the deviatoric plane, K)		1	1
Cap hardening parameters	p_{c0}	11.5	11.5
	p_c (at 1 % strain) *	12.5	12.5

*Equivalent to a hardening slope (ξ) of 100GPa

Boundary conditions for the lower end of the half-particle were set as a restriction of displacements in all directions (pinning) of an area along the particle bottom surface, with that area defined by the intersection of the particle surface with a plane perpendicular to the loading direction (Fig. 5.2). This (rigid) boundary condition creates a site of stress concentration along the particle surface, situated just above the line of intersection of the (rigid) matrix surface with the particle surface. This poses no problem if this site of stress concentration is remote from the peak stress region created by the notch along the outer particle surface while it is tested. Such was not the case in all tests, however; when this occurred (Figs. 5.2 b & d illustrate this) the iron surface was lowered in FEM simulations to the highest position for which a minimum appears between the stress at the intersection of the particle surface with the iron surface and the peak stress along the particle opposite to the notch (Figs. 5.2 c & e illustrate this).
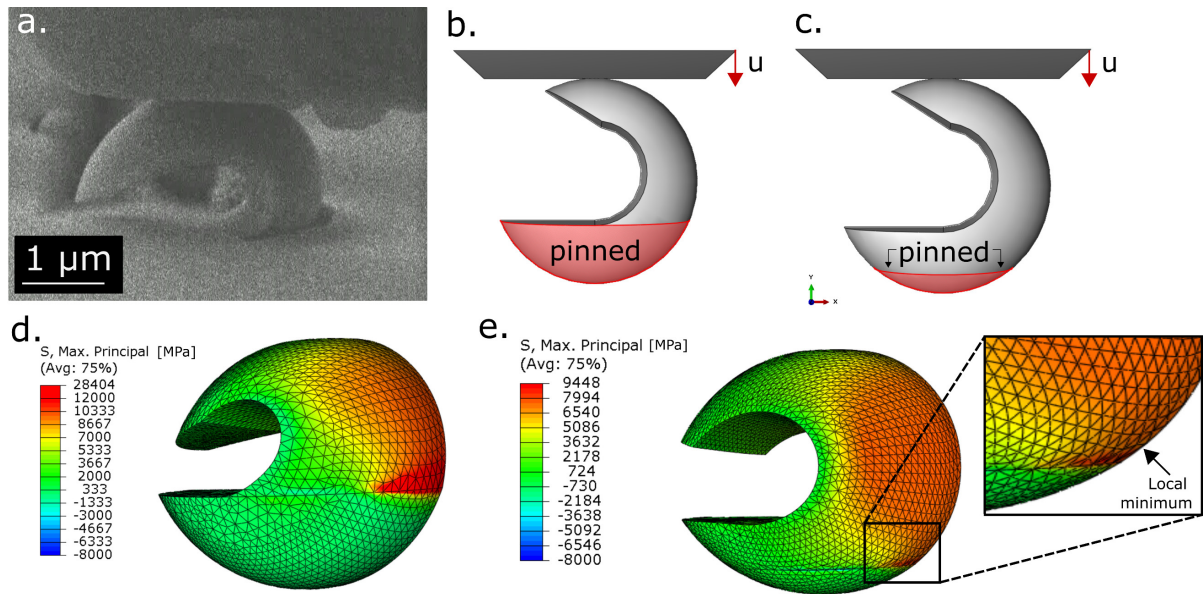
Figure 5.2 Boundary conditions used in FEM model and results from simulations of mechanical tests: a) SEM image of a tested inclusion at the moment of maximum displacement; b) pinned area used in simulation, with zero surface displacement everywhere below the iron surface observed in a; c) same with pinned area top boundary lowered to prevent the development of a region of maximum principal stress along the limit of the pinned area; d) maximum principal stress distribution predicted for the fully elastic model with the pinned area as defined in b; e) same but with pinned area as defined in c.

5.3 Results

C-shaped particle bend tests on the silica inclusions led to significant deformation followed by sudden fracture of the particles in roughly one-third of the tests. Fracture surfaces of the broken inclusions were often irregular, showing signs of multiple crack formation. Some inclusions were smashed by the indenter, while in others (the majority) the upper inclusion half landed at a location remote from the inclusion. Figure 5.3 shows two inclusions for which the fracture surface was comparatively well preserved: in (a) and (b) an inclusion for which a relatively simple and clean fracture surface is seen, in (c) and (d) the single inclusion for which the upper part remained attached to the lower half of the inclusion. For the remaining samples (roughly two thirds) closure of the "C" was reached before fracture of the particle (Fig. 5.4), at which point the tests were stopped and the sample was rapidly unloaded. For some of the non-fractured particles (six out of twenty-seven), the opening of a small crack was observed along the inner, FIB-milled, surface of the notch during unloading; an example of this is given in Fig. 5.4 c and indicated with a black arrow. Load-unload tests conducted while gradually bending C-shaped inclusions showed, even at small loads (below 100 µN), unloading load-displacement lines lower than the loading curve, thus indicating the presence of irreversible deformation in the C-shaped inclusion.
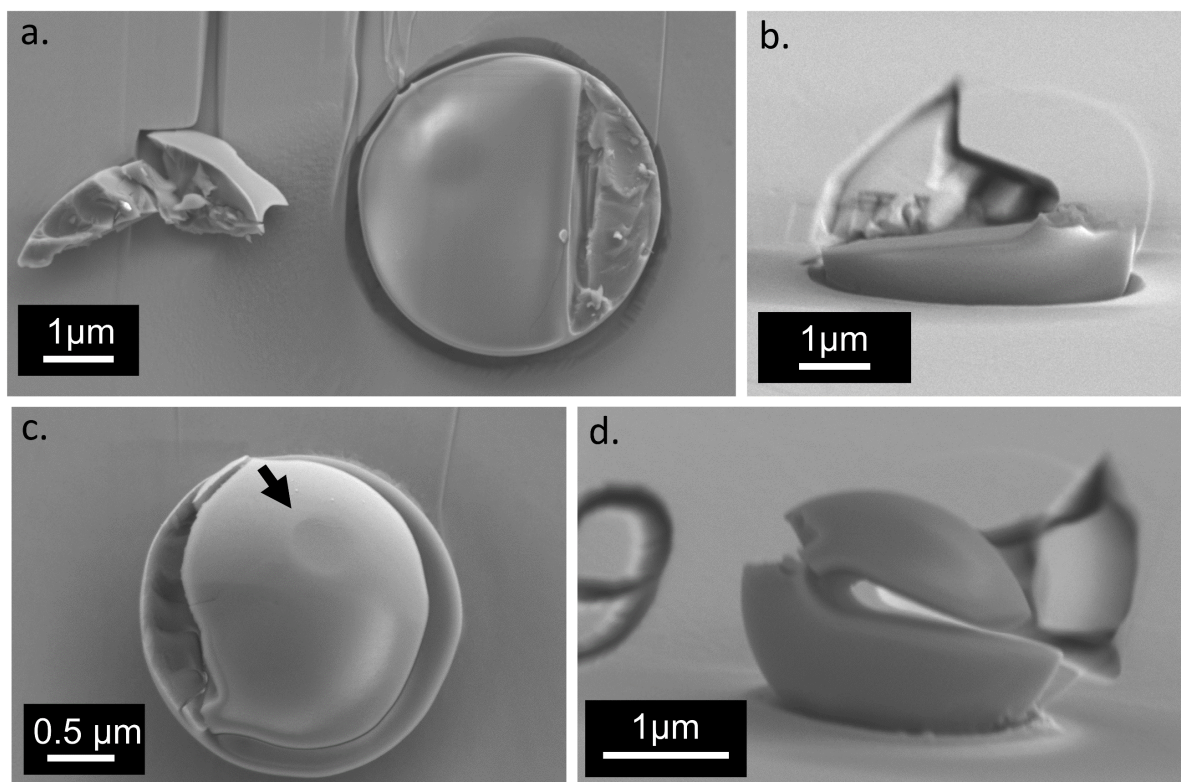
Figure 5.3 Top (a) and (c) and side (b) and (d) view of two fractured particles after testing; note in (c) and (d) that the top portion of the particle remained roughly in place after fracture, and that one can discern (black arrow) a trace of the indenter along the top particle surface, betraying the presence of a small level of compressive silica plastic deformation.
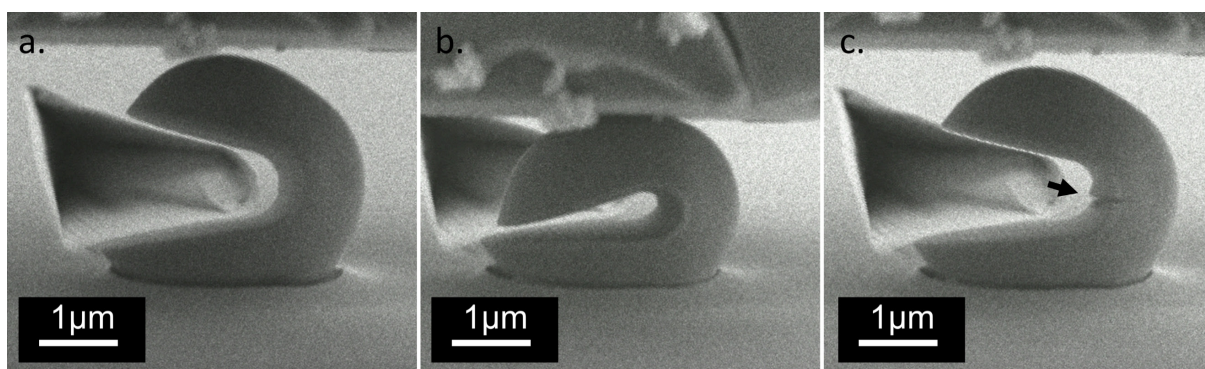

Figure 5.4 Example of non-fractured particle a) before testing; b) at the moment of maximum displacement; c) after unloading where a crack is visible in the inner part of the notch (black arrow).
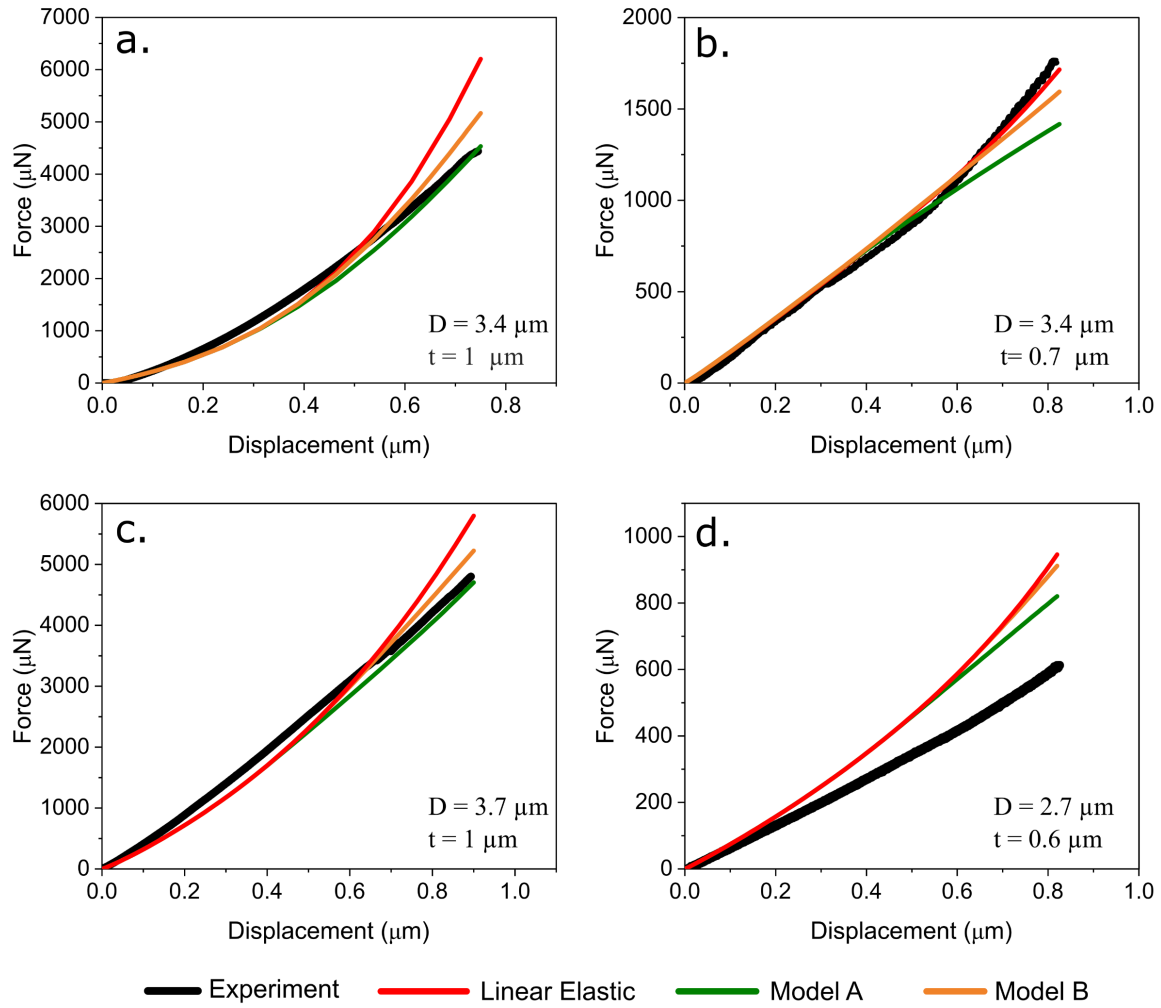
Figure 5.5 Examples of force-displacement data collected from experiments and finite element simulations for four different tests along with each particle diameter (D) and ligament thickness (t); experimental data were corrected to account for the compliance of the substrate and the testing rig. Colours distinguish the curves in the on-line version; experimental data are plotted with a thicker line; simulation curves are ranked vertically downwards in the following order: linear elastic (top), Model B (middle), Model A (lowest).

Force-displacement data (Fig. 5.5) show overall good agreement between experiments and FEM models. The initial portion of the curve is, as expected, not altered by the incorporation of plasticity in the models. Also, again as one would expect, at larger strain levels the force computed for both elasto-plastic models falls below values for purely linear elastic deformation; however, deviations remain small, both between different model predictions and between predictions and experimental data. The main trend observed is that the level of agreement between predictions and data decreases as the particle size decreases (Fig. 5.5 d illustrates this).

The sensitivity of simulations to dimensional input parameters, namely the ligament radius and thickness, as well as the angle of tilt of the compression axis with respect to the normal to the notch plane, was examined with a series of separate simulations. Details of these simulations, presented in Table 5.2 and Figs. 5.6 & 5.7, show that the predicted load-displacement curve is

Table 5.2 Details of variations implemented in FEM models and corresponding results in terms of peak strain, peak stress and peak force.

| Model	Peak Strain	Strain dev. (% as compared to ref.)	Peak Stress (GPa)	Stress dev. (% as compared to ref.)	Peak force (µN)	Force dev. (% as compared to ref.)
Reference	0.136	-	9.8	-	1442.6	-
5° tilt (Fig. 5.7 b)	0.151	**11.0**	10.9	**11.2**	1781.4	**23.5**
5° tilt (Fig. 5.7 c)	0.150	**10.3**	10.9	**11.2**	1758.8	**22.0**
10 % larger notch diameter (Fig. 5.7 d)	0.144	**5.8**	10.4	**6.1**	1211.9	**-16.0**
Notched moved to decrease ligament thickness by 10 %	0.145	**6.6**	10.5	**6.8**	990.0	**-31.4**
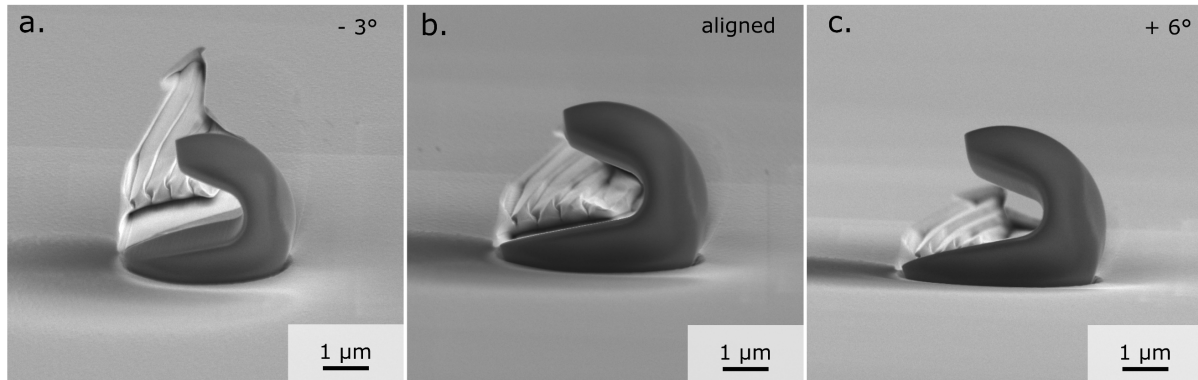
Figure 5. 6 Example of particle alignment with respect to the punch displacement direction (downwards in the images). A good alignment is achieved when the milled notch overlaps (and delineates) the traces left by the ion-beam on the iron surface behind the particle.
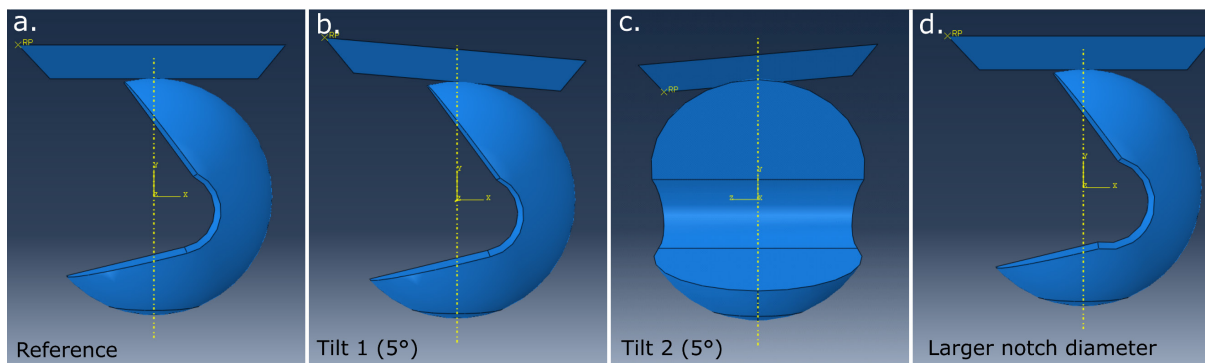

Figure 5. 7 Variations on particle geometry and alignment implemented in FEM simulations to evaluate the sensitivity of obtained strain, stress, and force. a) Particle geometry used as a reference; b & c) punch tilting of 5° in the two different possible directions; d) particle geometry considering a notch radius 10 % larger than that used for the reference dimensions.
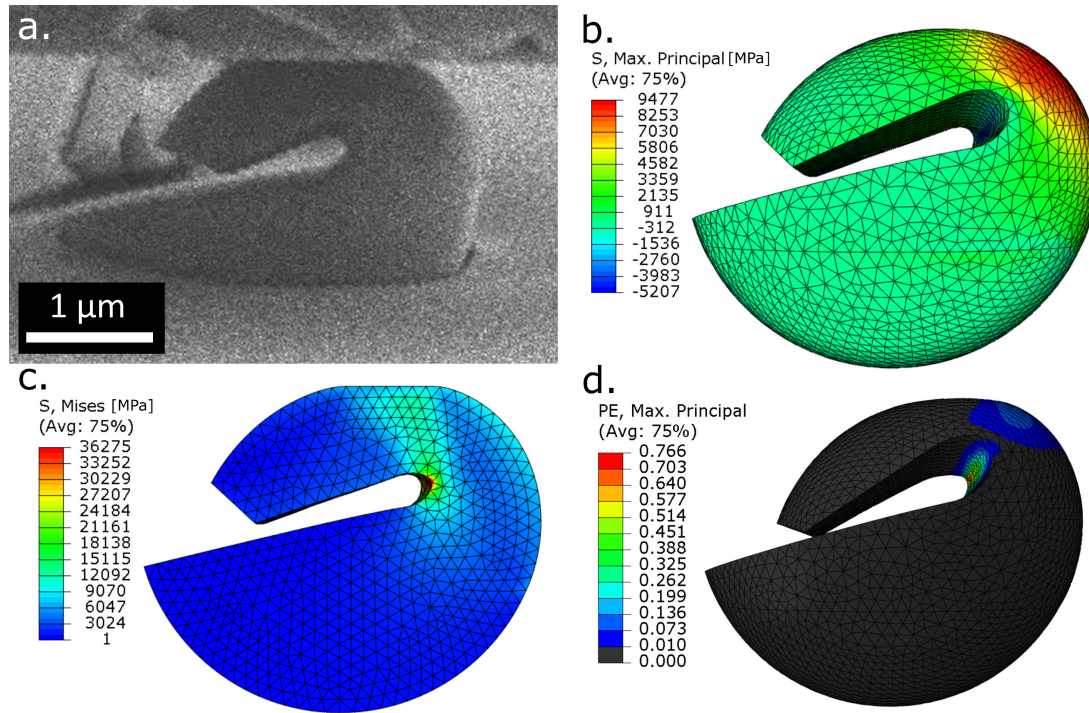
Figure 5.8 a) SEM image of a particle at maximum imaged displacement before fracture; FEM simulation results of: b) maximum principal stress and c) von Mises stress (along the mid-plane cross-section of the particle), both assuming linear elastic behaviour, and d) maximum principal plastic strain predicted for the particle modelled as an elasto-plastic solid with a deformation law defined by Model A.

highly sensitive to those geometrical parameters while the predicted peak stress and strain values are comparatively little affected by those variations.

Detailed model predictions show that (i) high stresses are present in the inner region of the notch, as a combination of shear and hydrostatic stress, and that (ii) the maximum principal stress is tensile and is always located at the outer surface of the C-shaped particles (Fig. 5.8), as one would expect. The incorporation of plastic behaviour in the silica deformation law, using parameters proposed in Refs. [121,195] (Model A), leads to predict the presence of permanent deformation along both the inner and outer surfaces of the particle (Fig 5.8 d). This caps, as one would expect, the observed maximum principal stress at the assumed yield stress, of ~8 GPa, while slightly increasing the strain that simulations predict along the outer surface. Simulations carried out with a yield criterion modified to restrict plastification to the inner notch surface (Model B) show similar peak stress and strain facture values along the particle outer surface as those obtained without yield, *i.e.*, assuming fully linear elastic deformation.

Figures 5.9 a & c present values of the maximum principal strain and stress reached according to FEM models using a linear elastic deformation law, for particles that fractured (filled symbols) and particles that did not fail (open symbols), with an indication of data collected with the electron beam of the SEM turned off. Figures 5.9 b & d show the maximum strain and stress reached by fractured particles according to elasto-plastic models A and B (described in Section 5.2.2). Points are separated along the horizontal direction in the plots of this figure

according to the product of the ligament thickness times the notch diameter times the particle diameter. This is a rough indicator of the stressed volume, since that volume scales roughly with each of those three lengths along each of three perpendicular directions.
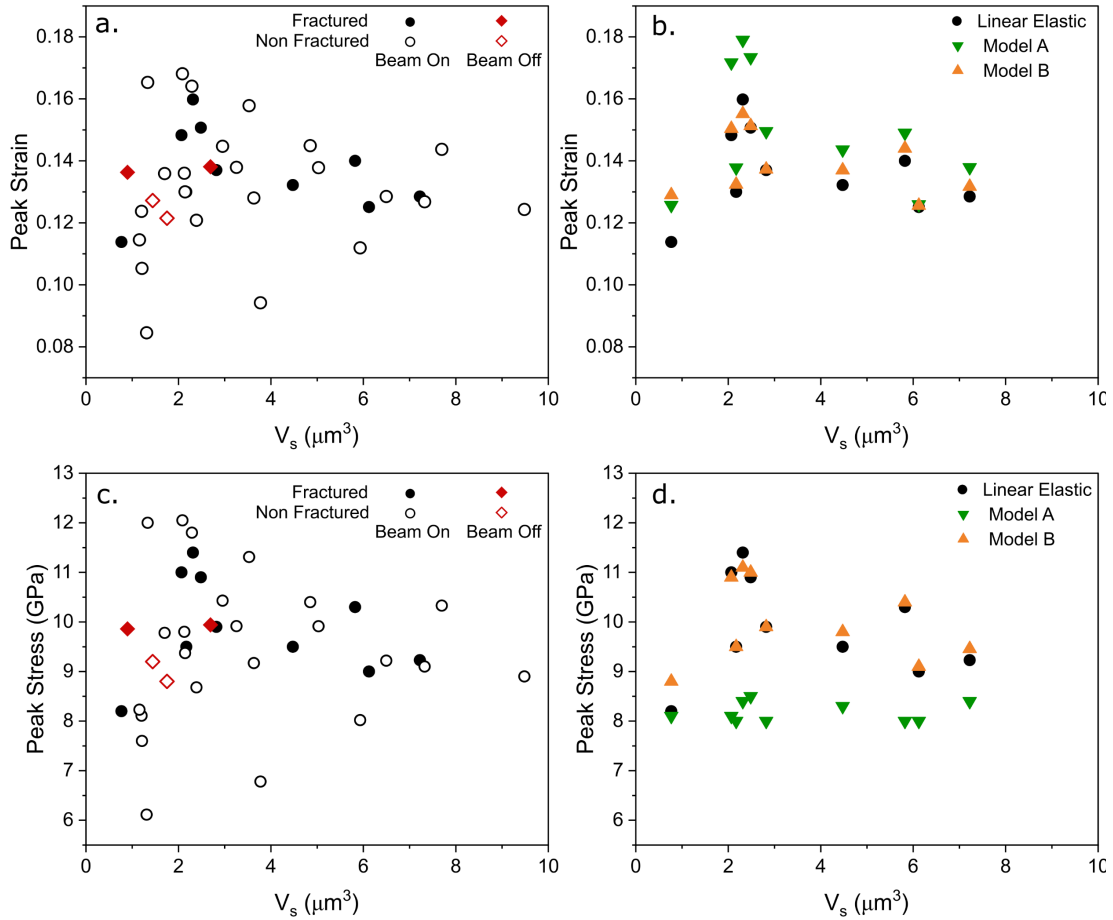

Figure 5.9 Maximum principal strain and stress obtained by FEM modelling of the tests: (a) and (c) of all tested particles and assuming linear elasticity; (b) and (d) of particles that fractured, assuming linear elasticity or assuming elastoplastic behaviour according to Models A or B (see Table 5.2). The horizontal axis (V_s) in all plots is an estimation of the stressed volume computed as the product of the ligament thickness times the notch diameter times the particle diameter of each sample.

5.4 Discussion

The main observation emerging from the present data is the spectacularly high resistance to fracture that is measured here, by means of the C-shaped specimen bend test, in spherical amorphous silica inclusions. This result is unaffected by the electron beam, Fig. 5.9 a, since data with the beam turned off fall near the middle of the range displayed by *in-situ* data. This lack of a discernible influence of the relatively low-intensity beam of the SEM (compared to that of a TEM) on micromechanical measurements conducted on silica agrees with observations reported in Refs. [156,196].

Both elastic and elastoplastic simulations of deformation within the bent inclusions lead to conclude that, along their outer surface, tensile strains in the range from 8 to 17 % were reached

before inclusion fracture. Those are remarkably high levels of tensile strain for amorphous silica. Fracture strain values of this magnitude in glass are typical of high-perfection silica fibres fractured in two-point bend tests, which return fracture strain values in the range from 6 to 8.5 % under ambient conditions (with 50 % relative humidity), or from to 16 to 18 % when testing is conducted under liquid nitrogen (*i.e.*, free of the influence of moisture) [100,197–199]. In tensile testing, failure strain values in the same range (12-15 %) are reported for metallized fibres that were coated from the melt [200]. Those values all exceed one-half of the intrinsic tensile fracture strain, situated near 20 % [199,201,202], that was derived for silica tested under load-control knowing its strain-dependent modulus.

What is the corresponding failure stress? If one assumes fully linear elastic deformation, then the tensile strength values measured here for silica inclusions along their surface are predicted by finite element simulations to be on the order of 10 GPa, Fig. 5.9. This is again on the order of values measured in tensile testing for pure, high-quality silica fibres in either vacuum [203] or liquid nitrogen, where maximum reported values reach 14 GPa [100,202–205]. Values in the same range (12-15 GPa) are reported for metallized fibres that were coated from the melt [200]. Values measured with uncoated high-quality silica fibres in air, namely ∼5-7 GPa [100,133,197,198,200,203,205], are noticeably lower, likely due to the effect of moisture in the testing environment.

For the large strain and stress levels observed in the current study, the implications of assuming a linear elastic behaviour must, however, be considered, even if predictions from FEM simulations match relatively well-recorded load-displacement curves (Fig. 5.5), since (i) the elastic modulus of silicate glasses is known to depend on strain, especially for high strain levels, and since (ii) significant plastic deformation has been observed in glass at high stress values.

It is known that the elastic modulus of amorphous silica increases by up to 25 % upon uniaxial tensile straining, and does so at least up to strains on the order of 5 to 10 % [201,202]. Measurements at higher strain levels are difficult, but extrapolations from lower strain data [201] show that the linear elastic assumption, for tensile conditions up to strains on the order of ∼20 %, underestimates the observed failure stress. So the influence of non-linear elasticity will be to *increase* the tensile strength values derived from the present data assuming linear elastic glass deformation, by an amount lower than 20 % (given that the present tests are in essence bend tests [206]).

Load-unload cycles conducted on C-shaped inclusions gave, as mentioned above, signs of the presence of irreversible deformation. Plasticity, if present, will impose a cap on the maximum strength of the inclusion material if plastic deformation can be triggered under tension. There is substantial evidence showing that amorphous silica can deform plastically to total strains in the order of 20 % in experiments where the stress state is predominantly compressive, such as in indentation, diamond anvil cell compression [209], or micropillar compression testing [196,154,120,155]. The common observation in those experiments is that amorphous silica undergoes permanent deformation under stresses around 7 to 9 GPa, with evidence for both densification and shear as the underlying mechanisms that cause plasticity. In experiments of this study, the crack opening observed in the inner part of the notch during the unloading of

some of the non-fractured C-shaped tests, Fig. 5.4 c, and also the slight particle surface deformation that one can see (in the location marked with a black arrow) at the top of the fractured particle half in Fig. 5.3 c, indicate that some level of plastic deformation indeed occurred in regions of the inclusions that were subjected to compressive stress states of sufficiently high value (and, for the notch root region, to modification by gallium ion implantation). Linear elastic finite element simulations also suggest that plastification is to be expected in the inner region of the notch while the C-shaped inclusions were bent: predicted Von Mises stress values at that location reach values near 35 GPa in some of the linear elastic model calculations (those for samples with thicker ligaments).

We therefore also conducted finite element simulations assuming the presence of plasticity in the amorphous silica inclusions. We used a model derived directly from the literature (Model A), and then modified it in a way to see, in simulations, silica plastification only in regions of the inclusions subjected to compressive stress states (Model B, produced by raising the shear yield stress in Model A). The reason for imposing this restriction is that there are no signs in our data, nor to the best of our knowledge in the literature [195], that plastic deformation appears in amorphous silica when it is deformed under predominantly tensile stress. In present samples the outer surface across the notch root in bent samples (see Fig. 5.4 c) remains smooth after unloading, with no sign of permanent deformation or rippling that would likely result if the outer surface had experienced substantial plastic elongation while the inclusion was under maximum load, given that upon unloading that region would experience a compressive surface state. More generally, the failure of high-strength amorphous silica fibres in bending or tensile testing is regularly reported to be brittle, with flat fracture surfaces (when they can be observed) [210]. Furthermore, if amorphous silica were prone to deform plastically under tension, then its toughness should exceed twice its surface energy. It is thus most likely that plastic deformation was experienced only in the inner part of the C-shape and not on the outer surface of deformed C-shape inclusions, leading us to believe that strain and stress values experienced by inclusions tested here are probably better predicted by Model B than by Model A.

Predictions of both models are plotted in Figure 5.9 b & d for samples that experienced fracture. Predictions of Model A for the tensile failure stress of fractured particles remain (obviously) capped by the assumed tensile yield stress. Predictions of Model B come close to values predicted by linear elasticity (in fact they exceed slightly predictions from linear elasticity for both strain and stress, which is a priori not expected; likely this is a result of densification on the compressive side of the notch). We thus conclude that compressive plastic deformation in the material does not affect significantly peak tensile fracture stress values that emerge from the present experiments.

It is unlikely that the etching step used to expose the inclusions would explain why such high failure strains were reached here, because (i) silica is non-conductive and hence was not electrolytically etched while the matrix was removed; (ii) exception made for hydrofluoric or phosphoric acid, which were not used here, amorphous high-purity silica is known to be inert in acidic environments [211], and finally (iii) where high-strength glass fibres have been etched in corrosive environments, their strength is nearly always found to have *decreased* [100,211–214] (an exception is with fibres that have a rough or damaged surface, the strength of which

can be increased from lower values to a few GPa by means of an etch that reduces the depth of surface irregularities, however, this situation does not apply here [100]).

In summary, the very high strains to failure that are measured here are thus likely not affected by artefacts, leading us to conclude that silica inclusions precipitated within iron in the present work display, along their surface, tensile strength and strain values that match what has been reported for the strongest silica fibres produced to date, namely values in the range 8 – 17 % for strain, and 6 to 11 GPa for stress. Those values come near the upper limit of what is known to be possible in amorphous silica. Using a simple fracture mechanics back-of-the-envelope calculation, since for amorphous silica $K_{Ic} \approx 0.75$ MPa$\sqrt{\mathrm{m}}$ [100], peak defect depths are therefore everywhere below 1 to 3 nm along the inclusion surfaces. Since in steel the amorphous silica phase is isolated from the surrounding atmosphere, it is also reasonable to expect the inclusions to be shielded from water and thus retain their high strength over prolonged periods of time, the sole (but important) exception being inclusions located along the surface of the metal.

In turn, assuming that the tested spherical inclusion regions are representative of entire inclusions, this implies first that it is possible to deoxidize iron without necessarily introducing weak defects in its midst if the inclusions can be made to be strongly bonded to the matrix. We have not tested here the strength of the particle/matrix interface (this is the subject of ongoing work); however, unless it is quite weak (in which case interfacial voiding might weaken steel containing such inclusions), and unless they emerge at the surface of the metal, the present inclusions are likely not to fracture within iron, even when the alloy is subjected to elevated tensile stress. A second implication of the findings reported here is that, given its high fracture stress, perhaps amorphous silica precipitated within iron might be used as a reinforcing phase. If equally smooth and strong amorphous silica inclusions can be produced in much larger proportions within steel, then one would have made a material with an admittedly lowered modulus, but with a potentially high strength-to-density ratio, entirely made from abundant elements (iron, carbon, silicon and oxygen), and – if one can bypass initial silica reduction - with a potentially lower carbon footprint than steel given that only a portion of the material would be reduced from ore.

5.5 Conclusion

The fracture stress of spherical amorphous silica inclusions formed by precipitation within iron melts can be measured using an adaptation of the C-shaped microsample testing method that was developed to test, free of FIB artefacts, the strength of reinforcing phases within metallic materials. Results show that failure strains in the range from 8 to 17 % are attained, corresponding to strength values of the silica inclusions that reach or exceed (since most particles tested reached such values without breaking) the range from 6 to 11 GPa. Those values approach the upper bound for the strength of dry amorphous silica: oxide inclusions in steel can be very strong.

Chapter 6 - General Conclusion

The goal of this thesis has been to add to the science of steel an exploration of the relationship between processing, structure, and properties of oxide inclusions that appear in iron alloys as a result of precipitation reactions between oxygen and deoxidising elements within the molten metal.

The results of this work show that oxide inclusions of controlled nature can be fabricated in the laboratory by deoxidation of high-purity iron melts. The chemistry and structure of thus produced oxide inclusions, however, can present remarkable deviations from equilibrium conditions and vary considerably across millimetre-sized laboratory casts. Consequently, accurate prediction of the composition, structure, and, therefore, properties of these oxide precipitates requires consideration, in addition to thermodynamics, of the kinetics of various processes, including inclusion precipitation within the molten metal, but also that of precipitation reactions of different phases within the oxides. This non-equilibrium nature of inclusions precipitated in liquid iron, in turn, emphasizes the need to measure local inclusion mechanical properties directly, on the inclusions themselves.

In spite of the complexity that oxide inclusions can show, their local properties can be measured. The need to assess the stiffness and hardness of micrometre-sized oxide inclusions has led to the development of a method to extract matrix-independent inclusions properties that can be extended to a wide range of other particle-matrix material systems. The correction is based on analytical considerations coupled with finite element calculations and shows that a relatively precise and reliable computation of the hardness and stiffness properties of embedded particles can be achieved by probing a large number of individual particles and averaging the corrected data.

Indentation properties measured in inclusions in the Mn-Si-Fe oxide system within laboratory samples show that the oxide stiffness and hardness are significantly increased when the MnO content exceeds 67 wt. %, while similar properties measured in Al-Si-Ca oxides remain relatively unchanged. Inclusion hardness values determined for all oxide inclusions in this work tend to be relatively high when compared with those of the metallic matrix, being (with few exceptions) above 6 GPa.

Strength determinations have been obtained by adapting a micromechanical testing technique to probe the properties of partially exposed and notched spherical silica inclusions. Strength determinations made on SiO_2 inclusions have shown that these oxide precipitates, usually seen as a nuisance, can, in fact, have remarkably high mechanical properties. For silica inclusions, failure strains and stresses have been measured to be in the range of 8 to 17 % and in the order of 10 GPa, respectively, and thus match the highest values reported for dry silica.

Chapter 7 - Perspectives for future work

We have presented here hardness, stiffness, and strength determinations in a reduced number of oxide inclusion compositions. An interesting direct continuation of this work would comprise similar investigations for other oxide compositions, which could map the two ternary systems that have been investigated here (Al_2O_3-SiO_2-CaO and MnO-SiO_2-FeO) but also extend results to oxide inclusions that contain other elements usually found in steel products such as MgO, TiO, Cr_2O_3.

In this pursuit, nanoindentation testing could be coupled with an increase in the palette of techniques used to characterize the structure of the observed oxide phases, for example, via transmission electron microscopy, electron backscattered diffraction, or Raman spectroscopy. In light of the advances in micromechanical testing techniques, temperature effects can also be explored on inclusions properties, as this would shed light on inclusion behaviour during hot-forming operations.

A major challenge that was encountered in probing the strength of inclusions with other compositions than pure silica has been their lower resistance to acid attack, by the solvent that is used to partially remove the iron matrix needed to access the individual particles so that they can be tested. If a solvent is identified that can remove the iron matrix without affecting the oxide inclusion surface, strength determinations using the C-shaped testing method could also be implemented in inclusions belonging to other oxide systems. Coupled with high-temperature testing this could provide a rich bank of useful and interesting data.

An important aspect not explored during this thesis but currently being investigated as part of the project that funded this dissertation is that of the inclusion-matrix interfacial strength. The properties of the interface between non-metallic inclusions and the metallic matrix play a role as important as that of intrinsic inclusion properties in determining stress distributions and the failure mechanism in inclusion-containing materials. These properties have been, so far, deduced from the strain to failure observed in macroscopic tests but can, using the present fabrication methods and dedicated micromechanical testing techniques, be probed directly. The resulting databank, coupled with measurements of inclusion stiffness, hardness, and where possible, strength, would likely be a guide of great utility in the design of modern steel alloys and steelmaking practice.

References

[1] L. Holappa, Secondary Steelmaking, in: Treatise on Process Metallurgy, Elsevier, 2014.

[2] L. Zhang, Nucleation, Growth, Transport, and Entrapment of Inclusions During Steel Casting, JOM. 65 (2013) 1138–1144. https://doi.org/10.1007/s11837-013-0688-y.

[3] A.L.V. da Costa e Silva, Non-metallic inclusions in steels – origin and control, Journal of Materials Research and Technology. 7 (2018) 283–299. https://doi.org/10.1016/j.jmrt.2018.04.003.

[4] L. Holappa, O. Wijk, Inclusion Engineering, in: Treatise on Process Metallurgy, Elsevier, 2014.

[5] L. Holappa, S. Nurmi, A. Jokilaakso, Review on interactions between slag, steel and inclusions in secondary steelmaking, Proceedings of the 7th International Congress on Science and Technology of Steelmaking. (2018) 10.

[6] J.R. Davis, ed., ASM Metals Handbook, 10th ed., ASM International, Materials Park, OH44073, 1990.

[7] B. Glasgal, Bearing steel 20/20 – a steelmaker's view point – a look back 20 years and a look forward 20 years, Bearing Steels: Into the 21st Century. (1998).

[8] J.M. Beswick, ed., Bearing Steel Technology-Advances and State of the Art in Bearing Steel Quality Assurance: 7th Volume, ASTM International, 100 Barr Harbor Drive, PO Box C700, West Conshohocken, PA 19428-2959, 2007. https://doi.org/10.1520/STP1465-EB.

[9] L. Zhang, B.G. Thomas, Inclusions in Continuous Casting of Steel, XXIV National Steelmaking Symposium. (2003) 138–183.

[10] L. Zhang, B.G. Thomas, State of the Art in Evaluation and Control of Steel Cleanliness., ISIJ International. 43 (2003) 271–291. https://doi.org/10.2355/isijinternational.43.271.

[11] H.K.D.H. Bhadeshia, Steels for bearings, Progress in Materials Science. 57 (2012) 268–435. https://doi.org/10.1016/j.pmatsci.2011.06.002.

[12] R. Kiessling, Clean steel - a debatable concept, Metal Science. 14 (1980) 161–172. https://doi.org/10.1080/02670836.2020.12097372.

[13] B.A. Webler, P.C. Pistorius, A Review of Steel Processing Considerations for Oxide Cleanliness, Metall Mater Trans B. (2020). https://doi.org/10.1007/s11663-020-01949-y.

[14] M.C. Flemings, (B) Formation of oxide inclusions during solidification, International Metals Reviews. 22 (1977) 201–207. https://doi.org/10.1179/imtr.1977.22.1.187.

[15] L. Zhang, C. Guo, W. Yang, Y. Ren, H. Ling, Deformability of Oxide Inclusions in Tire Cord Steels, Metall and Materi Trans B. 49 (2018) 803–811. https://doi.org/10.1007/s11663-017-1134-2.

[16] S. Chen, M. Jiang, X. He, X. Wang, Top slag refining for inclusion composition transform control in tire cord steel, Int J Miner Metall Mater. 19 (2012) 490–498. https://doi.org/10.1007/s12613-012-0585-3.

[17] L. Zhang, State of the Art in the Control of Inclusions in Tire Cord Steels - a Review, Steel Research International. 77 (2006) 158–169. https://doi.org/10.1002/srin.200606370.

[18] N. Ånmark, A. Karasev, P. Jönsson, The Effect of Different Non-Metallic Inclusions on the Machinability of Steels, Materials. 8 (2015) 751–783. https://doi.org/10.3390/ma8020751.

[19] K. Kirihara, Production Technology of Wire Rod for High Tensile Strength Steel Cord, Kobelco Technol. Rev. 30 (2011) 62–65.

[20] G. Krauss, Steels: processing, structure, and performance, second edition, 2nd ed., ASM International, 2015.

[21]   M. Lind, L. Holappa, Transformation of Alumina Inclusions by Calcium Treatment, Metall and Materi Trans B. 41 (2010) 359–366. https://doi.org/10.1007/s11663-009-9337-9.

[22]   S. Abraham, R. Bodnar, J. Raines, Y. Wang, Inclusion engineering and metallurgy of calcium treatment, J. Iron Steel Res. Int. 25 (2018) 133–145. https://doi.org/10.1007/s42243-018-0017-3.

[23]   N. Verma, P.C. Pistorius, R.J. Fruehan, M. Potter, M. Lind, S. Story, Transient Inclusion Evolution During Modification of Alumina Inclusions by Calcium in Liquid Steel: Part I. Background, Experimental Techniques and Analysis Methods, Metall and Materi Trans B. 42 (2011) 711–719. https://doi.org/10.1007/s11663-011-9516-3.

[24]   N. Verma, P.C. Pistorius, R.J. Fruehan, M. Potter, M. Lind, S.R. Story, Transient Inclusion Evolution During Modification of Alumina Inclusions by Calcium in Liquid Steel: Part II. Results and Discussion, Metall and Materi Trans B. 42 (2011) 720–729. https://doi.org/10.1007/s11663-011-9517-2.

[25]   L. Zheng, A. Malfliet, P. Wollants, B. Blanpain, M. Guo, Effect of surfactant Te on the behavior of alumina inclusions at advancing solid-liquid interfaces of liquid steel, Acta Materialia. 120 (2016) 443–452. https://doi.org/10.1016/j.actamat.2016.08.046.

[26]   R. Dekkers, B. Blanpain, P. Wollants, Crystal growth in liquid steel during secondary metallurgy, Metall and Materi Trans B. 34 (2003) 161–171. https://doi.org/10.1007/s11663-003-0003-3.

[27]   N. Aritomi, K. Gunji, Morphology and Formation Mechanism of Dendritic Inclusions in Iron and Iron-Nickel Alloys Deoxidized with Silicon and Solidified Unidirectionally, ISIJ Int. 19 (1979) 152–161. https://doi.org/10.2355/isijinternational1966.19.152.

[28]   S. Nurmi, S. Louhenkilpi, L. Holappa, Optimization of Intensified Silicon Deoxidation, Steel Research International. 84 (2013) 323–327. https://doi.org/10.1002/srin.201200178.

[29]   J. Poirier, A review: influence of refractories on steel quality, Metall. Res. Technol. 112 (2015) 410. https://doi.org/10.1051/metal/2015028.

[30]   F. Huang, L. Zhang, Y. Zhang, Y. Ren, Kinetic Modeling for the Dissolution of MgO Lining Refractory in Al-Killed Steels, Metall and Materi Trans B. 48 (2017) 2195–2206. https://doi.org/10.1007/s11663-017-0996-7.

[31]   S.P.T. Piva, D. Kumar, P.C. Pistorius, Modeling Manganese Silicate Inclusion Composition Changes during Ladle Treatment Using FactSage Macros, Metall and Materi Trans B. 48 (2017) 37–45. https://doi.org/10.1007/s11663-016-0764-0.

[32]   I.-H. Jung, S.A. Decterov, A.D. Pelton, Computer Applications of Thermodynamic Databases to Inclusion Engineering, ISIJ International. 44 (2004) 527–536. https://doi.org/10.2355/isijinternational.44.527.

[33]   I.-H. Jung, Overview of the applications of thermodynamic databases to steelmaking processes, Calphad. 34 (2010) 332–362. https://doi.org/10.1016/j.calphad.2010.06.003.

[34]   S.K. Choudhary, Thermodynamic Evaluation of Inclusion Formation during Cooling and Solidification of Low Carbon Si-Mn Killed Steel, Materials and Manufacturing Processes. 27 (2012) 925–929. https://doi.org/10.1080/10426914.2011.602797.

[35]   F.A. Elrefaie, W.W. Smeltzer, Thermodynamics of the system iron-aluminum-oxygen between 1073 K and 1573 K, Metallurgical Transactions B. 14B (1983) 85.

[36]   T. Botelho, G. Medeiros, G.L. Ramos, A. Costa e Silva, The Application of Computational Thermodynamics in the Understanding and Control of Clogging and Scum in Continuous Casting of Steel, J. Phase Equilib. Diffus. 38 (2017) 201–207. https://doi.org/10.1007/s11669-017-0525-z.

[37]   A. Costa e Silva, Applications of Multicomponent Databases to the Improvement of Steel Processing and Design, J. Phase Equilib. Diffus. 38 (2017) 916–927. https://doi.org/10.1007/s11669-017-0575-2.

[38]   Y.-B. Kang, H.S. Kim, J. Zhang, H.-G. Lee, Practical application of thermodynamics to inclusions engineering in steel, Journal of Physics and Chemistry of Solids. 66 (2005) 219–225. https://doi.org/10.1016/j.jpcs.2004.08.048.

[39]   Y.-B. Kang, H.-G. Lee, Inclusions Chemistry for Mn/Si Deoxidized Steels: Thermodynamic Predictions and Experimental Confirmations, ISIJ International. 44 (2004) 1006–1015. https://doi.org/10.2355/isijinternational.44.1006.

[40]   J.H. Park, L. Zhang, Kinetic Modeling of Nonmetallic Inclusions Behavior in Molten Steel: A Review, Metall Mater Trans B. 51 (2020) 2453–2482. https://doi.org/10.1007/s11663-020-01954-1.

[41]   J. Björklund, M. Andersson, P. Jönsson, Equilibrium between slag, steel and inclusions during ladle treatment: comparison with production data, Ironmaking & Steelmaking. 34 (2007) 312–324. https://doi.org/10.1179/174328107X168039.

[42]   R. Dekkers, B. Blanpain, P. Wollants, F. Haers, C. Vercruyssen, B. Gommers, Non-metallic inclusions in aluminium killed steels, Ironmaking & Steelmaking. 29 (2002) 437–444. https://doi.org/10.1179/030192302225004584.

[43]   M.-A. Van Ende, M.X. Guo, E. Zinngrebe, R. Dekkers, J. Proost, B. Blanpain, P. Wollants, Morphology and growth of alumina inclusions in Fe–Al alloys at low oxygen partial pressure, Ironmaking & Steelmaking. 36 (2009) 201–208. https://doi.org/10.1179/174328109X401550.

[44]   O. Adaba, R.J. O'Malley, L.N. Bartlett, Effect of Preexisting Inclusions on the Size and Morphology of Al2O3: Results from Two-Stage and Fixed Supersaturation Deoxidation, Metall Mater Trans B. (2020). https://doi.org/10.1007/s11663-020-01884-y.

[45]   W. Tiekink, R. Boom, A. Overbosch, R. Kooter, S. Sridhar, Some aspects of alumina created by deoxidation and reoxidation in steel, Ironmaking & Steelmaking. 37 (2010) 488–495. https://doi.org/10.1179/030192310X12700328925822.

[46]   L. Zheng, A. Malfliet, P. Wollants, B. Blanpain, M. Guo, Effect of Impurity Te on the Morphology of Alumina Particles in Molten Iron, ISIJ International. 56 (2016) 1529–1536. https://doi.org/10.2355/isijinternational.ISIJINT-2015-621.

[47]   N. Aritomi, K. Gun, On the Formation of Dendritic Inclusion from a Spherical Primary Silica in Iron- lO% Nickel Alloy Deoxidized with Silicon, ISIJ Int. 20 (1980) 26–32.

[48]   T.B. Braun, J.F. Elliott, M.C. Flemings, The clustering of alumina inclusions, MTB. 10 (1979) 171–184. https://doi.org/10.1007/BF02652461.

[49]   H. Duan, Y. Ren, B.G. Thomas, L. Zhang, Agglomeration of Solid Inclusions in Molten Steel, Metall Mater Trans B. 50 (2019) 36–41. https://doi.org/10.1007/s11663-018-1478-2.

[50]   D. Kumar, M.E. Ferreira, P.C. Pistorius, Comparing Agglomeration Behavior of Inclusions Observed on Steel-Argon Interafce in Confocla Laser Scanning Microscope Experiments and in Bulk Steel, in: Kanpur, India, 2017: p. 4.

[51]   K. Sasai, Agglomeration and removal of alumina inclusions in molten steel with controlled concentrations of interfacial active elements, ISIJ International. 60 (2020) 409–418. https://doi.org/10.2355/isijinternational.ISIJINT-2019-107.

[52]   H. Suito, H. Ohta, Characteristics of Particle Size Distribution in Early Stage of Deoxidation, ISIJ Int. 46 (2006) 33–41. https://doi.org/10.2355/isijinternational.46.33.

[53]   P.A. Thornton, The influence of nonmetallic inclusions on the mechanical properties of steel: A review, Journal of Materials Science. 6 (1971) 347–356.

[54]   R. Lagneborg, The influence of non-metallic inclusions on properties in steel - a review, in: Swedish Symposium on Non-Metallic Inclusions in Steel, Hans Nordberg and Rolf Sandström Eds., Uddeholms AB, Hagfors, Sweden, 1981: pp. 285–352.

[55]   W. Leslie, Inclusions and mechanical properties, Mechanical Working and Steel Processing XX. (1982) 3–50.

[56]   P. Kaushik, J. Lehmann, M. Nadif, State of the Art in Control of Inclusions, Their Characterization, and Future Requirements, Metall and Materi Trans B. 43 (2012) 710–725. https://doi.org/10.1007/s11663-012-9646-2.

[57]   A.L.V. da Costa e Silva, The effects of non-metallic inclusions on properties relevant to the performance of steel in structural and mechanical applications, Journal of Materials Research and Technology. 8 (2019) 2408–2422. https://doi.org/10.1016/j.jmrt.2019.01.009.

[58]   A. Pineau, A.A. Benzerga, T. Pardoen, Failure of metals I: Brittle and ductile fracture, Acta Materialia. 107 (2016) 424–483. https://doi.org/10.1016/j.actamat.2015.12.034.

[59]   A. Melander, J. Steninger, The roles of sulphides, oxides and pearlite in the ductile fracture of a niobium microalloyed steel, Materials Science and Engineering. 52 (1982) 239–248. https://doi.org/10.1016/0025-5416(82)90151-3.

[60]   F.M. Beremin, Cavity formation from inclusions in ductile fracture of A508 steel, MTA. 12 (1981) 723–731. https://doi.org/10.1007/BF02648336.

[61]   Y. Furuya, Gigacycle fatigue of high-strength steel caused by MnS inclusions, Materials Science and Engineering: A. 824 (2021) 141840. https://doi.org/10.1016/j.msea.2021.141840.

[62]   R. Tricot, J. Monnot, M. Lluansi, How Microstructural Alterations Affect Fatigue Properties of 52100 Steel, Metals Engineering Quarterly. 12 (1972) 39-.

[63]   S.S. Babu, The mechanism of acicular ferrite in weld deposits, Current Opinion in Solid State and Materials Science. 8 (2004) 267–278. https://doi.org/10.1016/j.cossms.2004.10.001.

[64]   L.D. Way, Cleanness, castability, and surface quality of formable sheet steels, Materials Science and Technology. 17 (2001) 1175–1190. https://doi.org/10.1179/026708301101509142.

[65]   S. Kumar, K.K. Keshari, A. Deva, R.K. Singh, S. Roy, V. Kumar, S. Toppo, K. Abhishek, N. Pradhan, Abrupt Casting Failures Due to Sub Entry Nozzle Clogging in Calcium Treated Aluminum Killed Steel, J Fail. Anal. and Preven. (2022). https://doi.org/10.1007/s11668-022-01569-5.

[66]   W. Yang, H. Duan, L. Zhang, Y. Ren, Nucleation, Growth, and Aggregation of Alumina Inclusions in Steel, JOM. 65 (2013) 1173–1180. https://doi.org/10.1007/s11837-013-0687-z.

[67]   Y. Wang, C. Liu, Agglomeration Characteristics of Various Inclusions in Al-killed Molten Steel Containing Rare Earth Element, Metall Mater Trans B. 51 (2020) 2585–2595. https://doi.org/10.1007/s11663-020-01938-1.

[68]   Y. Wang, C. Liu, In Situ Observation of Transient Evolution of Inclusions by Ca Treatment in Molten Steel, Metall Mater Trans B. 53 (2022) 2768–2773. https://doi.org/10.1007/s11663-022-02606-2.

[69]   A. Gittins, (D) Effect of oxygen on hot workability of steel, International Metals Reviews. 22 (1977) 213–221. https://doi.org/10.1179/imtr.1977.22.1.213.

[70]   J.H. Park, H. Todoroki, Control of MgO·Al$_2$O$_3$ Spinel Inclusions in Stainless Steels, ISIJ International. 50 (2010) 1333–1346. https://doi.org/10.2355/isijinternational.50.1333.

[71]   H. Cui, W. Chen, Effect of Boron on Morphology of Inclusions in Tire Cord Steel, J. Iron Steel Res. Int. 19 (2012) 22–27. https://doi.org/10.1016/S1006-706X(12)60082-X.

[72]   H. Iwai, B. Tsujino, S. Isa, T. Ao, On the behavior of the oxide inclusions of system MnO-SiO2-Al2O3 in steels during hot-rolling, and their influence on tensile strength of the steel, Tetsu-to-Haga. 55 (1969) 887–900. https://doi.org/10.2355/tetsutohagane1955.55.10_887.

[73]   H. Colpaert, Metallography of Steels: Interpretation of Structure and the Effects of Processing, ASM International, 2018.

[74]   J. Monnot, B. Heritier, J. Cogne, Relationship of Melting Practice, Inclusion Type, and Size with Fatigue Resistance of Bearing Steels, in: J. Hoo (Ed.), Effect of Steel Manufacturing Processes on the Quality of Bearing Steels, ASTM International, 100 Barr Harbor Drive, PO Box C700, West Conshohocken, PA 19428-2959, 1988: pp. 149-149–16. https://doi.org/10.1520/STP26232S.

[75]   T.I. Johansson, T. Lund, P. Olund, A Review of Swedish Bearing Steel Manufacturing and Quality Assurance of Steel Products, Bearing Steel Technology-Advances and State of the Art in Bearing Steel Quality Assurance. 7th (2007) 3–15.

[76]   J. Cheng, R. Eriksson, P. Jönsson, Determination of macroinclusions during clean steel production, Ironmaking & Steelmaking. 30 (2003) 66–72. https://doi.org/10.1179/03019230325009470.

[77]   B.G. Bartosiaki, J.A.M. Pereira, W.V. Bielefeldt, A.C.F. Vilela, Assessment of inclusion analysis via manual and automated SEM and total oxygen content of steel, Journal of Materials Research and Technology. 4 (2015) 235–240. https://doi.org/10.1016/j.jmrt.2015.01.008.

[78]   Y. Murakami, Effects of nonmetallic inclusions on fatigue strength, in: Metal Fatigue: Effect of Small Defects and Nonmetallic Inclusions, 2nd ed., Academic Press, 2019.

[79]   S.X. Li, Effects of inclusions on very high cycle fatigue properties of high strength steels, International Materials Reviews. 57 (2012) 92–114. https://doi.org/10.1179/1743280411Y.0000000008.

[80]   A. Pineau, S. Forest, Effects of inclusions on the very high cycle fatigue behaviour of steels, Fatigue Fract Engng Mater Struct. 40 (2017) 1694–1707. https://doi.org/10.1111/ffe.12649.

[81]   Y. Unigame, K. Hiraoka, I. Takasu, Y. Kato, Evaluation Procedures of Nonmetallic Inclusions in Steel for Highly Reliable Bearings, Journal of ASTM International. 3 (2006) 1–8. https://doi.org/10.1520/JAI14030.

[82]   D. Brooksbank, K.W. Andrews, Stress fields around inclusions and their relation to mechanical properties, Journal of the Iron and Steel Institute. (1972) 246.

[83]   J. Lankford, Effect of oxide inclusions on fatigue failure, International Metals Reviews. 22 (1977) 221–228.

[84]   R. Kiessling, N. Lange, Non-metallic inclusions in steel, Second edition, The Metals Society, London, 1978.

[85]   N.M.A. Eid, P.F. Thomason, The nucleation of fatigue cracks in a low-alloy steel under high-cycle fatigue conditions and uniaxial loading, Acta Metallurgica. 27 (1979) 1239–1249. https://doi.org/10.1016/0001-6160(79)90140-8.

[86]   M.F. Garwood, H.H. Zurburg, M.A. Frickson, Correlation of Laboratory Tests and Service Performance, Interpretation of Tests and Correlation with Service, ASM. (1951).

[87]   D. Brooksbank, K. Andrews, Thermal Expansion of Some Inclusions Found in Steels and Relation to Tessellated Stresses, Journal of the Iron and Steel Institute. 206 (1968) 595-+.

[88]   D. Brooksbank, K. Andrews, Tessellated Stresses Associated with Some Inclusions in Steel, Journal of the Iron and Steel Institute. 207 (1969) 474-+.

[89]   K. Hashimoto, T. Fujimatsu, N. Tsunekage, K. Hiraoka, K. Kida, E.C. Santos, Study of rolling contact fatigue of bearing steels in relation to various oxide inclusions, Materials & Design. 32 (2011) 1605–1611. https://doi.org/10.1016/j.matdes.2010.08.052.

[90]   ISO, ISO 4967:2013 Steel - Determination of content of nonmetallic inclusions - Micrographic method using standard diagrams, n.d. https://www.iso.org/fr/standard/63156.html (accessed December 9, 2022).

[91]   G. Bernard, P.V. Riboud, G. Urbain, Étude de la plasticité d'inclusions d'oxydes, Rev. Met. Paris. 78 (1981) 421–434. https://doi.org/10.1051/metal/198178050421.

[92]   S. Ashok, Behaviour of inclusions during processing and its effect on directionality, Scripta Metallurgica. 14 (1980) 31–34. https://doi.org/10.1016/0036-9748(80)90119-2.

[93]   T.J. Baker, K.B. Gave, J.A. Charles, Inclusion deformation and toughness anisotropy in hot-rolled steels, Metals Technology. 3 (1976) 183–193. https://doi.org/10.1179/030716976803391656.

[94]   R. Kiessling, Non-metallic inclusions in steel, Part V, Book Number 411, The Institute of Materials, London, UK, 1989.

[95]   P. Lamagnere, D. Girodin, P. Meynaud, F. Vergne, A. Vincent, Study of elasto-plastic properties of microheterogeneities by means of nano-indentation measurements: Application to bearing steels, Materials Science and Engineering: A. 215 (1996) 134–142. https://doi.org/10.1016/0921-5093(96)10268-9.

[96]   C.F. Kusche, J.S.K.-L. Gibson, M.A. Wollenweber, S. Korte-Kerzel, On the mechanical properties and deformation mechanisms of manganese sulphide inclusions, Materials & Design. 193 (2020) 108801. https://doi.org/10.1016/j.matdes.2020.108801.

[97]   Y.-N. Wang, J. Yang, Y.-P. Bao, Effects of Non-metallic Inclusions on Machinability of Free-Cutting Steels Investigated by Nano-Indentation Measurements, Metall and Mat Trans A. 46 (2015) 281–292. https://doi.org/10.1007/s11661-014-2596-3.

[98]   R. Wagner, R. Lehnert, E. Storti, L. Ditscherlein, C. Schröder, S. Dudczig, U.A. Peuker, O. Volkova, C.G. Aneziris, H. Biermann, A. Weidner, Nanoindentation of alumina and multiphase inclusions in 42CrMo4 steel, Materials Characterization. 193 (2022) 112257. https://doi.org/10.1016/j.matchar.2022.112257.

[99]   S. Bruns, L. Petho, C. Minnert, J. Michler, K. Durst, Fracture toughness determination of fused silica by cube corner indentation cracking and pillar splitting, Materials & Design. 186 (2020) 108311. https://doi.org/10.1016/j.matdes.2019.108311.

[100]   C.R. Kurkjian, M. John Matthewson, Mechanical Strength and Reliability of Glass Fibers, in: Specialty Optical Fibers Handbook, Elsevier, 2007: pp. 735–781. https://doi.org/10.1016/B978-012369406-5/50026-6.

[101]   Narottam P. Bansal, R. Doremus, Handbook of glass properties, Academic Press, Orlando San Diego, 1986.

[102]   A. Stiénon, A. Fazekas, J.-Y. Buffière, A. Vincent, P. Daguier, F. Merchi, A new methodology based on X-ray micro-tomography to estimate stress concentrations around inclusions in high strength steels, Materials Science and Engineering: A. 513–514 (2009) 376–383. https://doi.org/10.1016/j.msea.2009.02.008.

[103]   Ashizuka M., Aimoto Y., Okuno T., Mechanical Properties of Sintered Silicate Crystals (Part 1), J. Ceram. Soc. Japan. 97 (1989) 544–548. https://doi.org/10.2109/jcersj.97.544.

[104]   A. Pönitzsch, M. Nofz, L. Wondraczek, J. Deubener, Bulk elastic properties, hardness and fatigue of calcium aluminosilicate glasses in the intermediate-silica range, Journal of Non-Crystalline Solids. 434 (2016) 1–12. https://doi.org/10.1016/j.jnoncrysol.2015.12.002.

[105]   A. Melander, How particles control ductile fracture during testing and metal working operations, in: Swedish Symposium on Non-Metallic Inclusions in Steel, Hans Nordberg and Rolf Sandström Eds., Uddeholms AB, Hagfors, Sweden1981, 1981: pp. 353–394.

[106]   J.B. Kosco, D.A. Koss, Ductile fracture of mechanically alloyed iron-yttria alloys, Metall Mater Trans A. 24 (1993) 681–687. https://doi.org/10.1007/BF02656636.

[107]   H. Qiu, H. Mori, M. Enoki, T. Kishi, Evaluation of Ductile Fracture of Structural Steels by Microvoid Model., ISIJ International. 39 (1999) 358–364. https://doi.org/10.2355/isijinternational.39.358.

[108]   G. Le Roy, J.D. Embury, G. Edwards, M.F. Ashby, A model of ductile fracture based on the nucleation and growth of voids, Acta Metallurgica. 29 (1981) 1509–1522. https://doi.org/10.1016/0001-6160(81)90185-1.

96

[109] D. Kwon, Interfacial decohesion around spheroidal carbide particles, Scripta Metallurgica. 22 (1988) 1161–1164. https://doi.org/10.1016/S0036-9748(88)80123-6.

[110] L. Babout, Y. Brechet, E. Maire, R. Fougères, On the competition between particle fracture and particle decohesion in metal matrix composites, Acta Materialia. 52 (2004) 4517–4525. https://doi.org/10.1016/j.actamat.2004.06.009.

[111] R.D. Thomson, J.W. Hancock, Ductile failure by void nucleation, growth and coalescence, Int J Fract. 26 (1984) 99–112. https://doi.org/10.1007/BF01157547.

[112] A. Das, Stress/Strain Induced Void?, Arch Computat Methods Eng. 28 (2021) 1795–1852. https://doi.org/10.1007/s11831-020-09444-y.

[113] C. Luo, Evolution of voids close to an inclusion in hot deformation of metals, Computational Materials Science. 21 (2001) 360–374. https://doi.org/10.1016/S0927-0256(01)00149-5.

[114] J.A. Connally, S.B. Brown, Micromechanical fatigue testing, Experimental Mechanics. 33 (1993) 81–90.

[115] T.E. Buchheit, S.J. Glass, J.R. Sullivan, S.S. Mani, D.A. Lavan, T.A. Friedmann, R. Janek, Micromechanical testing of MEMS materials, Journal of Materials Science. 38 (2003) 4081–4086. https://doi.org/10.1023/A:1026365219307.

[116] J.-Å. Schweitz, Mechanical Characterization of Thin Films by Micromechanical Techniques, MRS Bulletin. 17 (1992) 34–45. https://doi.org/10.1557/S0883769400041646.

[117] G. Dehm, B.N. Jaya, R. Raghavan, C. Kirchlechner, Overview on micro- and nanomechanical testing: New insights in interface plasticity and fracture at small length scales, Acta Materialia. 142 (2018) 248–282. https://doi.org/10.1016/j.actamat.2017.06.019.

[118] M.D. Uchic, P.A. Shade, D.M. Dimiduk, Plasticity of Micrometer-Scale Single Crystals in Compression, Annu. Rev. Mater. Res. 39 (2009) 361–386. https://doi.org/10.1146/annurev-matsci-082908-145422.

[119] F. Östlund, K. Rzepiejewska-Malyska, K. Leifer, L.M. Hale, Y. Tang, R. Ballarini, W.W. Gerberich, J. Michler, Brittle-to-Ductile Transition in Uniaxial Compression of Silicon Pillars at Room Temperature, Advanced Functional Materials. 19 (2009) 2439–2444. https://doi.org/10.1002/adfm.200900418.

[120] R. Lacroix, V. Chomienne, G. Kermouche, J. Teisseire, E. Barthel, S. Queste, Micropillar Testing of Amorphous Silica, Int J Appl Glass Sci. 3 (2012) 36–43. https://doi.org/10.1111/j.2041-1294.2011.00075.x.

[121] G. Kermouche, E. Barthel, D. Vandembroucq, Ph. Dubujet, Mechanical modelling of indentation-induced densification in amorphous silica, Acta Materialia. 56 (2008) 3222–3228. https://doi.org/10.1016/j.actamat.2008.03.010.

[122] S. Korte, W.J. Clegg, Discussion of the dependence of the effect of size on the yield stress in hard materials studied by microcompression of MgO, Philosophical Magazine. 91 (2011) 1150–1162. https://doi.org/10.1080/14786435.2010.505179.

[123] P.J. Imrich, C. Kirchlechner, G. Dehm, Influence of inclined twin boundaries on the deformation behavior of Cu micropillars, Materials Science and Engineering: A. 642 (2015) 65–70. https://doi.org/10.1016/j.msea.2015.06.064.

[124] C. Gunderson, N. Rohbeck, M. Tranchant, J. Michler, L. Philippe, Nanoscale 3D Electroforming by Template Pyrolysis, Advanced Engineering Materials. 23 (2021) 2001293. https://doi.org/10.1002/adem.202001293.

[125] D.S. Gianola, C. Eberl, Micro- and nanoscale tensile testing of materials, JOM. 61 (2009) 24–35. https://doi.org/10.1007/s11837-009-0037-3.

[126] M.A. Haque, M.T.A. Saif, In-situ tensile testing of nano-scale specimens in SEM and TEM, Experimental Mechanics. 42 (2002) 123–128.

[127] D.T. Read, J.W. Dally, A new method for measuring the strength and ductility of thin films, Journal of Materials Research. 8 (1993) 1542–1549. https://doi.org/10.1557/JMR.1993.1542.

[128] J.-K. Heyer, S. Brinckmann, J. Pfetzing-Micklich, G. Eggeler, Microshear deformation of gold single crystals, Acta Materialia. 62 (2014) 225–238. https://doi.org/10.1016/j.actamat.2013.10.002.

[129] M.-Y. Seok, H. Gopalan, S. Nandy, S. Zaefferer, D. Raabe, C. Kirchlechner, G. Dehm, Microscale plastic anisotropy of basal and pyramidal I slip in pure magnesium tested in shear, Materialia. 14 (2020) 100932. https://doi.org/10.1016/j.mtla.2020.100932.

[130] G. Guillonneau, S. Sao Joao, B. Adogou, S. Breumier, G. Kermouche, Plastic Flow Under Shear-Compression at the Micron Scale-Application on Amorphous Silica at High Strain Rate, JOM. 74 (2022) 2231–2237. https://doi.org/10.1007/s11837-021-05142-7.

[131] C. Herring, J.K. Galt, Elastic and Plastic Properties of Very Small Metal Specimens, Phys. Rev. 85 (1952) 1060–1061. https://doi.org/10.1103/PhysRev.85.1060.2.

[132] G.L. Pearson, W.T. Read, W.L. Feldmann, Deformation and fracture of small silicon crystals, Acta Metallurgica. 5 (1957) 181–191. https://doi.org/10.1016/0001-6160(57)90164-5.

[133] M.J. Matthewson, C.R. Kurkjian, S.T. Gulati, Strength Measurement of Optical Fibers by Bending, Journal of the American Ceramic Society. 69 (1986) 815–821. https://doi.org/10.1111/j.1151-2916.1986.tb07366.x.

[134] G. Stan, S. Krylyuk, A.V. Davydov, I. Levin, R.F. Cook, Ultimate Bending Strength of Si Nanowires, Nano Lett. 12 (2012) 2599–2604. https://doi.org/10.1021/nl300957a.

[135] Y. Bellouard, On the bending strength of fused silica flexures fabricated by ultrafast lasers [Invited], Opt. Mater. Express. 1 (2011) 816. https://doi.org/10.1364/OME.1.000816.

[136] M.G. Mueller, M. Fornabaio, G. Žagar, A. Mortensen, Microscopic strength of silicon particles in an aluminium–silicon alloy, Acta Materialia. 105 (2016) 165–175. https://doi.org/10.1016/j.actamat.2015.12.006.

[137] T.P. Weihs, S. Hong, J.C. Bravman, W.D. Nix, Mechanical deflection of cantilever microbeams: A new technique for testing the mechanical properties of thin films, Journal of Materials Research. 3 (1988) 931–942. https://doi.org/10.1557/JMR.1988.0931.

[138] O. Kraft, R. Schwaiger, W.D. Nix, Measurement of Mechanical Properties in Small Dimensions by Microbeam Deflection, MRS Online Proceedings Library. 518 (1998) 39–44. https://doi.org/10.1557/PROC-518-39.

[139] T. Namazu, Y. Isono, T. Tanaka, Evaluation of size effect on mechanical properties of single crystal silicon by nanoscale bending test using AFM, Journal of Microelectromechanical Systems. 9 (2000) 450–459. https://doi.org/10.1109/84.896765.

[140] V. Schnabel, B.N. Jaya, M. Köhler, D. Music, C. Kirchlechner, G. Dehm, D. Raabe, J.M. Schneider, Electronic hybridisation implications for the damage-tolerance of thin film metallic glasses, Sci Rep. 6 (2016) 36556. https://doi.org/10.1038/srep36556.

[141] M.G. Mueller, V. Pejchal, G. Žagar, A. Singh, M. Cantoni, A. Mortensen, Fracture toughness testing of nanocrystalline alumina and fused quartz using chevron-notched microbeams, Acta Materialia. 86 (2015) 385–395. https://doi.org/10.1016/j.actamat.2014.12.016.

[142] G. Žagar, V. Pejchal, M.G. Mueller, L. Michelet, A. Mortensen, Fracture toughness measurement in fused quartz using triangular chevron-notched micro-cantilevers, Scripta Materialia. 112 (2016) 132–135. https://doi.org/10.1016/j.scriptamat.2015.09.032.

[143] A.K. Saxena, S. Brinckmann, B. Völker, G. Dehm, C. Kirchlechner, Experimental conditions affecting the measured fracture toughness at the microscale: Notch geometry

and crack extension measurement, Materials & Design. 191 (2020) 108582. https://doi.org/10.1016/j.matdes.2020.108582.

[144] C. Tian, C. Kirchlechner, The fracture toughness of martensite islands in dual-phase DP800 steel, Journal of Materials Research. 36 (2021) 2495–2504. https://doi.org/10.1557/s43578-021-00150-4.

[145] A.D. Norton, S. Falco, N. Young, J. Severs, R.I. Todd, Microcantilever investigation of fracture toughness and subcritical crack growth on the scale of the microstructure in Al2O3, J. Eur. Ceram. Soc. 35 (2015) 4521–4533. https://doi.org/10.1016/j.jeurceramsoc.2015.08.023.

[146] A.K. Mishra, H. Gopalan, M. Hans, C. Kirchlechner, J.M. Schneider, G. Dehm, B.N. Jaya, Strategies for damage tolerance enhancement in metal/ceramic thin films: Lessons learned from Ti/TiN, Acta Materialia. 228 (2022) 117777. https://doi.org/10.1016/j.actamat.2022.117777.

[147] B.N. Jaya, C. Kirchlechner, G. Dehm, Can microscale fracture tests provide reliable fracture toughness values? A case study in silicon, J. Mater. Res. 30 (2015) 686–698. https://doi.org/10.1557/jmr.2015.2.

[148] D. Kiener, C. Motz, M. Rester, M. Jenko, G. Dehm, FIB damage of Cu and possible consequences for miniaturized mechanical tests, Materials Science and Engineering: A. 459 (2007) 262–272. https://doi.org/10.1016/j.msea.2007.01.046.

[149] Y. Xiao, J. Wehrs, H. Ma, T. Al-Samman, S. Korte-Kerzel, M. Göken, J. Michler, R. Spolenak, J.M. Wheeler, Investigation of the deformation behavior of aluminum micropillars produced by focused ion beam machining using Ga and Xe ions, Scripta Materialia. 127 (2017) 191–194. https://doi.org/10.1016/j.scriptamat.2016.08.028.

[150] E. Preiss, B. Merle, Y. Xiao, F. Gannott, J.P. Liebig, J.M. Wheeler, M. Goeken, Applicability of focused Ion beam (FIB) milling with gallium, neon, and xenon to the fracture toughness characterization of gold thin films, J. Mater. Res. 36 (2021) 2505–2514. https://doi.org/10.1557/s43578-020-00045-w.

[151] G. Žagar, V. Pejchal, M.G. Mueller, A. Rossoll, M. Cantoni, A. Mortensen, The local strength of microscopic alumina reinforcements, Acta Materialia. 100 (2015) 215–223. https://doi.org/10.1016/j.actamat.2015.08.026.

[152] V. Pejchal, M. Fornabaio, G. Žagar, A. Mortensen, The local strength of individual alumina particles, Journal of the Mechanics and Physics of Solids. 109 (2017) 34–49. https://doi.org/10.1016/j.jmps.2017.08.005.

[153] M.G. Mueller, G. Žagar, A. Mortensen, In-situ strength of individual silicon particles within an aluminium casting alloy, Acta Materialia. 143 (2018) 67–76. https://doi.org/10.1016/j.actamat.2017.09.058.

[154] R.N. Widmer, D. Bischof, J. Jurczyk, M. Michler, J. Schwiedrzik, J. Michler, Smooth or not: Robust fused silica micro-components by femtosecond-laser-assisted etching, Materials & Design. 204 (2021) 109670. https://doi.org/10.1016/j.matdes.2021.109670.

[155] R. Lacroix, G. Kermouche, J. Teisseire, E. Barthel, Plastic deformation and residual stresses in amorphous silica pillars under uniaxial loading, Acta Materialia. 60 (2012) 5555–5566. https://doi.org/10.1016/j.actamat.2012.07.016.

[156] G. Kermouche, G. Guillonneau, J. Michler, J. Teisseire, E. Barthel, Perfectly plastic flow in silica glass, Acta Materialia. 114 (2016) 146–153. https://doi.org/10.1016/j.actamat.2016.05.027.

[157] L. Borasi, E. Casamenti, R. Charvet, C. Dénéréaz, S. Pollonghini, L. Deillon, T. Yang, F. Ebrahim, A. Mortensen, Y. Bellouard, 3D metal freeform micromanufacturing, Journal of Manufacturing Processes. 68 (2021) 867–876. https://doi.org/10.1016/j.jmapro.2021.06.002.

[158] L. Borasi, S. Frasca, K. Nicolet-Dit-Felix, E. Charbon, A. Mortensen, Coupling silicon lithography with metal casting, Applied Materials Today. 29 (2022) 101647. https://doi.org/10.1016/j.apmt.2022.101647.

[159] V. Pejchal, M. Fornabaio, G. Žagar, G. Riesen, R.G. Martin, J. Medřický, T. Chráska, A. Mortensen, Meridian crack test strength of plasma-sprayed amorphous and nanocrystalline ceramic microparticles, Acta Materialia. 145 (2018) 278–289. https://doi.org/10.1016/j.actamat.2017.12.031.

[160] G. Žagar, V. Pejchal, M. Kissling, A. Mortensen, On the diametric compression strength test of brittle spherical particles, European Journal of Mechanics - A/Solids. 72 (2018) 148–154. https://doi.org/10.1016/j.euromechsol.2018.04.016.

[161] W.C. Oliver, G.M. Pharr, An improved technique for determining hardness and elastic modulus using load and displacement sensing indentation experiments, Journal of Materials Research. 7 (1992) 1564–1583. https://doi.org/10.1557/JMR.1992.1564.

[162] W.C. Oliver, G.M. Pharr, Measurement of hardness and elastic modulus by instrumented indentation: Advances in understanding and refinements to methodology, J. Mater. Res. 19 (2004) 18.

[163] R. Saha, W.D. Nix, Soft films on hard substrates — nanoindentation of tungsten films on sapphire substrates, Materials Science and Engineering: A. 319–321 (2001) 898–901. https://doi.org/10.1016/S0921-5093(01)01076-0.

[164] R. Saha, W.D. Nix, Effects of the substrate on the determination of thin film mechanical properties by nanoindentation, Acta Materialia. 50 (2002) 23–38. https://doi.org/10.1016/S1359-6454(01)00328-7.

[165] J. Hay, B. Crawford, Measuring substrate-independent modulus of thin films, J. Mater. Res. 26 (2011) 727–738. https://doi.org/10.1557/jmr.2011.8.

[166] J.W. Leggoe, Determination of the elastic modulus of microscale ceramic particles via nanoindentation, J. Mater. Res. 19 (2004) 2437–2447. https://doi.org/10.1557/JMR.2004.0300.

[167] W. Yan, C.L. Pun, Z. Wu, G.P. Simon, Some issues on nanoindentation method to measure the elastic modulus of particles in composites, Composites Part B: Engineering. 42 (2011) 2093–2097. https://doi.org/10.1016/j.compositesb.2011.05.002.

[168] W. Yan, C.L. Pun, G.P. Simon, Conditions of applying Oliver–Pharr method to the nanoindentation of particles in composites, Composites Science and Technology. 72 (2012) 1147–1152. https://doi.org/10.1016/j.compscitech.2012.03.019.

[169] T.E. Buchheit, T.J. Vogler, Measurement of ceramic powders using instrumented indentation and correlation with their dynamic response, Mechanics of Materials. 42 (2010) 599–614. https://doi.org/10.1016/j.mechmat.2010.02.007.

[170] J.E. Jakes, C.R. Frihart, J.F. Beecher, R.J. Moon, D.S. Stone, Experimental method to account for structural compliance in nanoindentation measurements, J. Mater. Res. 23 (2008) 1113–1127. https://doi.org/10.1557/jmr.2008.0131.

[171] R.N. Widmer, A. Groetsch, G. Kermouche, A. Diaz, G. Pillonel, M. Jain, R. Ramachandramoorthy, L. Pethö, J. Schwiedrzik, J. Michler, Temperature–dependent dynamic plasticity of micro-scale fused silica, Materials & Design. 215 (2022) 110503. https://doi.org/10.1016/j.matdes.2022.110503.

[172] S. Korte, R.J. Stearn, J.M. Wheeler, W.J. Clegg, High temperature microcompression and nanoindentation in vacuum, Journal of Materials Research. 27 (2012) 167–176. https://doi.org/10.1557/jmr.2011.268.

[173] J.M. Wheeler, D.E.J. Armstrong, W. Heinz, R. Schwaiger, High temperature nanoindentation: The state of the art and future challenges, Current Opinion in Solid State and Materials Science. 19 (2015) 354–366. https://doi.org/10.1016/j.cossms.2015.02.002.

[174] G. Tiphéne, P. Baral, S. Comby-Dassonneville, G. Guillonneau, G. Kermouche, J.-M. Bergheau, W. Oliver, J.-L. Loubet, High-Temperature Scanning Indentation: A new method to investigate in situ metallurgical evolution along temperature ramps, Journal of Materials Research. 36 (2021) 2383–2396. https://doi.org/10.1557/s43578-021-00107-7.

[175] S. Bruns, T. Uesbeck, S. Fuhrmann, M. Tarragó Aymerich, L. Wondraczek, D. de Ligny, K. Durst, Indentation densification of fused silica assessed by raman spectroscopy and constitutive finite element analysis, Journal of the American Ceramic Society. 103 (2020) 3076–3088. https://doi.org/10.1111/jace.17024.

[176] M.F. Doerner, W.D. Nix, A method for interpreting the data from depth-sensing indentation instruments, J. Mater. Res. 1 (1986) 601–609. https://doi.org/10.1557/JMR.1986.0601.

[177] H. Gao, C.-H. Chiu, J. Lee, Elastic contact versus indentation modeling of multi-layered materials, International Journal of Solids and Structures. 29 (1992) 2471–2492. https://doi.org/10.1016/0020-7683(92)90004-D.

[178] R.B. King, Elastic analysis of some punch problems for a layered medium, International Journal of Solids and Structures. 23 (1987) 1657–1664. https://doi.org/10.1016/0020-7683(87)90116-8.

[179] J. Menčík, D. Munz, E. Quandt, E.R. Weppelmann, M.V. Swain, Determination of elastic modulus of thin layers using nanoindentation, J. Mater. Res. 12 (1997) 2475–2484. https://doi.org/10.1557/JMR.1997.0327.

[180] A.C. Fischer-Cripps, Nanoindentation of Thin Films and Small Volumes of Materials, in: A.C. Fischer-Cripps (Ed.), Nanoindentation, Springer, New York, NY, 2011: pp. 147–161. https://doi.org/10.1007/978-1-4419-9872-9_8.

[181] P. Sudharshan Phani, W.C. Oliver, A critical assessment of the effect of indentation spacing on the measurement of hardness and modulus using instrumented indentation testing, Materials & Design. 164 (2019) 107563. https://doi.org/10.1016/j.matdes.2018.107563.

[182] S.P. Timoshenko, J.N. Goodier, Theory of Elasticity, 2nd ed., McGraw-Hill Book Company, 1970.

[183] K.L. Johnson, Contact mechanics, Cambridge university press, 1987.

[184] C.A. Schneider, W.S. Rasband, K.W. Eliceiri, NIH Image to ImageJ: 25 years of image analysis, Nat Methods. 9 (2012) 671–675. https://doi.org/10.1038/nmeth.2089.

[185] R.J. Hand, D.R. Tadjiev, S.A. Hayes, Nano-indentation and surface hydration of silicate glasses, J. Ceram. Soc. Japan. 116 (2008) 846–850. https://doi.org/10.2109/jcersj2.116.846.

[186] D.R. Tadjiev, R.J. Hand, Surface hydration and nanoindentation of silicate glasses, Journal of Non-Crystalline Solids. 356 (2010) 102–108. https://doi.org/10.1016/j.jnoncrysol.2009.10.005.

[187] Forward, Gordon Edward, Nucleation of oxide inclusions during the solidification of iron, Massachusetts Institute of Technology MIT, 1966.

[188] D. Tuschel, Why are the Raman spectra of crystalline and amorphous solids different?, Spectroscopy (Santa Monica). 32 (2017) 26–33.

[189] L. Zhang, B.G. Thomas, State of the art in the control of inclusions during steel ingot casting, Metall and Materi Trans B. 37 (2006) 733–761. https://doi.org/10.1007/s11663-006-0057-0.

[190] J. Gleinig, A. Weidner, J. Fruhstorfer, C.G. Aneziris, O. Volkova, H. Biermann, Characterization of Nonmetallic Inclusions in 18CrNiMo7-6, Metall and Materi Trans B. 50 (2019) 337–356. https://doi.org/10.1007/s11663-018-1431-4.

[191] K. Wasai, K. Mukai, Mechanism of Formation of Amorphous Silica Inclusion in Silicon Deoxidized Copper, ISIJ International. 43 (2003) 606–611. https://doi.org/10.2355/isijinternational.43.606.

[192] J.E. Shelby, Formation and Properties of Calcium Aluminosilicate Glasses, Journal of the American Ceramic Society. 68 (1985) 155–158. https://doi.org/10.1111/j.1151-2916.1985.tb09656.x.

[193] D.R. Poirier, G.H. Geiger, Transport Phenomena in Materials Processing, The Minerals, Metals, and Materials Society, 1994.

[194] J. Everaerts, A. Slagter, A. Mortensen, A method for cleaning flat punch diamond microprobe tips, Micron. 155 (2022) 103217. https://doi.org/10.1016/j.micron.2022.103217.

[195] S. Bruns, K.E. Johanns, H.U.R. Rehman, G.M. Pharr, K. Durst, Constitutive modeling of indentation cracking in fused silica, J Am Ceram Soc. 100 (2017) 1928–1940. https://doi.org/10.1111/jace.14734.

[196] R. Ramachandramoorthy, J. Schwiedrzik, L. Petho, C. Guerra-Nuñez, D. Frey, J.-M. Breguet, J. Michler, Dynamic Plasticity and Failure of Microscale Glass: Rate-Dependent Ductile–Brittle–Ductile Transition, Nano Lett. 19 (2019) 2350–2359. https://doi.org/10.1021/acs.nanolett.8b05024.

[197] Z. Tang, N.P. Lower, P.K. Gupta, C.R. Kurkjian, R.K. Brow, Using the two-point bend technique to determine failure stress of pristine glass fibers, Journal of Non-Crystalline Solids. 428 (2015) 98–104. https://doi.org/10.1016/j.jnoncrysol.2015.08.005.

[198] Duncan, France, Craig, The effect of environment on the strength of optical fiber, in: Strength of Inorganic Glass, C.R. Kurkjian, Plenum Press, New York, 1985: pp. 309–328.

[199] C.R. Kurkjian, P.K. Gupta, R.K. Brow, The Strength of Silicate Glasses: What Do We Know, What Do We Need to Know?, International Journal of Applied Glass Science. 1 (2010) 27–37. https://doi.org/10.1111/j.2041-1294.2010.00005.x.

[200] C.R. Kurkjian, O.S. Gebizlioglu, I. Camlibel, Strength variations in silica fibers, in: M.J. Matthewson (Ed.), Boston, MA, 1999: pp. 77–86. https://doi.org/10.1117/12.372757.

[201] M. Guerette, C.R. Kurkjian, S. Semjonov, L. Huang, Nonlinear Elasticity of Silica Glass, J. Am. Ceram. Soc. 99 (2016) 841–848. https://doi.org/10.1111/jace.14043.

[202] P.K. Gupta, C.R. Kurkjian, Intrinsic failure and non-linear elastic behavior of glasses, Journal of Non-Crystalline Solids. 351 (2005) 2324–2328. https://doi.org/10.1016/j.jnoncrysol.2005.05.029.

[203] B.A. Proctor, I. Whitney, J.W. Johnson, The Strength of Fused Silica, Proceedings of the Royal Society of London. Series A, Mathematical and Physical Sciences. 297 (1967) 534–557.

[204] L.G. Baikova, T.I. Pesina, M.F. Kireenko, L.V. Tikhonova, C.R. Kurkjian, Strength of optical silica fibers measured in liquid nitrogen, Tech. Phys. 60 (2015) 869–872. https://doi.org/10.1134/S1063784215060031.

[205] C.R. Kurkjian, P.K. Gupta, R.K. Brow, N. Lower, The intrinsic strength and fatigue of oxide glasses, Journal of Non-Crystalline Solids. 316 (2003) 114–124. https://doi.org/10.1016/S0022-3093(02)01943-9.

[206] E. Suhir, Effect of the nonlinear stress-strain relationship on the maximum stress in silica fibers subjected to two-point bending, Appl. Opt. 32 (1993) 1567. https://doi.org/10.1364/AO.32.001567.

[207] E. Barthel, V. Keryvin, G. Rosales-Sosa, G. Kermouche, Indentation cracking in silicate glasses is directed by shear flow, not by densification, Acta Materialia. 194 (2020) 473–481. https://doi.org/10.1016/j.actamat.2020.05.011.

[208] Marsh, Plastic flow in glass, Proceedings of the Royal Society of London. Series A, Mathematical and Physical Sciences. 279 (1964) 19. https://doi.org/10.1098/rspa.1964.0114.

[209] D. Wakabayashi, N. Funamori, T. Sato, Enhanced plasticity of silica glass at high pressure, Phys. Rev. B. 91 (2015) 014106. https://doi.org/10.1103/PhysRevB.91.014106.

[210] G. Brambilla, D.N. Payne, The Ultimate Strength of Glass Silica Nanowires, Nano Lett. 9 (2009) 831–835. https://doi.org/10.1021/nl803581r.

[211] B.E. Ramachandran, B.C. Pai, N. Balasubramanian, Studies on the Acid Resistance of E Glass, Journal of the American Ceramic Society. 63 (1980) 1–3. https://doi.org/10.1111/j.1151-2916.1980.tb10634.x.

[212] M.J. Matthewson, C.R. Kurkjian, J.R. Hamblin, Acid stripping of fused silica optical fibers without strength degradation, Journal of Lightwave Technology. 15 (1997) 490–497. https://doi.org/10.1109/50.557565.

[213] H.D. Chandler, R.L. Jones, Strength loss in ″E″ glass fibres treated in strong solutions of mineral acids, J Mater Sci. 19 (1984) 3849–3854. https://doi.org/10.1007/BF00980747.

[214] T. Geisler, A. Janssen, D. Scheiter, T. Stephan, J. Berndt, A. Putnis, Aqueous corrosion of borosilicate glass under acidic conditions: A new corrosion mechanism, Journal of Non-Crystalline Solids. 356 (2010) 1458–1465. https://doi.org/10.1016/j.jnoncrysol.2010.04.033.

Curriculum Vitae

Alejandra Inés Slagter

25.10.1990

alejandra.slagter@epfl.ch

alejandraslagter@gmail.com

Education

Since Oct 2018	**PhD in Materials Science and Engineering** at École Polytechnique Fédéral de Lausanne (**EPFL**), Switzerland Laboratory of Mechanical Metallurgy
Sep 2016 – Aug 2018	**Double Master degree in Materials Science and Engineering** (AMASE master program) 2nd year - Luleå Tekniska Universitet (**LTU**), Sweden 1st year - Universitat Politecnica de Catalunya (**UPC**), Spain
Feb 2010 – Nov 2015	**Materials Engineering** at Universidad Nacional de La Plata (**UNLP**), Argentina

Publications

Slagter A., Everaerts J., Mortensen A., Nanoindentation of embedded particles, *Journal of Materials Research* (2023). https://doi.org/10.1557/s43578-023-00920-2

Slagter A., Everaerts J., Deillon L., Mortensen A., Strong silicon oxide inclusions in iron, *Acta Materialia*. 242 (2023) 10.1016/j.actamat.2022.118437

Everaerts J., Slagter A., Mortensen A., A method for cleaning flat punch diamond microprobe tips, *Micron*. 155, (2022) 10.1016/j.micron.2022.103217